Eddy diffusivities from a doubly-periodic quasi-geostrophic model of the Antarctic Circumpolar Current

Claire Murray

Master of Engineering

Department of Civil Engineering and Applied Mechanics

McGill University

Montreal,Quebec

2013

A thesis submitted to McGill University in partial fulfillment of the requirements for the degree of Master of Engineering

ABSTRACT

The Antarctic Circumpolar Current (ACC), long recognized for its importance in world ocean and climate dynamics, is close to purely zonal in many regions. This means the majority of meridional transport of heat or other scalars is largely achieved by transient mesoscale eddies. Many long-running climate models are still unable to resolve the mesoscale; their effects are parameterized, most commonly using the GM90 parameterization which relates mass transport to the slopes of isopycnal layers via an eddy diffusivity, κ.

In this project, the ACC was modelled using a two-layer quasi-geostrophic model with idealistic topography. A series of simulations were carried out at combination of topography heights and forcing strengths. Time-mean statistics were used to fit several forms of κ.

A paradox was found in κ_0, the cross-jet diffusivity. In a global sense, κ_0 increases as the strength of forcing and jet velocities increased, consistent with higher eddy kinetic energy. On the other hand, a local definition of κ_0 was found to be a local minimum in the jet core where the velocity peaked, consistent with research suggesting the ACC cores suppress mixing. In addition, a skew diffusivity, κ_{skew} was fitted and found to be globally non-zero for the higher topography, corresponding to a net eastwards flux.

For the ridge simulations, large-scale variation in κ_0 and κ_{skew} was noted and attributed to the effect of local bottom topography on baroclinic instability. This motivated a matrix definition of κ, which included the bottom topography gradient as an additional parameter to explain along and cross jet mass fluxes. In all forms the cross-jet diffusivity showed a large dependence on the density gradient.

RESUMÉ

Le rôle du Courant Circumpolaire Antarctique (CCA) dans la dynamique mondiale des océans est reconnu depuis longtemps. L'écoulement du CCA est presque de purement zonal dans de nombreuses régions, ce qui signifie que la majorité du transport traversant les jets est effectuée par les remous méso-échelles. La plupart des modèles climatiques de longue durée sont encore incapables de résoudre la méso-échelle et les effets de ces remous doivent être paramétrés. Actuellement, le modèle GM90, qui estime le transport de masse à partir des pistes isopycnales en utilisant une diffusivité turbulente, κ, est le plus fréquemment employé.

Dans ce projet, le CCA a été représenté par un modèle quasigéostrophique de deux couches avec de la topographie idéaliste. Une série de simulations a été réalisée en changeant la hauteur de la topographie et le niveau du forçage. Dans le but d'évaluer plusieurs formes de la diffusivité turbulente, une analyse des statistiques temporelles a été réalisée .

La diffusivité turbulente normale dans la direction méridienne, κ_0, a augmenté avec le gradient de densité. Une définition locale de κ_0, cependant, était un minimum dans le noyau de jet, en accord avec des recherches qui suggèrent la suppression du transport tranversant le CCA. Une diffusivité turbulente dans la direction du débit moyen, κ_{skew}, a été également estimée, montrant un flux net vers l'est pour les topographies et les forçages supérieurs.

Des répartitions spatiales ont été notées dans les κ_0 et κ_{skew}. Celles ont motivé une matrice de diffusion turbulente afin d'essayer de prendre en compte l'effet de la topographie sur les flux de masse. Cette forme a été appliquée globalement et localement, et a permis de réduire la variation spatiale de κ_0 et κ_{skew}.

ACKNOWLEDGEMENTS

Firstly I would like to express my sincerest gratitude to my supervisors, Prof. David Straub and Prof. Susan Gaskin, with whom it was a pleasure to work with over this project. The project would not have been possible without their encouragement and guidance. I will miss David's relaxed, yet extremely knowledgeable, style of guidance and Susan's big picture perspective and encouragement.

I wish to thank the other graduate students in my research group, who were always ready to provide a fresh eye on the project and problems.

Thank you to my family and friends in Montreal, who made the experience enjoyable and the long cold winters bearable. I felt very privileged to have such a fantastic support network in the city. On another note, I thank my parents, sister and friends at home for all their greatly-appreciated long-distance moral support.

In terms of support in another sense, this work would not have been possible without the financial support provided by NSERC grant, award number CGS-M 403869-11, and a GEC3 graduate student stipend.

TABLE OF CONTENTS

LIST OF TABLES

LIST OF FIGURES

LIST OF SYMBOLS

Scalar quantities (Roman symbols)

A_h	Biharmonic dissipation coefficient
dt	Timestep
dx, dy	Physical Resolution in x and y directions
D	Dissipation in model
f	Coriolis term, Planetary vorticity
f_0	Value of f in the centre of the domain
F	Forcing term in model
F_f	Forcing factor
g	Gravitational acceleration
g'	Reduced gravitational acceleration
h_0	Topography height
H	Mean layer thickness
J	Jacobian Operator
L_D	Rossby radius of deformation
L_{rhines}	Rhines scale
L_x	Zonal domain width
L_y	Meridional domain width
P	Pressure
q	Potential Vorticity
Q	Mean potential vorticity
r	Bottom friction (Rayleigh) coefficient
R	Radius of the Earth
t	Time

U_1	Imposed shear velocity in the upper layer
U_2	Imposed shear velocity in the lower layer
U_{crit}	Critical shear velocity
U_{onset}	Shear velocity at which the onset of baroclinic instability is observed
U_{shear}	Imposed shear velocity
w	Vertical Velocity

Scalar Quantities (Greek symbols)

α_i	Coefficients of an Eddy Diffusivity Matrix where i=1,2,3,4
β	Meridional derivative of f
β_{eff}	Effective β term
$\delta_{i,j}$	Direc delta function, 1 when $i = j$, zero otherwise
ζ	Relative Vorticity
η	Elevation of fluid interface
η_b	Elevation of bottom topography
η_y^{crit}	Critical interface gradient
κ	Eddy Diffusivity
κ_0	Normal cross-front eddy diffusivity
κ_{skew}	Skew, along-stream eddy diffusivity
λ	Wavelength
μ	Along-stream velocity
ν	Cross-stream velocity
ρ	Fluid density
ψ	Stream function
Ω	Angular velocity of the Earths rotation
θ	Latitude

Vector and Tensor Quantities

$\mathbf{u}$	Instantaneous horizontal velocity vector $(u, v)^T$
$\mathbf{u^b}$	Bolus velocity vector $(u^b, v^b)^T$

Subscripts

1	Upper Layer
2	Lower Layer
n	Parital derivative in cross-stream direction
l	Partial derivative in along stream direction
t	Partial derivative in time
x	Partial derivative in x-direction (zonal)
y	Partial derivative in y-direction (meridional)

Superscripts

$*$	Used to denote the Bolus flux velocity
'	Fluctuating quantity with zero mean
0	0-order, non-divergent
1	1-order, divergent
BC	Baroclinic
BT	Barotropic
f	Flat-bottom topography
g	Global
I	Interface between two fluid layers
jc	Jet core
S	Free surface
tot	Total

Averaging Operators

$\overline{a}$	Time-average of variable a
$\langle a \rangle$	Spatial average of a over the domain
$\langle a \rangle^x$	Zonal average of a
$\|a\|$	Absolute value of a

Notes

- The symbols most frequently used in this thesis are listed here
- Other notation introduced is defined at the first instance it appears in the text
- Vectors and tensors are written in bold

Chapter 1
Introduction

1.1 Motivation

Ocean transport of scalars, such as heat, fresh water, nutrients and CO_2, is of interest not only for ocean circulation, chemistry and biology, but also for the larger climate system. Modelling this transport is difficult due to the large range of length-scales that need to be resolved or parameterized (Washington and Parkinson, 2005). For example, ocean basins span thousands of kilometres, but ocean currents are typically 100 km or so wide. Moreover, these currents are unstable; consequently, the currents are associated with meandering pathways and with a rich field of eddies superimposed on the mean flow. The most energetic scale of these eddies is the mesoscale, which scales on the order of 100 km (Vallis, 2006). A further complication is that the length and time scales of both the currents and the mesoscale eddy field is such that the Coriolis acceleration (or force) is typically large compared to the advection of momentum. This gives rise to a dynamical balance called geostrophy, in which the horizontal density gradient force and Coriolis force balance. To leading order, one thinks of the horizontal ocean flow as the superposition of geostrophic currents and eddies.

Ideally, models of ocean transport of various chemical and dynamical scalars would explicitly account for advection by both the mean flow and the eddy field. In practise, however, eddy transport is often parameterized. This is especially true in climate applications, where the ocean represents only one component of the total system and where long time integrations are often needed. In other words, climate models include modules describing the ocean, atmosphere, and cryrosphere, as well as land surface characteristics, biology, and inherently sub-grid processes such as radiation and clouds. The biggest challenge in the coupling of the atmosphere with the ocean lies in the large difference between their time and spatial scales (Washington and Parkinson, 2005). Ocean dynamics typically occur at much smaller spatial scales, which would demand a much finer grid size to explicitly resolve. Such complexity comes at a cost, and it is almost universal in climate modelling that the ocean eddy field is parameterized rather than resolved explicitly (Garrison, 2004). Typically, the eddy transport is assumed to be down the mean gradient, and much attention is given to describing the assumed proportionality constant, or eddy diffusivity (κ).

A region of particular interest to climate scientists is the Southern Ocean, in which is located the oceans' strongest current, the Antarctic Circumpolar Current, or ACC. The ACC can be thought of as linking together the Atlantic, Pacific and Indian Oceans. It is dynamically distinct from the other major ocean currents in that it circumnavigates the globe, stretching 24 000 km (Wolff et al., 1991). The current is composed of several narrow meandering jets. The regions of strong eastwards flow in the jet cores, reaching surface velocity magnitudes of up to 33 cm/s (Phillips and Rintoul, 2000), are separated by weaker return flows to the west. These velocities peak at the surface in the jet cores and decay rapidly through the upper kilometer (Ferrari and Nikurashin, 2010). The ACC is driven by a combination of strong westerly winds (Garrison, 2004) and the meridional (north-south) density gradient in the Southern Ocean (Vallis, 2006; Gille, 2002), which is reinforced by thermohalocirculation. While the winds are a momentum source, the density structure supplies potential energy to the flow.

Tracer and heat transport across the ACC is of particular importance to climate dynamics in that the oceans global overturning cell (in which water sinks mainly in the North Atlantic and upwelling mainly in the Southern Ocean) must cross the ACC. For this reason, heat transport in the Southern Ocean is of first order importance in global heat budgets (Nowlin Jr and Klinck, 1986). However, since the ACC is close to zonal in many regions, the meridional transport of, say, CO_2 or nutrients, is accomplished by the eddy field. Moreover, ACC jet cores are believed to be inhibitors to meridional transport (Ferrari and Nikurashin, 2010; Marshall et al., 2006). Often this is believed to be due to the conservation of a quantity called potential vorticity, which we will explain in Section 2.1.

As in the entire ocean, transport across the ACC is necessarily parameterized in climate models. The most common form is that originally proposed by Gent and Mcwilliams (1990) and, commonly referred to as the GM90 parameterization. Formally it predicts mass transport between isopycnal surfaces to be proportional to the slope of the layer thickness (distance between isopycnals separated by a constant density difference, $\Delta\rho$). The constant of relation is the eddy diffusivity. Often a constant value for κ is used (Eden, 2006), although the various means of estimating κ produce a large range of estimates and spatial variation in the literature (e.g. Naveira Garabato et al. 2011; Marshall et al. 2006). Furthermore, in practice κ may often be derived from the resolved large-scale density structure (Nakamura and Chao, 2000). Given that mass transport across the ACC is achieved almost entirely by mesoscale eddies, the specification of κ in non-eddy resolving models dictates cross-jet transport predictions (Farneti et al., 2010; Treguier et al., 1997). This was evident in the most recent Intergovernmental Panel on Climate Change (IPCC) assessment in 2007, which published results with ACC transport varying over a factor of close to ten (Kuhlbrodt et al., 2012).

Evidence suggests that the Southern Ocean has already experienced some warming in the wake of climate change (Gille, 2002). Furthermore, the IPCC Fourth Assessment Report predicts a poleward shift and intensification of westerly winds in the Southern Ocean over the twenty-first century. These new wind patterns are thought to have an influence over the density structure in the Southern Ocean through changes to Ekman pumping (downwelling) in the mid-latitudes and upwelling of deep waters in the poles, and potentially steepening isopycnals (Wang et al., 2011). Several authors have published work predicting the ACC response to recent and forecast environmental changes (e.g. Hogg et al. 2008; Sen Gupta et al. 2009; Wang et al. 2011), however predictions are heavily reliant on the choice of sub-grid eddy parameterization (Kuhlbrodt et al., 2012). The interaction with bottom bathymetry is also still unclear and could play an important role in the ACC response (Wang et al., 2011).

In a recent paper, Thompson and Sallée (2012) study cross-jet transport using a two-layer quasi-geostrophic (QG) model (we will explain QG theory shortly in Section 2.1) of the ACC and an idealistic 3D ridge topography. The model forcing mirrors the classic Phillips problem for two-layer baroclinic instability (see Section 2.2) by imposing an inclination on the interface between the two fluids. They vary the zonal (west-east) extent of the ridge to explore both the localization of cross-jet transport in the domain and effect on net cross-jet transport in the domain.

1.2 Project Objectives

Here we will also study the ACC using a two-layer QG model with an idealistic ridge topography. Although a two-layer approximation is crude, it is commonly used in the ocean and qualitatively gives good results (Salmon, 1998). We are interested in the effect of both bottom topography and the strength of the meridional density gradient on eddy diffusivities in the ACC. To this end, we will vary both the height of our topography and the strength of the forcing in our model. We will investigate the relationship between coarse grained fields and eddy transport with the aim to assess the usefulness of eddy-diffusivity parameterizations. In particular, we hope to develop an understanding of how these parameterizations are affected by bathymetry and the strength of the imposed forcing. We will consider several parameterization of increasing complexity. In particular we are interested in whether the employment of more complex parameterizations adds more value and is worthwhile.

1.3 Synopsis of the thesis

In Chapter 2 we introduce the background theory of quasigeostrophy (QG) and instabilities in QG flow. In Chapter 3 we review literature pertaining to eddy mass flux parameterization and then orient the discussion more specifically to parameterization in the ACC and the effects of topography. Chapter 4 explains the numerical framework we use to analyze the problem. Results are presented in Chapter 5 and followed by a summary of the work in Chapter 6.

Chapter 2
Theoretical Background

Our model of the ACC is based on a two-layer quasigeostrophic (QG) model. In the first part of this chapter we derive the governing QG equations. We will first show the derivation for a simple one-layer case, then in the following extend to a two-layer case. A more rigorous treatment and explanation of the derivations can be found in several textbooks (e.g. Cushman-Roisin 1994; Salmon 1998). In Section 2.2 we will present types of instabilities relevant to the problem.

2.1 Quasigeostrophy

2.1.1 Derivations of the QG equations in a one-layer system

For the one-layer case, we consider the system in Figure 2–1 with a constant density of ρ_0 and an average depth H. Variation of the free surface from the average value is represented by η, measured as positive above the free surface. We define x to be in the zonal (west-east) direction and positive to the east, y to be in the meridional (north-south) direction and positive to the north, and z is the vertical coordinate.

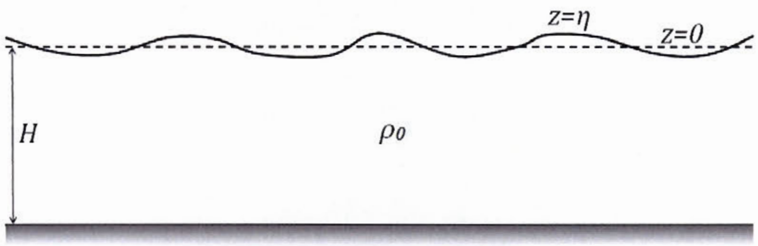

Figure 2–1: Representation and notation for one-layer quasi-geostrophic equations

We start with the shallow water Navier-Stokes equations in a rotating reference frame. Equation 2.1 and 2.2 are the momentum equations in the zonal and meridional directions respectively and Equation 2.3 is a non-divergence of the velocity field from the continuity equation by assuming incompressibility.

$$\frac{\partial u}{\partial t} + u(\nabla \cdot \mathbf{u}) - fv = -\frac{1}{\rho}\frac{\partial P}{\partial x} \tag{2.1}$$

$$\frac{\partial v}{\partial t} + v(\nabla \cdot \mathbf{u}) + fu = -\frac{1}{\rho}\frac{\partial P}{\partial y} \tag{2.2}$$

$$\frac{\partial u}{\partial x} + \frac{\partial v}{\partial y} + \frac{\partial w}{\partial z} = 0 \tag{2.3}$$

The last term on the left-hand sides of equations Equations 2.1 and 2.2 is the Coriolis force and f is the Coriolis term which is a sinusoidal function of latitude. The typical time and length scales of ocean circulation mean not only that the Coriolis force is a dominant term but its variation with latitude is also important. In a Cartesian coordinate system, the β-plane assumption is commonly used to account for this variation with latitude. It can be found by taking a Taylor series expansion about the centre of the domain and retaining only the first two terms, yielding a linear expression. While this introduces quantitative errors, it often captures the systems qualitative behaviour correctly within the simplicity of a Cartesian coordinate system.

$$f = 2\Omega\sin(\theta_0) + \frac{2\Omega\cos(\theta_0)}{R}\delta y = f_0 + \beta y \tag{2.4}$$

where f_0 is the value of f at the center of the domain and β is the meridional derivative of f in the center of the domain.

In derivation of the QG equations the following assumptions are made to simplify Equations 2.1 to 2.3 (Olbers et al., 2012). QG theory assumes all terms to be small but isn't biased as to which of the various small parameters is the largest.

- A small Rossby number; $R_o = U/\Omega L$, where Ω is the rotation of the earth and U and L are a horizontal velocity and a length scale of the fluid motion respectively. This condition implies a large influence of the Earths rotation.
- The free surface elevation is small compared to the layer depth, $\eta/H \ll 1$ (this also allows $\frac{H}{H+\eta} \simeq 1 - \eta/H$).

- The β correction to the Coriolis parameter is assumed small ($\beta L/f_0 \ll 0$).
- $T \sim L/U$, implying the linear $\mathbf{u}_t$ term is also small compared to the Coriolis force.
- A small Ekman number, Ek, implying viscous forces are small compared to the Coriolis force.

The above assumptions reduce the momentum equations to a leading order balance between the Coriolis force and the pressure term.

$$-fv = -\frac{1}{\rho}\frac{\partial P}{\partial x} \tag{2.5}$$

$$fu = -\frac{1}{\rho}\frac{\partial P}{\partial y} \tag{2.6}$$

We now consider the pressure gradient term and assume a hydrostatic pressure distribution within the water column. The pressure difference at any two points at the same depth is, therefore, simply determined by the difference between η at the two points. This permits the pressure term to be rewritten in the following way as a function of the free surface gradient.

$$\frac{1}{\rho}\nabla P = g\nabla\eta \tag{2.7}$$

The substitution of Equation 2.7 into the x and y momentum equations introduces another variable, η. A third equation is sought to close the system and is obtained from mass-continuity in Equation 2.3. Shallow water assumptions require that $u_z, v_z = 0$, and thus by taking a z-derivative of the continuity equation it can be shown that $w_{zz} = 0$. For a flat bottom, w_{bottom} must be zero by the no-flux condition, and the vertical velocity of a particle on the surface is therefore the simply the Lagrangian derivative of the free surface elevation. The following expression is therefore found for w_z

$$\frac{\partial w}{\partial z} = \frac{1}{H+\eta}\frac{D\eta}{Dt}$$

which is substituted back into the continuity equation. Finally we have three governing equations in u, v and η.

$$\frac{Du}{Dt} - fv = -g\frac{\partial \eta}{\partial x} \tag{2.8}$$

$$\frac{Dv}{Dt} + fu = -g\frac{\partial \eta}{\partial y} \tag{2.9}$$

$$\frac{D\eta}{Dt} + (H+\eta)\nabla \cdot \mathbf{u} = 0 \tag{2.10}$$

As mentioned in the introduction, we are interested in a quantity called *potential vorticity*, and thus now consider the vorticity of the system. Since we are only considering two-dimensional velocity, then vorticity exists only as a scalar oriented in the z direction. There are two types of vorticity in a QG model. The first, the *relative* vorticity, ζ, is the vorticity associated with the local velocity field. It is defined as the gradient crossed with the velocity vector, and in two-dimensions oriented in the z-direction.

$$\zeta = \hat{z} \cdot (\nabla \times \mathbf{u}) = \frac{\partial v}{\partial x} - \frac{\partial u}{\partial y} \tag{2.11}$$

The *planetary* vorticity, as the name suggests, is the vorticity associated with the solid body rotation of the Earth. Its z component is given as $2\Omega \sin(\theta)$, which varies with latitude. The sum of the two, $f+\zeta$, is the *total* vorticity. An equation governing the transport of the total vorticity, Equation 2.12, is found by rearranging Equation 2.9, taking the x-derivative and subtracting from it the y derivative of Equation 2.8.

$$\frac{D}{Dt}(f+\zeta) + (f+\zeta)\nabla \cdot \mathbf{u} = 0 \tag{2.12}$$

Using Equation 2.10, and noting that $H_t = 0$, we find an equation for $\nabla \cdot \mathbf{u}$ in terms of the total height of the water column, $H+\eta$.

$$\nabla \cdot \mathbf{u} = -\frac{1}{(H+\eta)}\frac{D}{Dt}(H+\eta) \tag{2.13}$$

Equation 2.13 is substituted into Equation 2.12 to find the result for the shallow water potential vorticity in a one-layer system.

$$\begin{aligned}\frac{1}{f+\zeta}\frac{D}{Dt}(f+\zeta) - \frac{1}{H+\eta}\frac{D}{Dt}(H+\eta) &= 0 \\ \frac{D}{Dt}\ln(f+\zeta) - \frac{D}{Dt}\ln(H+\eta) = \frac{D}{Dt}\ln\frac{(f+\zeta)}{(H+\eta)} &= 0 \\ \frac{D}{Dt}\left(\frac{f+\zeta}{H+\eta}\right) = \frac{Dq}{Dt} &= 0 \end{aligned} \tag{2.14}$$

where q denotes the *potential vorticity* (PV). In this one-dimensional shallow water case it is equal to the total vorticity over the total height of the water column. It can equivalently be thought of as the circulation per unit volume (Cushman-Roisin, 1994). The conservation of PV following fluid parcels is an important result and useful for a qualitative understanding. Typically Equation 2.14 is rewritten in terms of a stream function, which we present in the following.

Using the leading order balance of the Coriolis and pressure terms in the u and v momentum equations (Equations 2.1 and 2.2), u and v can be estimated from η. This permits the relative vorticity, ζ, to be expressed in terms of η.

$$u = -\frac{g}{f_0}\eta_y \tag{2.15}$$

$$v = \frac{g}{f_0}\eta_x \tag{2.16}$$

$$\zeta = \frac{g}{f_0}\nabla^2\eta \tag{2.17}$$

We use the expression above for ζ and the β-plane approximation (Equation 2.4) for f in Equation 2.14. Noting that $D_t(f_0/H) = 0$ and retaining only the following three terms in the expansion with leading order magnitude, the expression in Equation 2.18 is found.

$$\begin{aligned}\frac{D}{Dt}\left[\frac{f_0}{H} + \frac{\beta y}{H} + \frac{g}{Hf_0}\nabla^2\eta - \frac{f_0\eta}{H^2} - \frac{\eta\beta y}{H^2} - \frac{\eta g}{H^2 f_0}\nabla^2\eta\right] &= \\ \frac{D}{Dt}\left[\beta y + \frac{g}{f_0}\nabla^2\eta - \frac{f_0\eta}{H}\right] &= 0\end{aligned} \tag{2.18}$$

Equation 2.18 allows a qualitative interpretation of the influences on the potential vorticity of a column of fluid. The first term inside the total derivative represents the gain or loss of planetary vorticity as fluid columns move northward or southward. The second term accounts for changes in relative vorticity as the local velocity field evolves. The last term is the vertical stretching or squeezing of fluid columns due to changes in the free surface elevation. Equation 2.18 is most commonly written in terms of a streamfunction. The streamfunction, ψ, has its usual meaning where:

$$v = \frac{\partial \psi}{\partial x}; u = -\frac{\partial \psi}{\partial y}$$

Note that η can also be rewritten in terms of ψ using the expressions for u and v in Equation 2.15 and 2.16.

$$\eta = \frac{f_0}{g}\psi \tag{2.19}$$

Using the above expressions, Equation 2.18 is found in terms of the stream function below, where J is the Jacobian operator:

$$\begin{gathered} \frac{D}{Dt}\left[\nabla^2\psi - \frac{f_0^2}{gH}\psi + \beta y\right] = 0 \\ \frac{\partial}{\partial t}\left(\nabla^2\psi - \frac{f_0^2}{gH}\psi\right) + J(\psi, \nabla^2\psi) + \beta\frac{\partial \psi}{\partial x} = 0 \qquad (2.20) \end{gathered}$$

Equation 2.20 is the *quasi-geostrophic potential vorticity equation* for a one-layer system. It is one equation in terms of one unknown, ψ. In principle the system is closed, however it cannot be solved analytically (in general) in time and requires the use of numerical methods. These modelling methods isolate the time derivative and integrate the entire system in time from initial conditions. Each time step involves, both updating the PV and an elliptic inversion to get ψ, given the PV. We discuss the numerical methods in more detail in Section 4.2.

2.1.2 Governing Equations of a Two-Layer System

As mentioned, in this project we use a two-layer model. We now extend the principles introduced in Section 2.1.1 to a two-layer system with bottom topography. We consider the system shown in Figure 2–2. The symbols retain their same meanings, where we now use subscripts 1 and 2 to refer to the upper and lower layers respectively. Note that we now have two interfaces: one at the free surface, denoted by η^S, and one at the interface between the two layers of fluid, η^I. Here $\rho_2 > \rho_1$ where it is assumed that $\rho_2 - \rho_1 \ll \rho_0$. Bottom topography, $\eta_b(x, y)$, is introduced into the bottom layer as a function of both x and y.

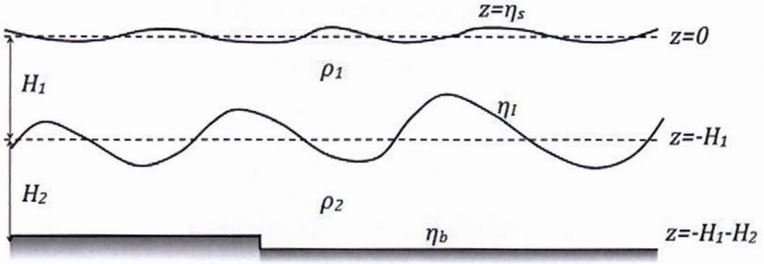

Figure 2–2: Representation and notation for two-layer quasi-geostrophic model with bottom topography

The fluid depth in the upper layer, d_1, is given by $H_1 + \eta^S - \eta^I$, and likewise in the lower layer $d_2 = H_2 + \eta^I - \eta_b$. The pertubation at the interface between the two layers, η^I, is related to the stream functions in the two layers, ψ_1 and ψ_2.

$$\eta^I = \frac{f_0}{g'}(\psi_2 - \psi_1) \tag{2.21}$$

In addition to the QG model assumptions in Section 2.1.1, we note that $\eta_b/H \ll 1$ (Kantha and Clayson, 2000) and $\eta^I/H \ll 1$ (Cushman-Roisin, 1994). Again we arrive at a leading order balance between the Coriolis force and the pressure term in the momentum equations in the two layers. Recall that in the one-layer case we derived an expression for the pressure term in terms of the interface gradient. In the upper layer we find the same expression as before for the pressure gradient term although now the pressure gradient in the lower layer is a function of both η^I and η^S.

$$\frac{1}{\rho}\nabla P_1 = g\nabla\eta^S \tag{2.22}$$

$$\frac{1}{\rho}\nabla P_2 = g\nabla\eta^S + g'\nabla\eta^I \tag{2.23}$$

where g' is the reduced gravity given by the following.

$$g' = \frac{\rho_2 - \rho_1}{\rho} g$$

Typically the two terms on the right-hand side of Equation 2.23 are roughly the same order of magnitude. That means to say that, although the reduced gravity is much smaller than the full g, disturbances at the interface have a much higher amplitude than that at the surface.

As in the one-layer case, potential vorticity is found to be conserved following fluid columns in each layer. In other words, $D_t q_i = 0$ where q_i is the potential vorticity in layer i as given below. Note that these can be compared with the one-layer analogy given in Equation 2.20.

$$q_1 = \nabla^2\psi_1 + \frac{f_0^2}{g'H_1}(\psi_2 - \psi_1) + f \tag{2.24}$$

$$q_2 = \nabla^2\psi_2 - \frac{f_0^2}{g'H_2}(\psi_2 - \psi_1) + f + \frac{f_0}{H_2}\eta_b \tag{2.25}$$

Similar to the one layer case, $\nabla^2\psi_i$ is the local spin or relative vorticity. In both equations, the second term on the right-hand side is the stretching term by the other layer. The ratio in front of this term is related to the Rossby radius of deformation, which we will introduce in the following section. f again accounts for the changes in the planetary vorticity of fluid columns. The last term in Equation 2.25 accounts for squashing of fluid columns moving over elevations in the bottom topography.

2.2 Barotropic and Baroclinic Instabilities

Ocean circulation is generally conceded to be mainly driven by the large scale, slowly varying, wind stress. Because typical length scales of associated with atmospheric winds are large compared to the ocean eddy field, this forcing does little to excite the eddies. Instead, the mesoscale eddy field results from instabilities of the large scale flow. QG dynamics admits two classes of instability; barotropic and baroclinic. A *barotropic* fluid is formally defined as a fluid in which density is a function of pressure only (Vallis, 2006). This simply means isopyncnal (constant density) surfaces and isobaric (constant pressure) surfaces are aligned. *Baroclinic* fluids encompass anything other than barotropic fluids. Note, however, that even if the fluid is baroclinic, barotropic instability may still exist. Essentially one can think of the overall flow as in terms of vertical modes; the gravest of which corresponds to the depth average. Barotropic instability acts on this mode, whereas baroclinic instability also involves the depth-dependant part of the flow.

2.2.1 Barotropic instabilities

Barotropic instabilities may develop in fluids of constant density, meaning buoyancy forces do not play a role in their dynamics McWilliams (2006). In the ocean, sloping sea floors or the meridional variation of the Coriolis parameter set up background PV gradients. These ambient gradients are able to sustain waves such as planetary and topographic waves (see Cushman-Roisin (1994)). As shear currents sustain a similar PV gradient they too permit the existance of waves. In this case, the baroclinic instabilities extract their energy from energy in the mean shear flow (Witter and Chelton, 1998).

We mention barotropic instability here mainly for completeness. In our QG model, the formation of the jets relates to barotropic dynamics but not so much to barotropic instability per se. The two-layer QG model does, however, admit baroclinic instability which we explain in following.

2.2.2 Baroclinic Instabilities

Baroclinic instabilities exist in environments with horizontal slopes in isopyncnal surfaces in rotating reference frames. For this reason they can only occur in stratified fluids. The ocean is stratified at all latitudes. Essentially, the abyss ocean is filled with waters having been made cold (and therefore dense) as a result of surface cooling, either in the deep ocean or along continental shelves. Surface waters in the Southern Ocean are also cold and dense; however, they remain buoyant compared to the abyssal waters. As such, the Southern Ocean, like all other major oceans is vertically stratified, and can be subject to baroclinic instability. In addition, horizontal density gradients also exist, being naturally set up by net heating in the tropic regions and net cooling in the polar regions (Salmon, 1998). The two processes lead to sloping isopycnals.

Consider Figure 2–3, in which isopycnals are sloping down towards the equator as in the Southern Ocean. The system contains potential energy which increases in magnitude as the slopes of the layers are increased. The horizontal stratification produces a driving pressure gradient towards the north. Unlike in classic fluid dynamics, the system may in fact be stable due to the opposing Coriolis force. The idea is similar to the slope on the free surface which stabilizes in a swirling bucket of water. However, as the isopycnals become steeper a critical slope is reached, beyond which the system is no longer stable. In this case the isopycnals undergo a slight relaxation, releasing some potential energy. It is this energy which feeds and drives the resulting baroclinic instabilities (Cushman-Roisin, 1994).

Even though the system in Figure 2–3 may have an overall unstable density structure, the system may be stable to vertical displacements of fluid parcels. Consider a perturbation swapping fluid parcels "A" and "C". Just as if the density stratification were horizontal, the two fluid parcels experience restoring forces and return to their original positions. In contrast, after swapping "A" and "B", "A" is both higher and more buoyant relative to its environment; therefore buoyancy would tend to push it further from its initial position. The lighter fluid being displaced higher, and the denser fluid being displaced lower means

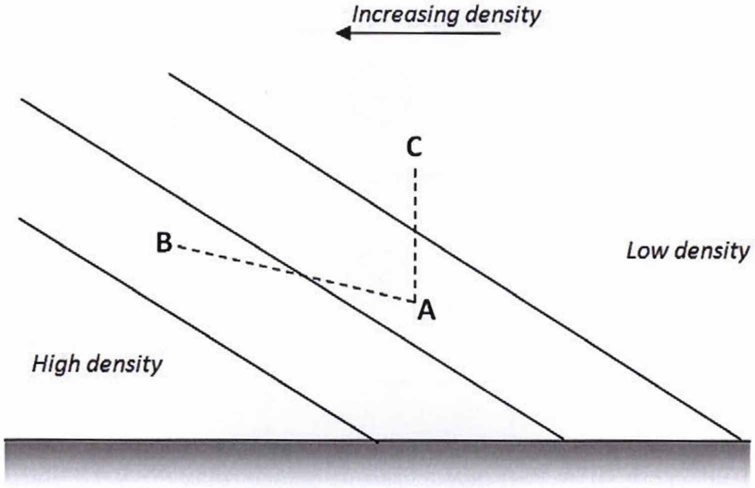

Figure 2–3: System giving rise to baroclinic instabilities, convention for southern hemisphere with increasing density towards the pole. Based on figure from Vallis (2006).

the system is now in a state with lower potential energy. This loss in potential energy is gained by the perturbation, fuelling its growth (Vallis, 2006).

Several approaches exist for baroclinic instabilities including, for example, the consideration of continuously stratified fluids. Given that our model is a two-layer system, we present here an analytic treatment for a system with two layers of constant density, commonly referred to as the Phillips problem. The system is shown in Figure 2–4 (again with conventions for the Southern hemisphere), where the interface between the two fluids has a slope uniquely in the meridional direction. As in the derivations of the QG equations, we assume the pressure to be hydrostatic. Note that this inherently means that any non-zero slope on the interface leads to a misalignment of isobars and isopycnals, and the flow falls into a baroclinic classification.

In the upper layer, the horizontal stratification generates a driving pressure gradient towards the south. In contrast, in the lower layer, the direction of the net pressure gradient depends on a balance between the density difference across the interface and the slope of

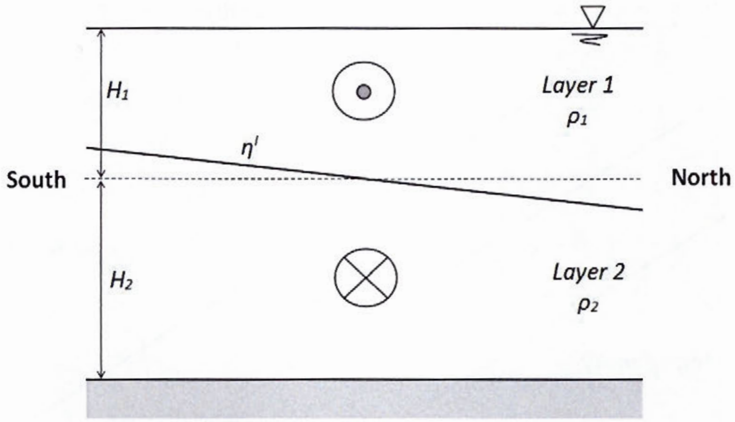

Figure 2–4: Initial state of a two-layer system which may lead to baroclinc instability. Convention is shown in the Southern hemisphere with the upper warmer layer increasing in thickness towards the equator.

the interface. If the slope is sufficiently steep then the driving pressure gradient is towards the south and the system is said to be baroclinically unstable. In this case, in the upper layer, a flow is initiated towards the south but is deflected towards the east (out of the page in the diagram) by the Coriolis effect. In the lower layer, a westward flow is generated. The opposing flows in the two layers produce a shear at the interface and generates baroclinic instabilities.

To determine this critical slope several textbooks take an approach using linear instability (e.g. Cushman-Roisin 1994; Salmon 1998). The QG equations are linearized to produce a steady state solution with constant zonal velocities in the two layers. We define the difference between the two velocities, or the shear velocity at the interface, to be U_{shear}.

$$U_1 - U_2 \equiv U_{shear} \tag{2.26}$$

The leading order balance in QG model between the Coriolis force and pressure term (Equation 2.6) allows the shear velocity to be rewritten in terms of the pressure gradient. The expression can then be related to the interface slope, η^I, using the relationship between the pressure gradient and η^I defined in Equation 2.23. This leaves us with a simple relationship directly linking U_{shear} to η^I_y.

$$U_{shear} = -\frac{1}{\rho_0 f} P_y = \frac{g'}{f_0} \bar{\eta}^{I}{}_{y} \tag{2.27}$$

As mentioned, the system is unstable if η^I_y, or equivalently U_{shear}, exceeds some critical value. The critical value represents the point, beyond which the potential vorticity gradient changes direction across the interface (McWilliams, 2006). The analytical critical value is simply given in Equation 2.28, while the analytic treatment can be found in Salmon (1998).

$$\frac{U_{shear}}{2} > U_{crit} \equiv \beta L_D^2 \tag{2.28}$$

Equation 2.28 introduces L_D, the Rossby radius of deformation (or sometimes referred to as the baroclinic radius of deformation). L_D is often interpreted as a length scale of an eddy resulting from baroclinic instability and in a two-layer system is given by the latter expression in Equation 2.29,

$$L_D^2 \sim \frac{g'D}{f_0^2} \equiv \frac{g' H_1 H_2}{f_0^2 (H_1 + H_2)} \tag{2.29}$$

where g' is the reduced gravity term, H_i is the depth of layer i, and f_0 is the Coriolis term evaluated in the centre of the domain. Here it is more correctly the *internal* deformation radius as it references the interior stratification. The use of the full gravitational acceleration relates to the free surface and is called the external deformation radius (McWilliams, 2006).

2.2.3 Relationship between baroclinic and barotropic instabilities

In our model, quasi-steady jets are formed by the interaction of both baroclinic and barotropic modes. To help explain the dynamics of their formation, we first define a length scale pertaining to the barotropic mode; the Rhines scale, L_{Rhines}. Recall that the barotropic mode can be thought of as a depth averaged flow, or with the absence of stratification and consider the barotropic equation shown in Equation 2.30.

$$\nabla^2\psi_t + J(\psi, \nabla^2\psi) + \beta\psi_x = 0 \tag{2.30}$$

L_{Rhines} can be thought of as a scale at which the β effect begins to have an important influence on the flow (Salmon, 1998). Mathematically, it is a length scale at which the non-linear advection and β terms in the barotropic equation are roughly equal. Using a scale analysis we scale the Jacobian term as $\sim U^2/L^2$ and the β-term as $\sim \beta U$, where U is a representative eddy velocity. Equating the magnitude of the two terms results in the dimensional argument in Equation 2.31, although sometimes it appears with varying coefficients of relation. For example, Thompson (2010) quotes a factor of 2π as the constant of relation and interprets it as the extent of meridional eddy mixing within a single geostrophic jet.

$$L_{Rhines} \sim \left(\frac{U}{\beta}\right)^{1/2} \tag{2.31}$$

Quasi-geostrophic jets are essentially formed by a movement of energy to larger scales. Instabilities are initially generated by baroclinic instability, with a length scale on the order of the Rossby radius of deformation, L_D. Unlike in the energy cascade in classic turbulence, in the ocean, the mechanism for vortex-stretching cannot exist due to the two-dimensionality of the flow. As a result energy cannot move to smaller scales and is shunted into the larger scales (Vallis, 2006), a process termed the inverse energy cascade. Eventually the eddies grow to a size on the order of the Rhines scale. Further growth is restricted due to the increasing restoring force provided by the β-effect (Rhines, 1975). The inverse energy cascade reaches its limit and the anisotropy of the system (due to β) means the turbulent energy is channelled into a field of zonal waves, or geostrophic jets (such as the ACC).

This can also be understood by considering the equations. For $L \ll L_{Rhines}$, β is irrelevant and the two-dimensional Navier-Stokes equations in a stationary reference frame are recovered. The non-linear term leads to an upscale of the energy cascade and, eventually, as the turbulent scales grow, the β term becomes more important. As β becomes even more important, $L \gg L_{Rhines}$, leading to a quasi-linear (weakly non-linear) system. Due to this, long term integrations of freely evolving turbulence tend to organize into quasi-zonal jets.

Chapter 3
Literature Review

3.1 Mass transport by mesoscale eddies

3.1.1 The role of mesosale eddies

Mesoscale eddies are large rotating stuctures, on the order of 100km (Rhines, 2001), evolving over time under a strong influence from the Earth's rotation. They grow over time scales estimated to be anywhere from 30 days south of Australia to closer to 60 days in Drake Passage (Phillips and Rintoul, 2000). Mesoscale eddies dominate the kinetic energy budget. Their total kinetic energy is estimated to often be on the order of ten times that contained in the mean flow (Vallis, 2012) (note, however, that PE is dominated by the large scale features). These eddies transport properties such as heat and tracers and act to fragment and irreversably mix the flow. Specifically in the Southern Ocean, mixing attributed to mesoscale eddies dominates cross-frontal transport (Eden, 2006).

Mesoscale turbulence is largely non-isotropic owing to the strong stratification (Dukowicz and Greatbatch, 1999) and subsequently mixing occurs much more easily along isopycnal surfaces of constant potential density than across them (Gent, 2011). Within isopycnal layers, the transport of tracers or other properties is realized by an effecive transport velocity which is the sum of mean flow and eddy velocity components (Gent et al., 1995). In coarse-grained models, the grid size is larger than the Rossby radius and thus unable to resolve these mesoscale eddies evolving from baroclinic instability. It is common practice to parameterize this effective eddy transport velocity, particularly in longer running models (Treguier et al., 1997). This is commonly achieved using an eddy diffusivity.

3.1.2 Mass transport within an isopycnal layer

In the ocean, a large amount of scalar transport can often be attributed to changes in isopyncal layer thicknesses. Consider an isopycnal layer with a high concentration of a given scalar. If the thickness of this layer is reduced, then in a global sense, one can think of the scalar as being effectively "dispersed" horizontally (Dukowicz and Greatbatch, 1999). Using the same logic, an increase in layer thickness can be thought of as an inward flux of the scalar. For this reason, changes in isopycnal thicknesses, or equivalently mass transport within isopycnals, is often considered to be important in scalar transport.

To derive the mass transport within an isopycnal layer consider the velocity and interface elevation to have two components; a time-mean component denoted with an overbar and a fluctuating eddy component denoted with a prime. The total layer thickness, h, is given by the sum of the average depth of the layer and the interface pertubation, $h = \overline{h}+\eta'$. Similarly, the total velocity is the sum of the two components, $\mathbf{u} = \overline{\mathbf{u}} + \mathbf{u}'$. Note that both $\overline{\eta'}$ and $\overline{\mathbf{u'}}$ are zero. The mean mass transport within a layer can found by multiplying the velocity by the layer height and taking a time average.

$$\overline{\mathbf{u}h} = \overline{\bar{\mathbf{u}}\bar{h}} + \overline{\bar{\mathbf{u}}h'} + \overline{\mathbf{u}'\bar{h}} + \overline{\mathbf{u}'\eta'} \tag{3.1}$$

$$= \bar{\mathbf{u}}\bar{h} + \overline{\mathbf{u}'\eta'} \tag{3.2}$$

In the first expansion, the first term on the right-hand side is mass transport by the mean flow in the mean layer thickness. The following two terms are zero in taking a time-average. The final term is a correlation of two fluctuating quantities. It is the mass transport by the mesoscale eddies. This term is analogous to the Reynolds stress or turbulent scalar flux in the Reynolds Averaged Navier-Stokes (RANS) equations in classic turbulence (e.g. Pope 2000; Tennekes and Lumley 1972). In coarse-grained models the mean flow is resolved; however, the $\overline{\mathbf{u}'\eta'}$ is unresolved and requires parameterization. Often this thickness-velocity correlation is expressed as a velocity. The Bolus velocity of layer i,$\mathbf{u}_i^b$, is defined as $\overline{\mathbf{u}'\eta'}$ divided by the average layer thickness. The GM90 parameterization appears in the tracer equation in the form of the Bolus velocity. In these applications, $\mathbf{u}_i^b$ may be added to the Eulerian time mean, $\bar{\mathbf{u}}_i$ to give an effective advective velocity for scalar transport.

$$\mathbf{u}_i^b = \frac{\overline{\mathbf{u}'_i\eta'}}{\overline{H_i}} \tag{3.3}$$

3.1.3 GM90 parameterisation of mass fluxes

Here we introduce the most common model to estimate $\overline{\mathbf{u}'\eta'}$, or equivalently the Bolus velocity. Currently, the model proposed by Gent and Mcwilliams (1990) and later clarified by Gent et al. (1995) is the most commonly employed (Farneti et al., 2010). Often in the literature it is referred to simply as the GM90 isopycnal tracer mixing parameterization.

Recall that baroclinic instabilities are fed by and reduce the potential energy contained in sloping isopycnal surfaces (Section 2.2.2). It seems sensible to assume that mesoscale eddy transport could therefore be related to this energy source. In other words, it predicts that if baroclinic eddies are generated to relax baroclinically unstable isopycnal surfaces then the amount of mixing by the baroclinic eddies is related to how much energy is released by the relaxation of the isopycnals. Steeper isopycnals are therefore able to supply more energy. It is the relaxation of these isopycnals which is modelled by a down-gradient Fickian diffusion process. Based on a gradient transport hypothesis (see Pope 2000; Tennekes and Lumley 1972), the height fluxes can be related to the interface gradient as in Equation 3.4 where κ is the eddy diffusivity.

$$\overline{\mathbf{u}'\eta'} = -\kappa \boldsymbol{\nabla}\overline{\eta} \tag{3.4}$$

This eddy diffusivity model is relatively simple to implement in the oceans interior, however it runs into problems where isopycnals outcrop at the surface (Nurser and Lee, 2004). Additionally there is some suggestion that κ should be matched to the integration time of the model (Nakamura and Chao, 2000).

Note that both $\overline{\mathbf{u}'\eta'}$ and $\nabla\overline{\eta}$ are vectors in Equation 3.4. The equation is mathematically correct if κ is a scalar, but also if κ is written as a tensor. As a scalar, κ could be taken as a constant or permitted to vary. Often in climate models it is taken as a constant in space (Eden, 2006). That said, several authors argue that κ varies spatially and should be diagnosed from the large-scale density structure resolved in the model (e.g. Nakamura and Chao 2000). In isopycnal coordinates κ can be written as a two-by-two matrix with entries, α_i. The matrix can be rewritten into four separate matrices which lend themselves to a physical interpretation.

$$\kappa = \begin{pmatrix} \alpha_1 & \alpha_2 \\ \alpha_3 & \alpha_4 \end{pmatrix} = \begin{pmatrix} \kappa_0 & 0 \\ 0 & \kappa_0 \end{pmatrix} + \begin{pmatrix} 0 & -\kappa_{skew} \\ \kappa_{skew} & 0 \end{pmatrix} + \begin{pmatrix} \alpha & 0 \\ 0 & -\alpha \end{pmatrix} + \begin{pmatrix} 0 & \beta \\ \beta & 0 \end{pmatrix} \tag{3.5}$$

The κ_0 matrix quantifies height diffusivity due to downgradient Fickian diffusion, or alternatively also called the across iso-surfaces flux. The second matrix on the right-hand side with coefficients of κ_{skew} is the flux along iso-surfaces or perpendicular to the gradient. It is often formally called the skew flux (Vallis, 2006). Note in passing that it is the diffusive flux, oriented in the direction of the gradient which acts to reduce variation (if $\kappa_0 > 0$), in contrast the skew flux is perpendicular to the gradient. α and β characterize anisotropies of the two diffusion mechanisms.

3.1.4 Scalar transport in non-eddy resolving models

In coarse grained models, scalar transport is often modelled by Equation 3.7 where Θ is the mean scalar field.

$$\frac{D}{Dt}\Theta = \nabla \cdot (\kappa \nabla \Theta) \tag{3.6}$$

$$\Theta_t + \underset{\sim}{\overline{\mathbf{v}}} \cdot \nabla\Theta + = \kappa \nabla^2 \Theta \tag{3.7}$$

Gent and Mcwilliams (1990) proposed the effective advective velocity, $\underset{\sim}{\overline{\mathbf{v}}}$, should be written as the sum of the mean and an effective eddy velocity, the Bolus velocity.

$$\Theta_t + \overline{\mathbf{u}} \cdot \nabla\Theta + \overline{\mathbf{u}}_{bolus} \cdot \nabla\Theta = \kappa \nabla^2 \Theta \tag{3.8}$$

More formally the expansion of $\nabla \cdot (\kappa \nabla \Theta)$ to $\kappa \nabla^2 \Theta$ in Equation 3.7 contains another term, $\nabla\kappa \cdot \nabla\Theta$. Since it contains the gradient of κ, it is identically zero if κ is non-varying in space.

To maintain generality the term could be absorbed into the Bolus Velocity. Although we will not compute this term in the present work, it provides a motivation to test whether κ varies in space. Modelled using an eddy diffusivity, the Bolus velocity is then rewritten as the sum of two terms in Equation 3.9 for a two-layer system.

$$\mathbf{u^b}_i = \frac{\kappa \nabla \bar{\eta}}{\overline{H_i}} - \nabla \kappa \tag{3.9}$$

We mention the Bolus velocity here for completeness; however, we will present our results largely in terms of mass fluxes and κ. Nonetheless, Equation 3.9 clearly shows the strong dependence of turbulent mass transport on κ and potentially its spatial variation.

3.2 ACC dynamics and mixing

We gave a short introduction to the ACC and its importance in Section 1.1. Here we focus the discussion on the dynamics of the ACC, and in particular the transport of scalars or other properties. Recall that the ACC is the strongest and only zonally reconnecting ocean current. The quasi-steady jets which compose the ACC are sustained by two main energy sources. The first, a momentum source to the current, are the strong westerly winds over the ocean surface in the Southern Ocean. This wind momentum is believed to be transferred vertically to deeper waters by isopycnal form drag (e.g. Wolff et al. 1991; Straub 1993), and secondarily by the horizontal Reynolds stress divergence (McWilliams and Chow, 1981). Furthermore, a meridional density gradient is maintained in the Southern Ocean through differential surface heating, freshwater fluxes and wind-driven Ekman pumping to the north of the ACC and upwelling of cooler water on the poleward side (Kuhlbrodt et al., 2012). This density gradient is recognized as a source of potential energy to the current (Gille, 2002; Pedlosky, 1963).

Earlier we introduced the idea that the ACC is believed to be a barrier to mixing. Most commonly, the inhibition is believed to be due to the conservation of PV. This can be understood by considering a simple zonal jet with some $\overline{u}(y)$. Note that one side of the jet has positive relative vorticity and the other has negative. In this sense, it is difficult for Lagrangian particles conserving vorticity to move from one side to the other, and in fact doing so would disrupt the jet structure. In the ocean it is not relative vorticity but PV that is conserved (PV for a one-layer system was defined in Equation 2.14). The ideas are similar although the β-effect now introduces an ambient PV gradient in the y direction.

Literature on ACC mixing and its dynamics is a combination of both observations and numerical simulations. Early models of the ACC were motivated to confirm observations in the field. Typically they took the form of a 2-layer quasi-geostrophic model in a zonally-reentrant channel and bounded by walls to the north and south. These simple two layer models produced the same flows in the upper layer as that observed at the surface in the Southern Ocean; peak velocities in the jet cores, alternating with regions of wider and weaker Eastward flow (McWilliams and Chow, 1981).

Here we gives details about the parameterization of mixing in the Southern Ocean and its spatial and depth variation. The literature is most often concerned with eddy transport in the meridional direction as transport in the zonal direction is dominated by the mean flow. Most commonly, authors try to form a link between the mixing structure, or equivalently κ, and mean flow properties.

3.2.1 Representation of the ACC in non-eddy resolving models

The majority of non-eddy resolving models use parameterizations for mesoscale eddy transport based on the ideas initially proposed by Gent and Mcwilliams (1990) and introduced here in Section 3.1.3. In the GM90 parameterization, transport is either a linear function of the density field or quadratic in the case where κ is time-varying and diagnosed from the stratification (Wang et al., 2011). The Southern Ocean is particularly sensitive to parameterization due to its widespread outcropping of isopycnal layers at the surface and consequently κ is very influential in terms of modelling results. In fact ACC transport is more strongly correlated with the choice of κ than zonal wind stress maximums (Kuhlbrodt et al., 2012).

The determination of a suitable κ is made even more difficult by the inability to obtain direct observations of eddy mixing in the oceans' interior. That said, it is possible to make estimates of mass fluxes from surface measurements (e.g. Phillips and Rintoul 2000). The spatial variability of these mass fluxes and κ is even harder to resolve from physical measurements. This means the methods of estimation, and hence resulting estimates, of κ in the Southern Ocean are very varied in the literature. In the most recent Intergovernmental Panel on Climate Change assessment in 2007, results were published with ACC transport varying over a factor of close to 10 (Kuhlbrodt et al., 2012). The next IPCC Fifth Assessment Report begins to allow resolutions as fine as 1/3° and resolution of eddies. Even so, it is still too computationally expensive for flows with a large number of tracers. For this reason the GM90 parameterization is expected to remain in use at least for the foreseeable future (Kuhlbrodt et al., 2012).

In modelling, usually the meriodional transport is of principal concern since the zonal transport is dominated by the mean flow and since one is often interested in the meridional transport of tracers. Typically κ is taken as a positive constant indicating the relaxation of isopycnals. A negative κ would be physically interpreted as eddies acting to increase rather than decrease the available potential energy (Eden et al., 2007). This is contrary to baroclinic instability theory (see Section 2.2.2). We present some eddy diffusivity values in the Southern Ocean found in the literature in Table 3–1. Note that in the Southern Ocean, cooler waters in the polar region and warmer waters in the mid-tropics set up isopycnals sloping down towards the equator. A positive κ therefore corresponds to northward transport (see Equation 3.4).

Table 3–1 shows eddy diffusivities with a huge variation. We discuss the spatial and depth distribution of κ on a more local scale within the structure of the jets which make up the ACC.

Table 3–1: Eddy Diffusivities in the ACC

Author	Means of Estimation	Estimated Eddy Diffusivity
Eden 2006	Eddy-resolving MOM2 with 42 vertical layers	Surface Values of 200 $\mathrm{m^2/s}$ poleward of polar front, 600 $\mathrm{m^2/s}$ between 60-45°, 3000 $\mathrm{m^2/s}$ between 45-35°
Marshall et al. 2006	Numerical advection using surface velocities from satellite altimetry	Surface Values of 500 $\mathrm{m^2/s}$ in jet axes up to 2000 $\mathrm{m^2/s}$ on Equatorial flanks
Naveira Garabato et al. 2011	Application of mixing length theory (Ferrari and Nikurashin, 2010) to altimetric data	200 $\mathrm{m^2/s}$ in upper kilometer within ACC jets, 2000 $\mathrm{m^2/s}$ in inter-frontal regions

Spatial Variation in κ

The spatial variation of κ in the literature is not clear, with seemingly contradictory arguments. For example, Sallée et al. (2008) suggest a relationship where a Lagrangian κ is proportional to the square-root of eddy kinetic energy (EKE). As the mean kinetic energy (MKE) shows a similar large scale structure to the EKE, they find higher diffusivities through the ACC than closer to the continents. Shuckburgh et al. (2009) on the other hand argues EKE can not completely explain κ; they instead find κ to be suppressed in regions of high mean flow where EKE is high.

This argument of local suppression in the jet cores is supported by other authors. Marshall et al. (2006) numerically advects a tracer in the ACC's surface flow determined by satellite altimetry. They compute eddy diffusivities from the evolution of the tracer field using a method originally published by Nakamura (1996). The approach amplifies the molecular diffusivity according to the distortion of scalar contours by the eddies. They find regions of low eddy diffusivities in regions of high PV gradients and higher eddy diffusivities in regions of low PV gradient.

Ferrari and Nikurashin (2010) takes a more analytical standpoint to look at meridional mixing across the ACC. They link the eddy diffusivity to the mean current speed using an idea loosely based on mixing length theory. The mixing length, l, is reduced according to to the mean flow velocity in which the eddies are advected. Suppressed mixing is predicted through the jet cores where the mean flow is fast enough to "..advect the tracer out of the eddy faster than the eddy lifetime and hence reduce the time for which eddies can stir the tracer." Naveira Garabato et al. (2011) uses this analytic framework on altimetric data, predicting κ to be suppressed by an order of magnitude within the ACC compared to the inter-frontal regions. This large scale variation in κ is derived from the large scale variation in the mixing length field, l. Although the mixing length theory may seem like a completely different idea, the same regions in the jet cores of mixing length suppression are incident with regions of high PV gradient.

3.2.2 Depth Variation of κ

The two-layer model that we will use in this study will limit our ability to look at the structure of κ in the vertical profile. Nonetheless, a basic understanding of the depth variation of κ will allow us to compare our results to values of κ in Table 3–1, which are mainly concerned with surface values. The zonal velocity of the ACC has a vertical structure with peak velocities near the surface and decaying rapidly within the upper kilometer or so.

Like the spatial variation, the depth variation of κ is also a little complicated. Overall, κ is found to be maximum within the upper 500m, dropping to close to zero below 2500 m (Eden, 2006). Recall that κ was related to MKE by Sallée et al. (2008). Given the higher velocities closer to the surface, then the result that κ is also generally higher close to the surface is in agreement. The level inhibition through the jet cores also varies with depth and is maximum where the mean current speed peaks (Abernathey et al., 2010). As the mean current speed decays with depth there exists a point where it matches the phase speed of the eddies. It is suggested that this permits an enhanced level of mixing (Ferrari and Nikurashin, 2010; Abernathey et al., 2010).

Bottom topography also affects the vertical mixing profile with local peaks in diffusivity occurring where the ACC negotiates topography (Sallée et al., 2008; Thompson and Sallée, 2012). In the vertical profile, peaks in κ are observed where jets merge together to negotiate bathymetry (Lu and Speer, 2010). Given that our model includes bottom topography it is valuable to discuss in more detail the effect of topography in the following.

3.3 Influence of topography

Early simulations of the ACC with bottom topography were carried out using wind-driven two-layer quasi-geostrophic models (e.g. Wolff et al. 1991; McWilliams et al. 1978). These aimed mainly to qualitatively explore the flow field formed under different conditions and the energy transfer within the system. In these simulations, the eddy field has a large barotropic component with large eddies in the lower layer (Wolff et al., 1991; McWilliams et al., 1978). Bottom topography sheds standing eddies which can be seen in the time mean flow (Wolff et al., 1991). They initiate a bottom form stress which is physically due to bottom pressure variations which are out of phase with zonal topographical variations (Olbers et al., 2012). This drag is responsible for a large proportion of the momentum removal in the ACC (Straub, 1993).

Later modelling efforts includes Merryfield and Holloway (1999) and Witter and Chelton (1998). Again they employ wind-driven two-layer QG models with ridges orientated perpendicular and parallel to the flow. A zonal ridges steers the jet along contours of constant f/H_n where H_n is the time mean thickness of the layer n (Witter and Chelton, 1998). This gives rise to a separation of the jet core between the two layers, increasing baroclinic shear at the interface. At these locations of topographical shifts, increased EKE is observed. Merryfield and Holloway (1999) impose an idealistic ridge and sea-mount in their simulations. They do not find their simulation results to support an eddy diffusivity hypothesis. The imposed topography causes eddies to form mean isopycnals which reflected the bottom bathymetry. The eddies drive the system towards a higher-entropy state consistent with the bottom topography. This is contrary to the thickness diffusivity approach of Gent et al. (1995), which assumes the system to tend towards zero entropy through a relaxation of isopycnal surfaces.Their paper suggests that rather, eddy thicknesses should be proportional to $\nabla(\Omega - \Omega*)$ where Ω is the entropy of the system and $\Omega*$ is the topographically correlated entropy state.

Using smaller scale and more regular topography, Thompson (2010) explores the influence of bottom bathymetry on jet formation and mixing in the ACC. The influence of topography is proportional to a ratio between the Rhines scale over a topographic length scale, L_{Rhines}/L_t. When the ratio is greater than unity, the positions of the jets become largely fixed in space by the topography with little temporal meandering (Thompson, 2010).

More recently, Thompson and Sallée (2012) imposed large scale topographic features in a two-layer QG model and our work will draw many ideas from theirs, particularly in terms of the model set-up. Their bottom bathymetry consists of a ridge with variation in the meridional and zonal direction. The ridge is varied to stretch from 0% of the domain to the full extent. In the simulations where the ridge occupies only a portion of the domain, the zonal jets shift northward in the lee of the topography (and vice-versa when the jets move back up onto the ridge). For the conservation of PV, the meridional meander provides a change in planetary vorticity to compensate for a change in layer thickness. They show jet axes to track along streamlines. Although this may seem intuitive, it might also be possible for a jet core, defined by a maximum local $\overline{u}$, to shift relative to streamlines as streamlines diverge and come together. Whereas, in the case where the centre of the jet corresponds to a streamline it is much harder to imagine cross-jet transport.

They evaluate cross-jet transport in relation to these large topographic features. Their numerical analysis takes a different approach to what we will ultimately use in this project, deriving cross-jet transport from probability distribution functions of instantaneous PV fields. They find the meridional exchange of fluid parcels is maximum where the jet breaks down, and this tends to be in the lee of the topography. They relate this back to the physical topography along the ACC, predicting that 75% of cross-jet transport is localized to a mere 20% of the zonal extent of the ACC. Again to assess the localization of cross-jet transport by topography, Naveira Garabato et al. (2011) evaluates the variation of mixing suppression in the jets cores using altimetric data and the mixing length method proposed by (Ferrari and Nikurashin, 2010). Reduced mixing suppression is observed where the jets undertake sharp meanders to negotiate topography, terming these regions as "leaky jets". These two recent studies (Thompson and Sallée 2012; Naveira Garabato et al. 2011) highlight the importance of these large scale topographic features in mass transport. We are interested in how these large scale distributions in mass transport map back to large scale distributions in the GM90 eddy diffusivity.

3.4 Long-term changes in the ACC

Over the twenty-first century the density gradient in the Southern Ocean is predicted to strengthen. The response of the ACC to future atmospheric changes is of high importance in climate change studies, particularly to Southern Ocean circulation, global meridional overturning, global heat and carbon budgets (Wang et al., 2011). Modelling attempts have produced considerable discrepancies and are heavily reliant on the choice of κ in non-eddy resolving models. The bottom bathymetry may play a role in spatial shifts of the ACC and how it may impact the meridional transport under new conditions is also unclear (Wang et al., 2011; Sen Gupta et al., 2009). An insight into the sensitivity and dependence of κ on both bottom topography and the meridional density structure is essential for predicting the evolution and potential feedback mechanisms of mass transport across the ACC.

Chapter 4
Methods

4.1 Model

4.1.1 Overview

Our model of the ACC is based on the two-layer QG equations derived in Section 2.1.2. Here we use a re-entrant channel with doubly periodic boundary conditions. Recall that the theory gives that the PV in each layer, q_i, is conserved following fluid parcels. Numerically it is expressed in Equation 4.1. The rearrangement in Equation 4.2 is used to integrate the solution in time.

$$\frac{Dq_i}{Dt} = F - D \tag{4.1}$$

$$\frac{\partial q_i}{\partial t} = -J(\psi_i, q_i) + F - D \tag{4.2}$$

where F and D are the forcing and dissipation in the model respectively. At statistical equilibrium, $F - D$ is roughly equal to zero in a global sense, giving $D_t(q_i) \simeq 0$. Note, however, that this is typically not true locally due to the differing spatial structures of F and D. In the first rearrangement we can see that the magnitude of F and D governs the energy contained in the system at steady state. This in turn affects the size and strength of the jets formed at steady state; we will talk about this in more detail in Section 5.1.2.

Although the actual ACC is driven by wind and buoyancy, we will consider an idealized forcing based upon the classic Phillips problem. Rather than imposing a forcing per se, we impose a base state. Because we specify the base state such that it is unstable, this produces eddies which are ultimately dissipated in the model via bottom drag and a hyperviscous term. In other words, the imposed forcing is implicit and represents what is required to maintain the base state.

For simplification, a rigid lid approximation is applied to the upper surface. Physically, this means omitting the vortex stretching term caused by displacement at the free-surface and is a reasonable assumption in the ocean (Salmon, 1998). It is implemented by amplifying the gravitational acceleration term at the surface.

4.1.2 Forcing

Our forcing imposes a base state by generating an imposed shear at the interface between the two layers. Equivalently, it can be thought of as inclining the interface between the two layers. The base-state PV in the two layers, Q_1 and Q_2, are given below. ζ does not appear as it is zero by definition and η_b is the bottom topography.

$$Q_1 = \beta y - \frac{f_0^2}{g'H_1}(\psi_1 - \psi_2) \tag{4.3}$$

$$Q_2 = \beta y - \frac{f_0^2}{g'H_2}(\psi_2 - \psi_1) + \frac{f_0}{H_2}\eta_b \tag{4.4}$$

Noting the shear velocity as $U_{shear} = U_1 - U_2$ and taking the meridional derivative leads to the following rearrangement. Note that from now on we drop the I superscript on η indicating the interface between the two fluids. The shear is implemented in the model by replacing β with an effective term, β_{eff}, which absorbs the effects of the interface gradient. To emphasize, β has the same magnitude in the two layers, whereas, β_{eff}

$$Q_{1y} = \beta + \frac{f_0^2}{g'H_1}(U_1 - U_2) = \beta + \frac{f_0\bar{\eta}}{H_1} = \beta_{eff} \tag{4.5}$$

$$Q_{2y} = \beta - \frac{f_0^2}{g'H_2}(U_1 - U_2) = \beta - \frac{f_0\bar{\eta}}{H_2} + \frac{f_0}{H_2}\eta_{by} = \beta_{eff} + \frac{f_0}{H_2}\eta_{by} \tag{4.6}$$

In the top layer $\bar{\eta_y}$ acts to reinforce β and Q_{1y} is always positive. In the bottom layer, the imposed interface gradient acts to oppose β and the overall sign of Q_{2y} depends on the magnitude of $\bar{\eta_y}$. According to the Phillips problem, the system is unstable when $\langle Q_{2y} \rangle < 0$. We choose amplitudes of $\bar{\eta_y}$ to meet this condition, causing the growth of baroclinic instabilities. Note that we later find the system is unstable at small positive values of $\langle Q_{2y} \rangle$ (see below).

We choose to define a variable to describe "how unstable" the flow is so that we can cleanly compare results with different forcing levels. We term this the forcing factor and denote it as F_f and define it in Equation 4.7. F_f is simply the ratio of the imposed shear to the critical shear. We will later find that our set-up has a different instability condition than the classic Phillips problem (see Section 5.1.1) and choose to define F_f based on the onset of instability U_{onset} for our parameters. $F_f = 1.0$ therefore corresponds to a marginally stable system.

$$\frac{U_{shear}}{2} = F_f U_{onset} \tag{4.7}$$

The induced velocity in each layer is computed as below, so that depth integrated velocity (or equivalently barotropic mode velocity) is zero. In our case,$H_1 = H_2$ and the velocities are equal and opposite.

$$\begin{aligned} U_1 &= \frac{H_2}{H_{tot}} U_{Shear} \\ U_2 &= \frac{H_1}{H_{tot}} U_{Shear} \end{aligned} \tag{4.8}$$

4.1.3 Energy Removal

Energy is removed from the model to maintain stability of an equilibrium state. It is removed in two ways, the sum of which permits a dynamic balance with the energy added by the forcing term. D_i represents the dissipation in layer i and is given in Equation 4.9.

$$D_i = A_h \nabla^6 \psi_i + \delta_{i2} r \nabla^2 \psi_2 \tag{4.9}$$

where δ_{i2} is the Kronecker delta. The first term on the right hand side represents energy removal via hyperviscosity in both layers and the latter is bottom drag in the lower layer.

Small scale dissipation is implemented using hyperviscosity, using bi-harmonic friction like several other authors (e.g. Merryfield and Holloway (1999); Wolff et al. (1991)). The constant, A_h, in Equation 4.9 is the bi-harmonic viscosity coefficient. Energy is removed from the small scales to prevent the build up of small scale noise and instability of the model and of entropy which is transferred towards higher wavenumbers. Whereas viscosity scales with the fourth derivative of the streamfunction, hyperviscosity scales with the sixth derivative. The sensitivity of hyperviscosity at small scales makes it highly effective for removing the small scale energy.

Energy removal in the bottom layer by bottom drag is modelled using Rayleigh damping. It scales with the second derivative of the stream function in the bottom layer where r is the bottom drag coefficient in Equation 4.9. We use a typical value of r of 10^{-7} $\mathrm{s}^{-}1$ (e.g. Merryfield and Holloway 1999; Nadeau 2011). The bottom Rayleigh drag is not scale selective; it damps energy equally from all horizontal scales.

4.1.4 Topography

Topography is added to the model using a function adopted from Thompson and Sallée (2012). Its shape is defined by a sinusoidal shape in the meridional direction and a hyperbolic tan function in the zonal direction.

$$\begin{aligned} \eta_b(x,y) &= \frac{h_0}{2} X(x) Y(y) \\ Y(y) &= \left[1 - \cos\left(\frac{2\pi y}{L_y}\right)\right] \\ X(x) &= \left[1 - \frac{\tanh[(x - L_x/2 + \gamma)/\sigma] - \tanh[(x - L_x/2 - \gamma)/\sigma]}{2\tanh(\gamma/\sigma)}\right] \end{aligned} \tag{4.10}$$

γ defines the zonal extent of the ridge in the domain. Here we use a constant value of $L_x/4$, corresponding to a ridge over half of the domain. σ is a parameter determining the slope of the *tanh* function on the two flanks. A value of $5L_D$ is used, equivalent to that by Thompson and Sallée (2012). h_0 is the total amplitude of the ridge from its lowest to highest point.

We found a topography of the form $\eta_b(x,y)$ to be preferable over a more simplistic form with only zonal or meridional dependence, that is $\eta_b(x)$ or $\eta_b(y)$, such as that used by Merryfield and Holloway (1999). Recall that our model uses a periodicity condition in the x and y directions to simplify the numerical implementation. Given that the ACC is almost purely zonal in many regions, the periodicity assumption and our results would only be valid if our model produced no net mean flow in the meridional direction. An early test run using a simple one-dimensional ridge, $\eta_b(x)$, produced a non-zero northward flow in the upper layer. The adoption of the two-dimensional topography, described here, was able correct this problem.

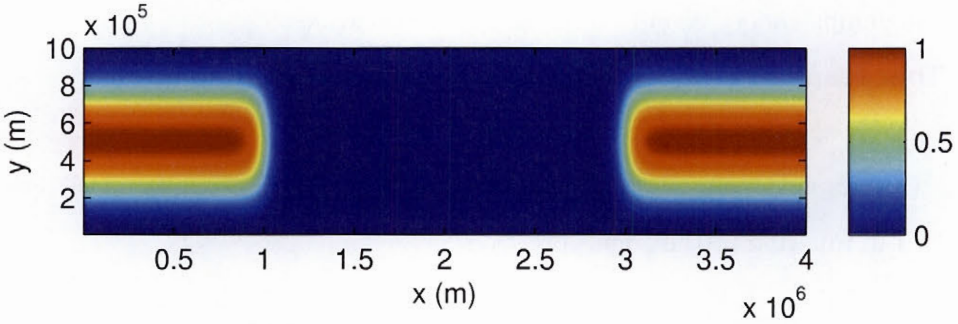

Figure 4–1: Bottom ridge topography used for all simulations. Scale shown is η_b/h_0, where h_0 is varied in the simulations.

4.1.5 Model Equations and Parameters

Our domain is doubly periodic with physical dimensions of 4000km zonally by 1000km in the meridional direction. All simulations are carried out at a resolution of 1024 by 256, producing a square resolution, i.e. $dx = dy$. The Rossby radius of $L_y/64$ means the spatial resolution can effectively capture baroclinic instabilities. The model equations are shown below with all parameters given in Table 4–1. The last two parameters in the table are those varied in the simulations. Note that a further set of simulations will be carried out for a flat bottom at a larger L_D in Section 5.6. For these runs L_D and its corresponding g' are shown in parentheses.

$$q_1 = \nabla^2\psi_1 + \frac{f_0^2}{g'H_1}(\psi_2 - \psi_1) + f_0 + \beta_{eff}y \tag{4.11}$$

$$q_2 = \nabla^2\psi_2 + \frac{f_0^2}{g'H_2}(\psi_1 - \psi_2) + f_0 + \beta_{eff}y + \frac{f_0}{H_2}\eta_b \tag{4.12}$$

$$\frac{Dq_i}{Dt} = -r\delta_{2i}\nabla^2\psi_2 - A_h\nabla^6\psi_i \tag{4.13}$$

Table 4–1: Model parameters

Parameter	Symbol	Value	Units
Zonal domain width	L_x	4000	km
Meridional domain width	L_y	1000	km
Rossby radius of deformation	$L_D = L_y/64(L_y/32)$	15.6 (31.3)	km
Upper layer depth	H_1	2000	m
Lower layer depth	H_2	2000	m
Physical resolution	dx, dy	3.91	km
Time-step	dt	1	hr
Coriolis Parameter	f_0	-1 x 10^{-4}	s^{-1}
Beta Parameter	β	2.0 x 10^{-11}	$m^{-1}s^{-1}$
Rayleigh Bottom Friction Coefficient	r	1 x 10^{-7}	s^{-1}
Upper layer density	ρ_1	1000	$kg.m^{-3}$
Reduced Gravity	g'	0.0024 (0.0098)	m^2/s
Bottom Drag Coefficient	r	1 x 10^{-7}	s^{-1}
Bi harmonic dissipation coefficient	$A_h = \beta dx^5$	1.83 x 10^8	m^4/s
Topographic height	H_0	0 to 400	m
Forcing Factor	F_f	1.2 to 1.6	-

4.2 Numerical Methods

The model is implemented using a code written in FORTRAN 90. The main code was written by Nadeau (2011) and here we adapt it to our set-up. The system is initiated with random white noise. During the spin-up phase instabilities grow in the field and quasi-geostrophic jets are formed. Simulations are allowed to spin-up over a minimum period of 16 000 days, or longer where required to reach energy saturation. Time averaged statistics are then computed over a further 60 000 days.

4.2.1 Numerical Integration

The numerical integration of the governing equations is carried out using the Adams-Bashforth third-order numerical scheme (background on numerical methods may be found in several textbooks such as Gilat and Subramaniam (2011)). As applied to this problem, the Adams-Bashforth method is given in Equation 4.14.The initial three time steps are treated differently as the computation of $q^{(n+1)}$ uses values of q at the previous three time steps.

$$q^{n+1} = q^n + \frac{\Delta t}{12}\left[23\mathrm{RHS}^n - 16\mathrm{RHS}^{n-1} + 5\mathrm{RHS}^{n-2}\right] \tag{4.14}$$

where RHS refers to the value of the right-hand side of Equation 4.2 at the specified time steps. Jacobian operators are computed in the same manner as the original code, using the Arakawa scheme which permits the conservation of kinetic energy and enstrophy (Nadeau, 2011).

At each time step, the integration produces updated values of q in each layer. The direct back-computation of ψ_1 and ψ_2 from q_1 and q_2 is not straightforward due to the dependence of q in each layer on the stream functions in both layers. Thus the motions are projected onto the two vertical, baroclinic and barotropic, modes.

$$q_{BT} = \frac{H_1 q_1 + H_2 q_2}{H_1 + H_2} = \beta y + \nabla^2 \psi_{BT} \tag{4.15}$$

$$q_{BC} = \nabla^2 \psi_{BC} - \frac{f_0^2 H_T}{g' H_1 H_2} \psi_{BC} = \nabla^2 \psi_{BC} - \frac{1}{L_D^2} \psi_{BC} \tag{4.16}$$

where

$$\psi_{BT} = \frac{H_1}{H_T} \psi_1 + \frac{H_2}{H_T} \psi_2 \tag{4.17}$$

$$\psi_{BC} = \psi_2 - \psi_1 \tag{4.18}$$

The conversion results in two elliptic equations for q_{BT} to its stream-function, ψ_{BT}, and similarly for the baroclinic mode. The removal of the cross-dependence permits the elliptic inversion using the multigrid method (Briggs et al., 2000). The streamfunctions are then superimposed to give ψ_1 and ψ_2 at the next time step.

$$\psi_1 = \psi_{BT} - H_2/H_T\psi_{BT} \tag{4.19}$$

$$\psi_2 = \psi_{BT} + H_1/H_T\psi_{BT} \tag{4.20}$$

The algorithm then continues.

4.2.2 Computation of Mass Flux

The thickness fluxes are obtained by removing transport by the mean field from the total transport (see Section 3.1.2 for theory). We compute $\overline{\mathbf{u}'\eta'}$ as follows where the overbars indicate a temporal average.

$$\overline{\mathbf{u}'\eta'} = \overline{\mathbf{u}\eta} - \bar{\mathbf{u}}\bar{\eta} \tag{4.21}$$

and η is computed from the stream functions in the two layers.

$$\eta = \frac{f_0}{g'}(\psi_2 - \psi_1) \tag{4.22}$$

The first term on the right-hand side in Equation 4.21, $\overline{\mathbf{u}\eta}$ is simply the instantaneous values of the $\mathbf{u}$ and η fields multiplied together at each grid point and then averaged in time. The second term,$\bar{\mathbf{u}}\bar{\eta}$, computes first the time-averages of the separate variables and then multiplies them together. The subtraction of this mean transport term from the total transport leaves the transport due to mesoscale eddies, $\overline{\mathbf{u}'\eta'}$. Averaging computations occur every 100 time steps and are added to a running average. In addition to averaging mass fluxes we compute temporal averages of layer stream functions and interface gradients.

4.3 Summary

We carry out a series of simulations based on the two-layer QG model described in this section. The model is forced by a meridional density gradient and dissipated using bottom drag and hyperviscosity. We use a set of 25 simulations with varying combinations of topography and forcing strength throughout the core of our results in the following section; we summarize these simulations in Table 4–2. We carry out other simulations varying L_D and further varying F_f which we will introduce for varying motivations.

Table 4–2: Summary of combinations of topography and forcings in main simulations

Topography			F_f		
Flat	1.2	1.3	1.4	1.5	1.6
100 m ridge	1.2	1.3	1.4	1.5	1.6
200 m ridge	1.2	1.3	1.4	1.5	1.6
300 m ridge	1.2	1.3	1.4	1.5	1.6
400 m ridge	1.2	1.3	1.4	1.5	1.6

Chapter 5
Results and discussion

We carried out many simulations in total, 25 of which we present in our main results to assess meridional eddy diffusivities. The simulations vary the level of the imposed U_{shear} and use five different topographies; a flat bottom and ridges with heights of 100 m , 200 m, 300 m and 400 m.

This chapter is organized as follows. Section 5.1 decribes characteristics of the formation and form of quasi-geostrophic jets. We consider the spatial variation of mass transport in Section 5.2. Section 5.3 looks at the plausibility of an eddy diffusivity model by considering simple flow statistics. We use the results of this section to propose an eddy diffusvity model which we explore fitting both globally and locally in Section 5.4. These ideas are extended to look at the possible usefulness of a matrix diffusivity in Section 5.5. Finally, we note that our eddy diffusivity estimates are on the lower end of those found in the literature. Motivated by this we present the results of a further set of simulations with a larger Rossby radius in Section 5.6.

5.1 Formation of Quasi-steady Jets

5.1.1 Baroclinic Instability of the System

Flat Topography

Recall that the classic Phillips model for 2 layer baroclinic instability (refer Section 2.2.2) predicts the critical shear velocity to be βL_D^2. In our set-up we found the onset of instability growth occurred at values of U_{shear} less than βL_D^2. With flat bottom topography, we find this onset of instability growth, U_{onset}, to lie at approximately $0.7\beta L_D^2$.

A key difference between our model and that in the classically derived critical case is the presence of bottom drag. It is well understood that increasing bottom drag leads to more baroclinic flows (e.g. Rivière et al., 2004), but it is certainly not obvious how a term that removes energy from the flow could cause it to be more unstable. In our system, the bottom drag does not act on the imposed shear velocity in the two layers, U_1 and U_2, which are held fixed in the model. Nor does it remove energy from the upper layer. It only removes energy from the perturbation, or model response in the lower layer. The shear increases if more dissipation occurs in the barotropic mode. This therefore permits the flow to go unstable at lower levels of U_{shear} which is what we observe. The classic instability condition was able to be recovered by setting the bottom drag to zero. One could re-do the classic Phillips analysis including bottom drag to get an analytic expression for U_{onset}. This is beyond the scope of this project so we empirically find U_{onset}.

We remind the reader here that we chose to define the forcing factor, F_f, based on U^f_{onset}, where the superscript indicates the flat-bottomed case. For simplicity we present our results mainly in terms of F_f. An F_f of unity corresponds to a marginally stable case with flat bottom topography. The shear velocity is found therefore by $F_f U^f_{onset}$.

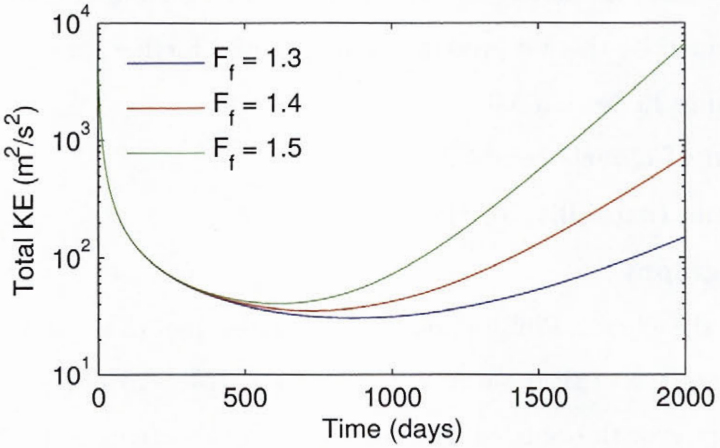

Figure 5–1: Sum of kinetic energy in the two layers during the spin-up phases of flat bottom simulations with different values of F_f; the graph shows the exponential growth phase.

The growth of the instability can be seen in the total kinetic energy of the system. The energy in the system at $t = 0$ is due to the white noise used to initiate the system (Section 4.2). This initial energy is predominantly in the small scales and is decays rapidly towards zero due energy removal by the hyper-viscosity term. After some time, instability growth is triggered and energy grows exponentially with a growth rate of α, where we find α to be proportional to $U_{shear} - U_{onset}$. An example of early energy growth is shown in log-scale in Figure 5–1 for a range of forcings. The slopes of the curves after approximately 1000 days in log-space are proportional to $U_{shear} - U_{onset}$, equivalently, it is proportional to $(F_f - 1)$.

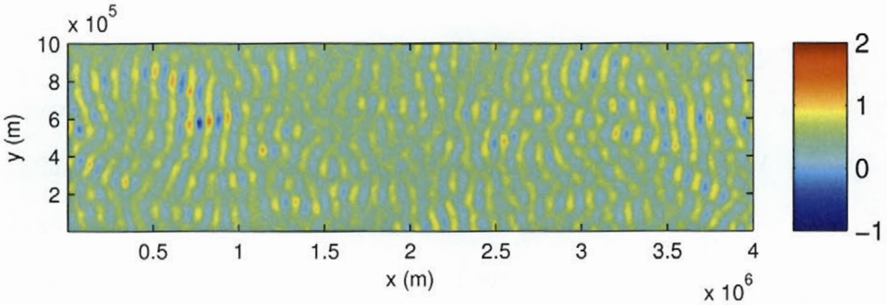

(a) t = 1500 days

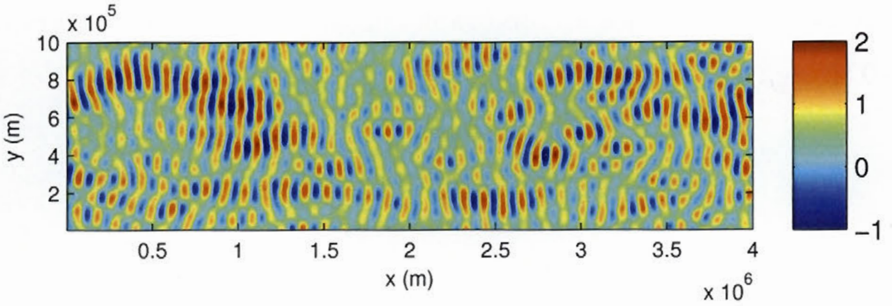

(b) t = 2000 days

Figure 5–2: The upper layer streamfunction, ψ_1, at two different time steps for simulation with flat bottom and F_f of 1.4. The time-steps are during the exponential energy growth phase when primarily one mode is growing.

During this exponential growth phase a regular structure is seen as one mode is predominantly growing. Figure 5–2 shows two ψ_1 fields during the exponential growth phase. It is possible to predict the maximum wavenumber at which there is baroclinic instability, k_{cutoff}, however the precise result depends on β. Here we make a rough approximation that $k_{cutoff} \sim 1/L_D$, and that the wavenumber of maximum growth, k_{max}, as smaller by an order one amount. If for example we take $k_{max} \sim 0.2k_{cutoff}$, then we find the wavelength of maximum growth is predicted to be approximately 100km, close to the predominant wavelength we observe in Figure 5–2.This exponential energy growth continues until the system kinetic energy peaks to a maximum value before falling back down to a lower equilibrium value. Simulations with lower levels of forcing take longer to reach this saturation level.

Ridge Topography

For the ridge cases we find the onset of instability to occur at even lower levels of forcing than U^f_{onset}. We show as an example the instability growth for a 200 m ridge in Figure 5–3 (analogous to Figure 5–1). We continue to denote the forcing factor as $F_f = U_{shear}/U^f_{onset}$ and note the system is unstable even when $F_f < 1$. We take the 200 m ridge here as example as it represents the middle of the topography height range but find the system unstable for $F_f < 1$ for all topography heights used. For the 200 m ridge we find $U_{onset} \sim 0.5U^f_{onset}$.

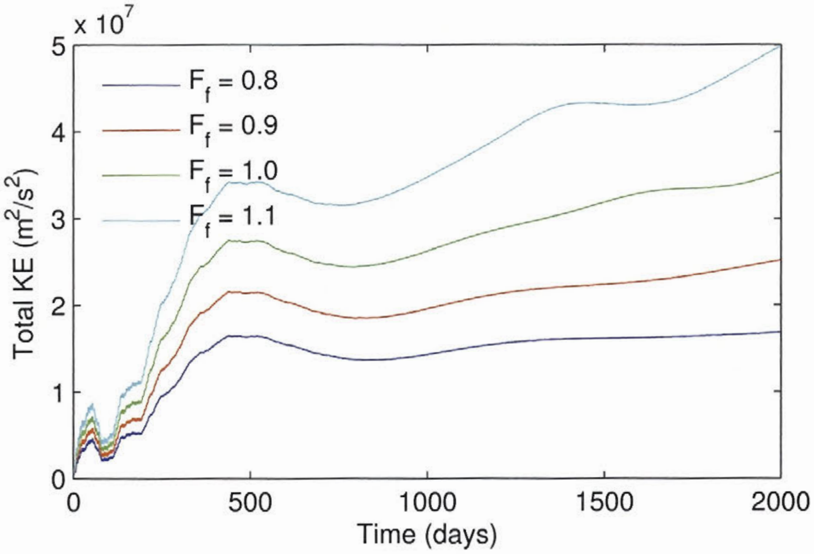

Figure 5–3: Sum of KE in the two layers during spin-up for simulations with 200 m high ridges and varying F_f, showing different growth mode of ridge simulations compared to flat bottoms.

Figure 5–3 shows almost no resemblance to the flat-bottom analogy in Figure 5–1. This suggests the early growth regime is not the same with and without topography. We show a series of instantaneous ψ_1 plots in Figure 5–4 during the spin-up phase for one of the simulations shown in Figure 5–3. A key difference is that the interaction between the imposed zonal mean flow and the ridge excites a large scale structure. As such, the initial energy growth is due to both the existence of the large scale topography waves and baroclinic instability. Additionally the baroclinic instability (wavenumbers comparable to $1/L_D$) occurs preferentially in parts of the domain where topography slopes favour instability.

To explain the initial structure observed in the earliest field in Figure 5–4, recall that U_2 is westwards in the lower layer. Where topography slopes downwards to the east, fluid columns are pushed upslope. Conversely when the topography slopes upward to the east, fluid columns are pushed downslope. This creates a ridge in the interface height at approximately $x = 1000$km and a trough in the interface at around $x = 3000$km. This occurs very early on and can be seen in the ψ_1 field in Figure 5–4 (a). The ridge-trough structure continues to evolve, both in conjunction with advection by the mean flow and with topographic Rossby wave propagation. By 200 days (Figure 5–4(b)) we find that the trough structure has moved into the southern half of the domain and the ridge into the northern part of the domain.

The growth of the baroclinic instability is finally observed in Figure 5–4(c), but only in some parts of the domain. In the ψ_1 field we see instability growth primarily to the east of the downward ridge slope at $x = 1000$km and to the west of the leading edge of the ridge at $x = 3000$km. Fields at earlier time-steps show instability first occurs on the southern tip of the ridge at $x = 1000$km. This baroclinic instability growth is masked in Figure 5–3 by the large energy contained in the large structure (compare the scales of Figure 5–1 and Figure 5–3).

Recall that for our ridge topography the meridional gradient of the bottom topography introduces a PV gradient in the bottom layer (see Section 4.1.2 for further details). The meridional slope acts as a stabilizing influence if it creates a PV gradient in the same direction as β or a destabilizing effect otherwise (Cushman-Roisin, 1994). To explain this consider Equation 5.1.

$$Q_{2y} = \beta - \frac{f_0}{H_2}\overline{\eta}^I + \frac{f_0}{H_2}\eta_{by} = \beta_{eff} + \frac{f_0}{H_2}\eta_{by} \tag{5.1}$$

Instability occurs when the meridional PV gradient reverses direction across the interface. Since Q_{1y} is always positive, instability occurs when Q_{2y} becomes negative. The orientation of topography slopes can either increase or reduce instability. On the northern flank of the ridge $\eta_{by} < 0$ acts to locally increase stability. On the southern flank, η_{by} works with the imposed interface gradient to reduce stability. In our case, $|\eta_{by}|$ can be locally very important especially for the higher topographies. At forcings much lower than U^f_{onset} the local topography gradient on the southern flank can cause Q_{2y} to be negative. Based

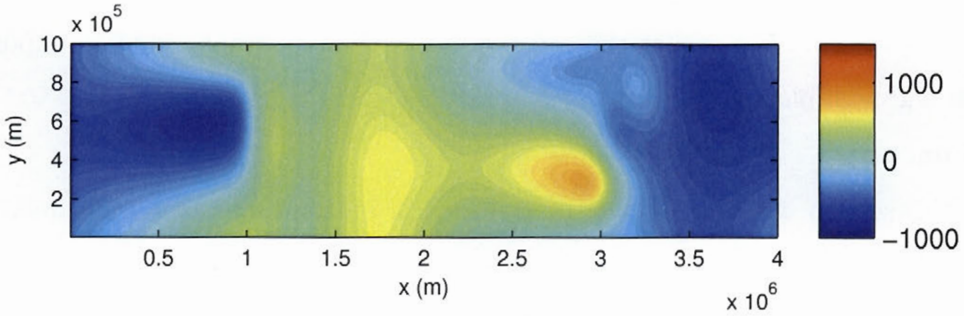

(a) $t = 20$ days

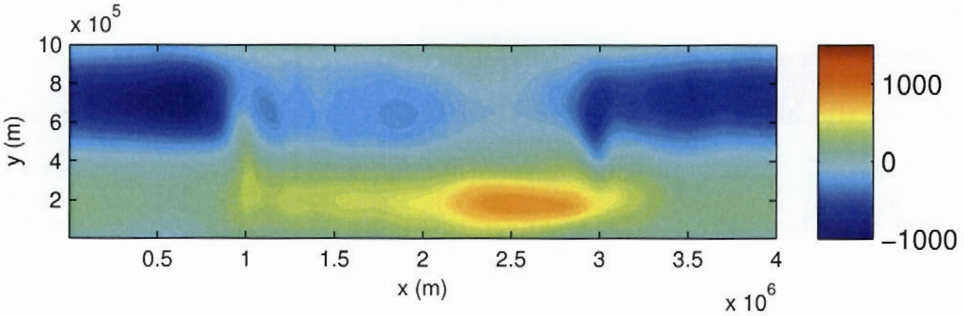

(b) $t = 200$ days

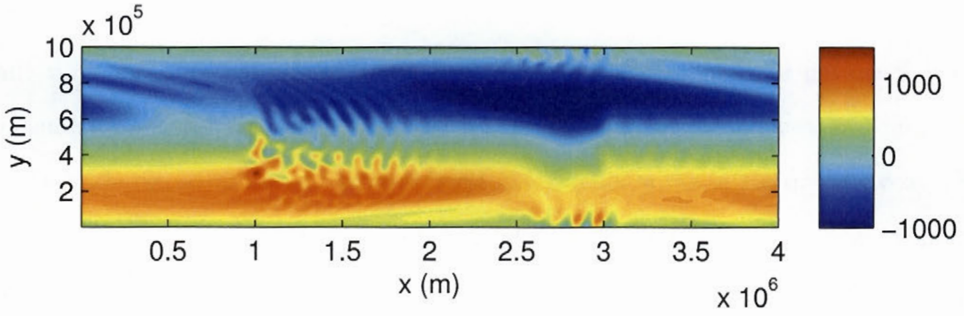

(c) $t = 2000$ days

Figure 5–4: ψ_1 for ridge of 200 m and F_f of 1.0 during spin-up. The development of the large-scale structure can be seen at all three time-steps and the start of baroclinic instability growth in panel (c).

on this we would expect the southern slopes to be the most baroclinically unstable. We could argue that this is loosely true as we see the first baroclinic instability initiated on the southern side of the ridge in the lee of the topography. However, what appears more obvious from Figure 5–4 is that the x derivative of the topography is more important in the initial growth phase.

Summary

In this section we showed that the inclusion of bottom drag caused our model to go unstable at lower shear velocities than expected. With our parameters U_{onset} for the flat-bottomed case is approximately 70% of the classic Phillips case. The addition of bottom topography led to a different growth regime and again reduced U_{onset}.

5.1.2 Jet Structure in Statistical Equilbrium

Following the initial growth period described in the preceeding section, the energy pertubation saturates and quasi-steady jets are formed in the domain. These jets are typical of β-plane turbulence. The energy saturation can be seen in the total KE in the system. Consider Figure 5–5 which shows the spin-up period over the first 15 000 days for simulations with a series of forcing and topography combinations. Plot (a) shows the energy growth for a range of topography heights at the same forcing. We observe the same exponential growth in the flat bottom case as we saw in Figure 5–1. We find the higher ridge simulations reach energy saturation the fastest, although all simulations with the same F_f grow towards the same saturation level energy. In plot (b) we show the spin-up energy for a range of forcing levels at the middle topography height. All five forcings show a similar growth regime. We see the total KE in the system at saturation increases with forcing. This makes sense as the energy in the system at equilibrium is given by the difference forcing and dissipation terms (see Section 4.1). Generally the spin-up period for each simulation was 15 000 days, although some simulations were run for longer as they had not saturated at 15 000 days (the flat bottom case in Figure 5–5 (a) for example). The simulations were then run for another 60 000 days to obtain time-averaged statistics.

At statistical equilibrium, the size and intensity of the jets are governed by bottom drag, strength of forcing and L_D. In these simulations bottom drag is fixed, however

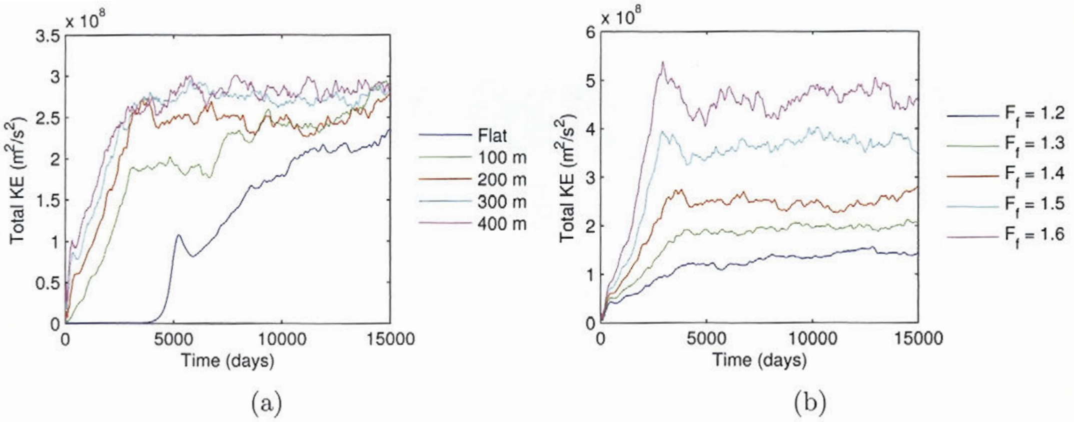

Figure 5–5: Sum of kinetic energy in the upper and lower layers during first 15 000 days of spin-up shown for a range of (a) topography heights at $F_f = 1.4$, and (b) forcing levels with the 200 m ridge. Note the y-scale difference between the two plots.

increasing the magnitude of r produces smaller jets. Here r is small enough that it permits the inverse cascade to grow to the Rhines scale. Further growth is constrained by the β effect and zonal flows are formed (Vallis, 2006).

Since we vary both forcing and topography, for consistency we show fields mainly for a reference case. The middle forcing and middle topographical height is used; a 200 m ridge with F_f of 1.4. We will focus on both the effect or forcing and the effect of topography height relative to this reference case. The effect of L_D is explored later in Section 5.6.

Instantaneous fields

Instantaneous upper and lower streamfunction fields are shown for the reference simulation in Figure 5–6. ψ_1 is predominantly decreasing with y indicating eastwards flows. Recall that u is equivalent to $-\psi_y$; regions of high gradient in the ψ_1 field therefore correspond to jet cores in the upper layer. The positions of the jets remain largely fixed between time intervals as bottom topography varies over scales much larger than the jet scale (Thompson and Sallée, 2010). In contrast, ψ_2 has an overall net increase across the

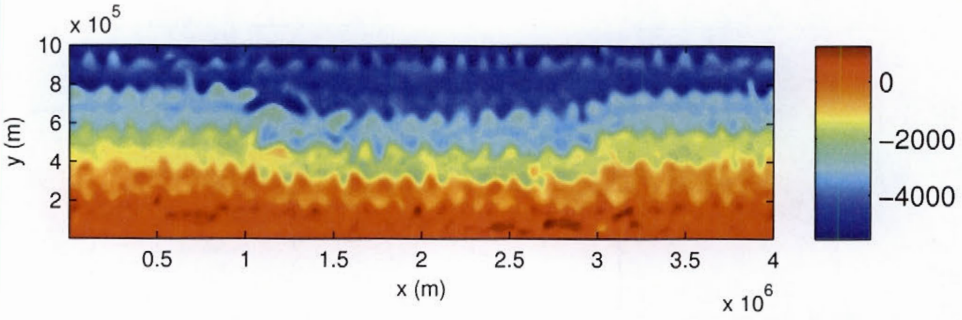

(a) ψ_1

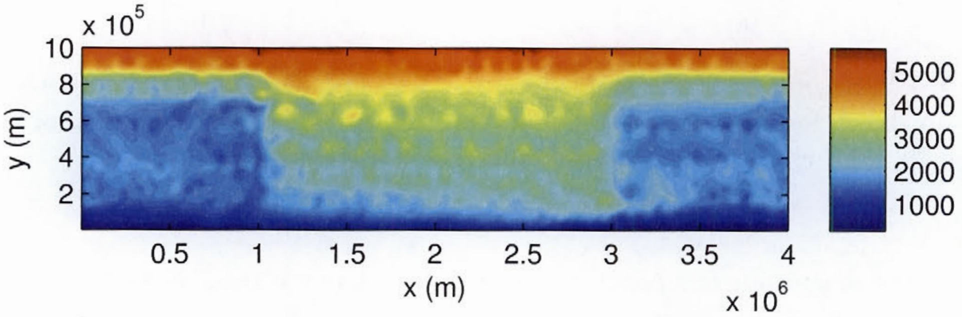

(b) ψ_2

Figure 5–6: Instantaneous ψ_1 and ψ_2 for our reference case, 200 m ridge and F_f of 1.4, at statistical equilibrium showing meridional excursion taken by the jets.

domain indicating a net westwards flow in this layer. Regions of recirculation are observed in the valley and, likewise, fluid parcels on the ridge crest do not move into the valley.

In the upper layer we see that the jets follow a meridional excursion to the south. In fact, in all ridge simulations we see an excursion in the lee of the topography. It can be explained simply by considering the conservation of PV for a one-layer system. Columns of water within the jet are vertically stretched as they move into deeper water off the ridge. To conserve PV, fluid parcels compensate by moving southward to increase the magnitude of their planetary vorticity. The jets shift northward moving back up onto the ridge for the opposite reasoning. The same idea can be extended to explain the observations in our

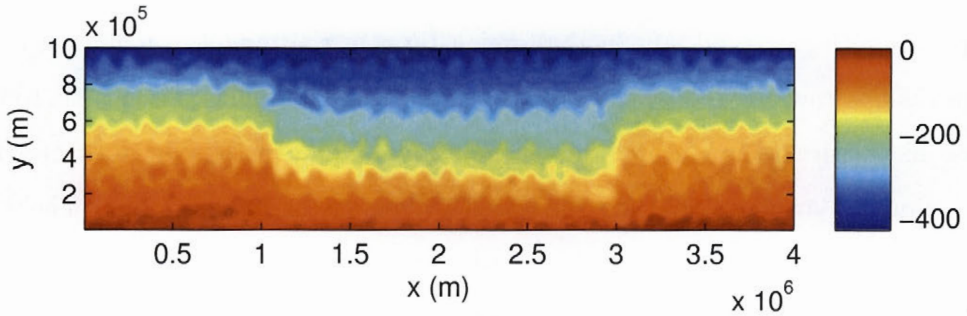

(a) η

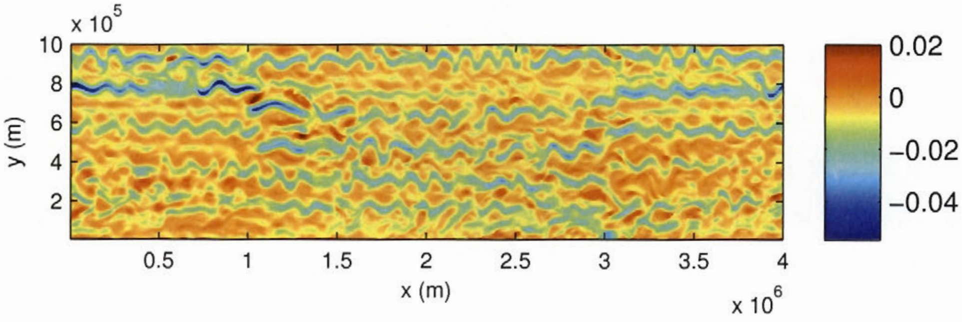

(b) η_y

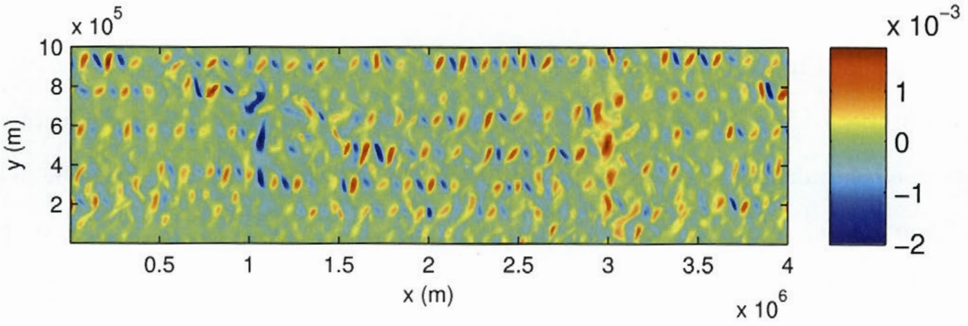

(c) η_x

Figure 5–7: Instantaneous η field and its derivatives for the reference case. Note the difference in scales between the η_x and η_y fields shown.

two-layer system. As expected, the absence of total fluid depth change in the flat bottomed topography means the jets remain zonal across the domain.

At the same timestep as in Figure 5–6, we show η and its derivatives in Figure 5–7. As η is proportional to $\psi_2 - \psi_1$, we see a meridional excursion of η-contours in the lee of the topography like ψ_1 and ψ_2. In the forcing term in the model, η is imposed as a net downward slope towards the equator (see Figure 2–4). The model response is to create a staircase like structure in the meridional direction. This can be seen most clearly in η_y where regions of steeper slopes are separated by regions of flatter slopes. These regions of step slope are closely related to the position of jet cores in the upper layer as seen in Figure 5–6 (a). Large negative values of η_x are seen at the end of the ridge at x = 1000 km and large positive values at the leading edge at x = 3000 km. These are coincident with the points where the jets take their meridional excursion.

For the reference simulation we show an instantaneous PV field of the upper layer in Figure 5–8(b). The PV is anti-correlated with η in Figure 5–7 as expected and we observe the same step-like structure. Bands of constant PV are separated by strong PV gradients indicating the jet cores. In the upper and lower panels we show how PV fields change with forcing. Figure 5–8(a) is the most weakly forced regime we use in these simulations and Figure 5–8(c) is the most strongly forced. As anticipated, we see that in Figure 5–8(c) the jets are larger and more turbulent compared to those in Figure 5–8(a).

The number of jets in the domain does not vary significantly in our simulations. In the flat bottomed simulations between five and six jets are formed in the domain, depending on the forcing level. This corresponds to a jet spacing of 160 to 200 km. We compute the Rhines scale as $L_{Rhines} \sim (U/\beta)^{1/2}$ and find it to vary with forcing level from approximately 20 to 30 km. Note that Thompson and Sallée (2010) define L_{Rhines} with an additional scaling factor of 2π. They interpret this L_{Rhines} to be a measure of the meridional eddy mixing within a single jet. Using this scaling factor, L_{Rhines} for our simulations is very close to the jet spacing.

Time-averaged Fields

After statistical equilibrium was reached we run all simulations for an additional 60 000 days. We will be interested in relating the time-averaged fields to eddy statistics. To

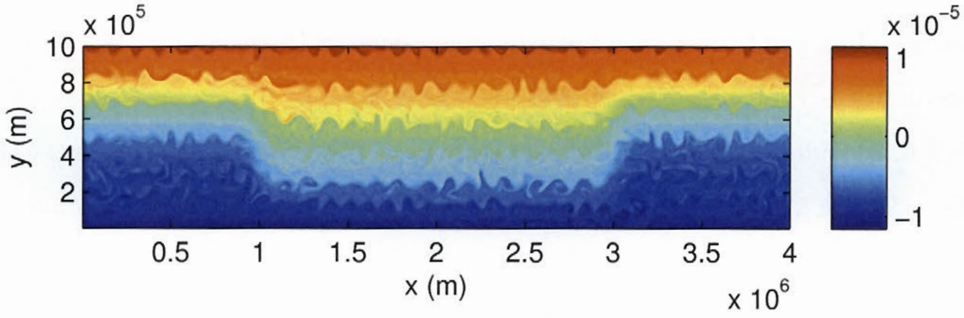

(a) $F_f = 1.2$

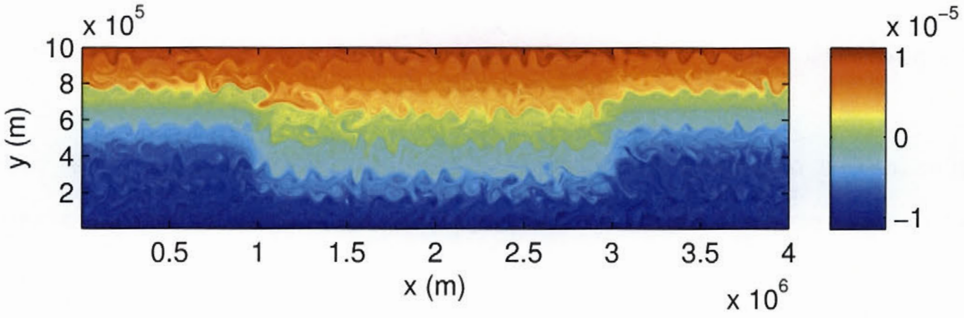

(b) $F_f = 1.4$

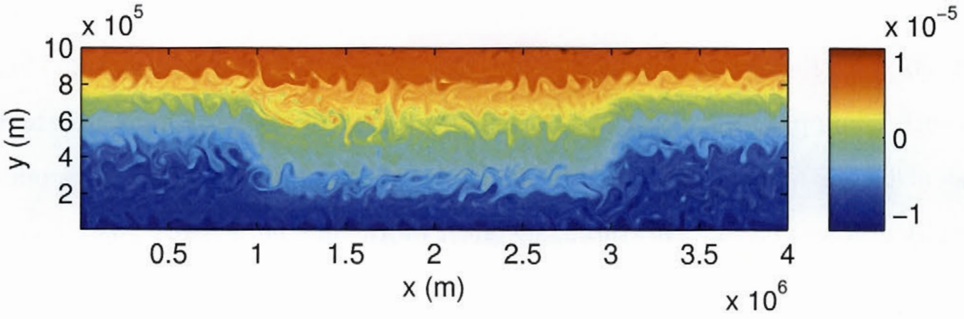

(c) $F_f = 1.6$

Figure 5–8: Upper layer instantaneous PV fields for simulations with a 200 m high ridge. Fields for three different forcings are shown; (a)$F_f = 1.2$, (b)$F_f = 1.4$ and (c) $F_f = 1.6$. The effect of the forcing strength can be seen in the size of the jets and eddies.

this end, it is useful to first examine the time-averaged flow. In the flat bottom simulations, a series of quasi-steady zonal jets are formed. In our ridge simulations the jet structures are a little more complex. We choose this averaging time to be long compared to the time-scale of the eddies. Later in Section 5.2.2 we will come back to the averaging time and see that the structure does evolve somewhat with averaging time.

We now consider the effect of both topography height and forcing level on the structure of the jets. Figure 5–9 shows a series of ten $\overline{u_1}$ fields for a combination of forcing strengths and topographical heights. To the left we show all five topographies at the reference forcing of $F_f = 1.4$. To the right we show our reference case topography (a 200 m ridge) at all five levels of forcing used in this project. In the upper layers shown, jet cores are identified by peak eastwards velocities alternating with regions of either weaker eastwards or westwards flows.

Focusing first on the effect of forcing (right-hand panels in Figure 5–9), we see the stronger forcings produce larger, more widely spaced jets. This is consistent with observations of the PV fields in Figure 5–8. We note that the jets in the domain are not of equal strength. Even following the same jet, the core velocity changes notably when the jet moves off the ridge and again when it moves back up onto the ridge. In our simulations we find jets have highest core velocities on the northern flanks of the ridge. This is consistent with Thompson and Sallée (2012) who saw stronger jets on their southern flanks (equivalent to our northern flanks). This is somewhat counter-intuitive since our bottom topography gradient has a local stabilizing effect on the northern flanks (see Section 5.1.1). The reason is evident in the mean interface gradient fields presented later in Section 5.2.1. We will show that on the northern ridge $\overline{\eta_y}$ is steeper. This means baroclinic eddies are relaxing the isopycnals towards a locally steeper critical gradient. This in turn is able to supply more potential energy to the mean flow and results in stronger jets. Alternatively, since topography is stabilizing on the northern flank of the ridge, a larger η_y is needed for instability.

Now focusing on the effect of topography (shown in the fields on the left in Figure 5–9) we see that a meridional excursion is observed in all ridge simulations. Recall the one-layer analogy we gave in Section 5.1.2 as a simple explanation. Based on this, we would

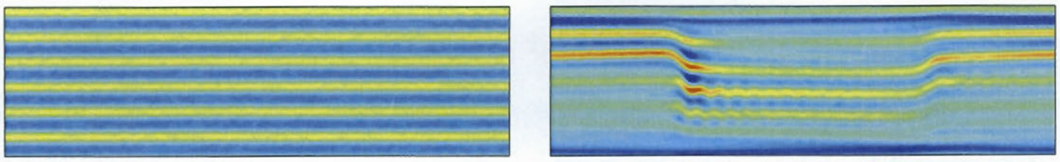

(a) Flat, $F_f = 1.4$ (b) 200 m ridge, $F_f = 1.2$

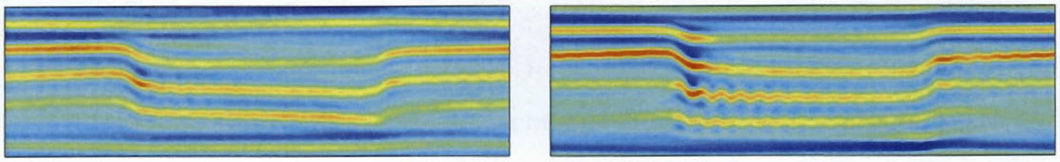

(c) 100 m ridge, $F_f = 1.4$ (d) 200 m ridge, $F_f = 1.3$

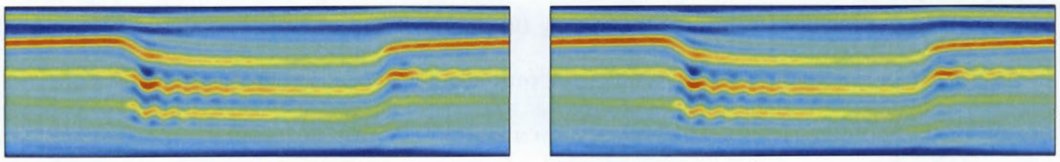

(e) 200 m ridge, $F_f = 1.4$ (f) 200 m ridge, $F_f = 1.4$

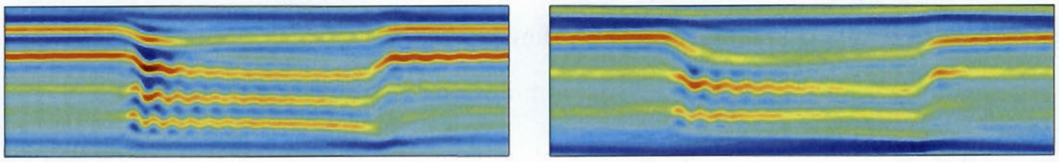

(g) 300 m ridge, $F_f = 1.4$ (h) 200 m ridge, $F_f = 1.5$

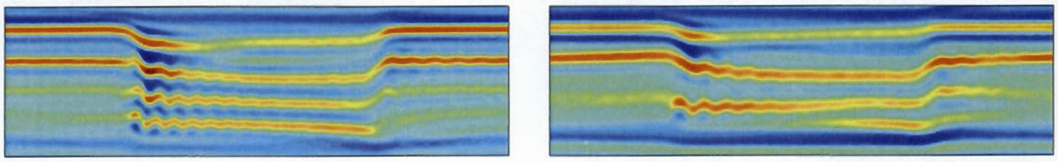

(i) 400 m ridge, $F_f = 1.4$ (j) 200 m ridge, $F_f = 1.6$

Figure 5–9: Time-averaged upper layer velocity fields, showing the effect of topography and forcing strength on the the time-mean jet structure. On the left we vary topography height relative to the reference case. On the right the forcing strength is varied. The same colour scale as in Figure 5–10 is used.

expect that a larger depth change requires a larger change in total vorticity. As the ridge height increases this could be achieved by shifting larger distances southward in a one-layer scenario. We do not find this to be the case in our two-layer system in the upper layer. In fact little variation is seen in the meridional excursion of the jets across simulations with different topography heights. In the higher topography simulations, a standing eddy is excited as the jet moves off the ridge. These eddies serve to remove energy from the flow (Wolff et al., 1991) and decay within roughly 5 wavelengths in our simulations. The same is seen, although to a lesser extent, at the leading edge of the ridge at $3L_x/4$. Information is not transmitted upstream of the change at either location.

In the lower layer the dynamics are much different. Figure 5–10 shows the time-averaged lower layer stream function and velocity field for the reference case. Figure 5–10(a) is the time-averaged analogy to the ψ_2 field presented earlier in Figure 5–6 (b). Both fields in Figure 5–10 show closed recirculations zones on the crest of the ridge and in the valley. This is seen in (a) by the streamlines which do not track the entire zonal length of the domain. In (b) the recirculation is seen by regions of eastwards velocity alternating with regions of westward velocity in the valley between the ridge.

In the lower layer of the flat bottom simulations we find largely westwards flows. Directly under jets in the upper layer, westward velocities are roughly two orders of magnitude smaller than those in the upper layer. These regions are separated by wider and stronger eastward return flows.

Summary

In all of our simulations quasi-steady jets are formed. As expected, we find the the size and strength of the jets at statistical equilibrium to vary with the strength of forcing. The addition of bottom topography caused the jets to take a meridional excursion to the south in the lee of the topography and return northward at the leading edge. Also noteworthy with the topography cases is that the jets in the domain do not have equal strengths. Even along the same jet the same core velocity is not maintained and varies with bottom topography. We will come back to this several times later, particularly when we consider locally defined eddy diffusivities in Section 5.4.2.

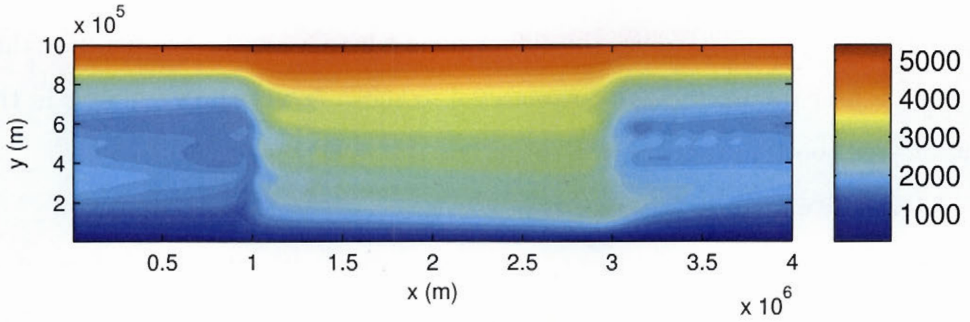

(a) $\overline{\psi_2}$

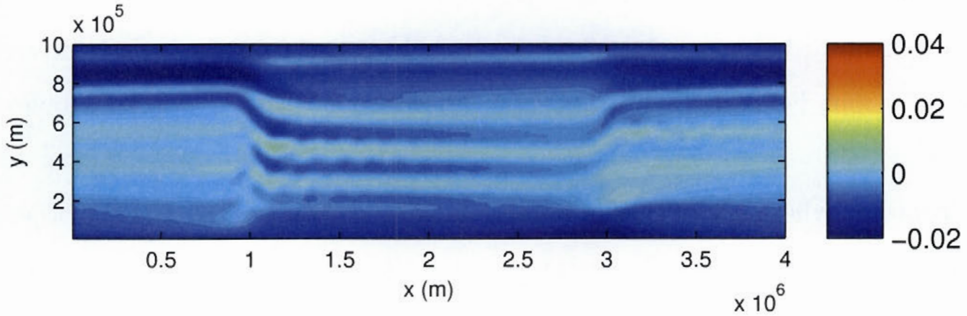

(b) $\overline{u_2}$

Figure 5–10: Time averaged $\overline{\psi_1}$ and $\overline{u_2}$ showing zones of recirculation in the lower layer in the valley. Simulation has a ridge height of 200 m and F_f of 1.4.

We find the jets to be far more evident in the upper layer than the lower layer. This fact confirms that our set-up produces quasi-realistic dynamics in agreement with the fact that ACC jets are strongest closest to the surface. It also leads us to believe that an understanding of the mixing of jets in the Southern Ocean will be most meaningful if derived from the upper layer dynamics. We decide to focus our analysis in the upper layer and drop the 1 subscripts (unless required) from here on.

5.2 Spatial distribution of mean mass transport and interface gradients

We remind the reader that the GM90 thickness diffusivity suggests that $\overline{\mathbf{u}'\eta'} \sim \kappa\nabla\overline{\eta}$. In this section we discuss qualitatively $\overline{\mathbf{u}'\eta'}$ and $\nabla\overline{\eta}$ fields from our simulations. We will not consider quantitatively whether this model can be applied to our data until Section 5.3. Again, we present and explain fields mainly in terms of reference cases using the middle forcing strength; $F_f = 1.4$. We use the 400 m ridge where we wish to accentuate the effects of the ridge. Later we use the flat bottom case to show small scale variations in the fields in isolation from bottom topography effects.

5.2.1 Mean interface gradient

We show mean interface gradients for a simulation with a ridge of 400m at the reference forcing strength in Figure 5–11. These are the time averaged-equivalent of those in Figure 5–7, although note that the topography height is not the same. The $\overline{\eta}$ interface has a net downward slope towards the equator clearly seen in the y-derivative. Like in the instantaneous fields in Figure 5–7, the interface has a staircase like profile; regions of steeper slope alternate with regions of flatter slopes. The jet cores lie close to locally steep η-contours where the supply of potential energy is maximum. A series of jet cores is therefore seen in Figure 5–11(a) identified by locally high $\overline{\eta_y}$ (η steep) values. These core alternate with lower values of $\overline{\eta_y}$ (flatter η) corresponding to backflow regions between the jets. The same meridional deflection of the jets is observed in the lee of the topography. We also find domain-maximum values of $\overline{\eta_y}$ are found on the northern flanks of the ridge - coincident with maximum $\overline{u_1}$.

We find that $\overline{\eta_x}$ is only large in magnitude where the mean velocity has a meridional component. This occurs on the downslope and upslope of the ridge at approximately $x = 1000$km and $x = 3000$km respectively. We also observe some structure in the lee of the topography that decays over several wavelengths. This corresponds to the eddy excited at the end of the ridge identified in Figure 5–9 (note it can also be seen in the $\overline{\eta_y}$ field). Although difficult to see from the scale of the plot, $\overline{\eta_x}$ also has some small scale variation in the zonal direction like in the instantaneous field in Figure 5–7.

The effects of the ridge on $\nabla\overline{\eta}$ are most apparent in this highest topography case and less so for the lower ridges. Overall the observations of $\nabla\overline{\eta}$ are very similar to those observed in the $\overline{u_1}$ fields in Figure 5–9. We can therefore say the appearance of this term in the GM90 eddy diffusivity model gives a representation of the jet structures.

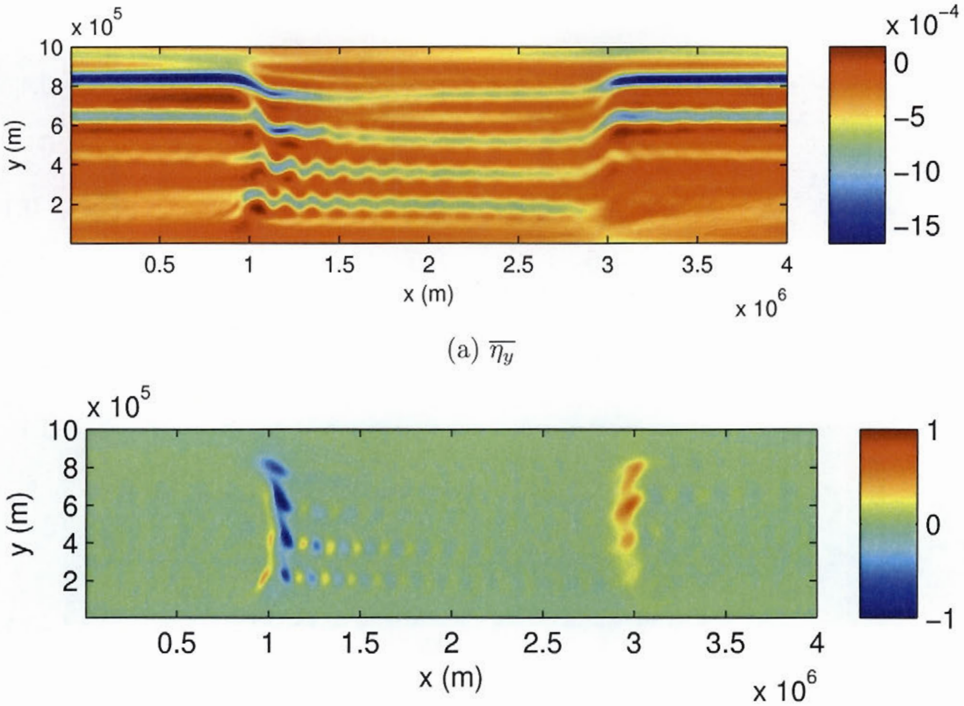

(a) $\overline{\eta_y}$

(b) $\overline{\eta_x}$

Figure 5–11: Mean interface gradients for simulation with a ridge of 400m and forcing factor of 1.4. Jet cores are indicated by steep $\overline{\eta_y}$ gradients. Note the two different scales in the plots.

5.2.2 Mass Fluxes

We now consider time-averaged meridional and zonal mass fluxes in Figure 5–12. For consistency, the fields are from the simulation with the same parameters as that in Figure 5–11. In Figure 5–12 (a), $\overline{u'\eta'}$ is positive on the northern side of the jet core and negative on the southern side. This means η' is transported eastwards on the northern side and westwards on the southern side of the jet core. In the meridional profile, this eastwards transport of η' is maximum where the shear in the mean flow is at a negative maximum value. Likewise, the westwards transport of η' is maximum where the shear in the mean

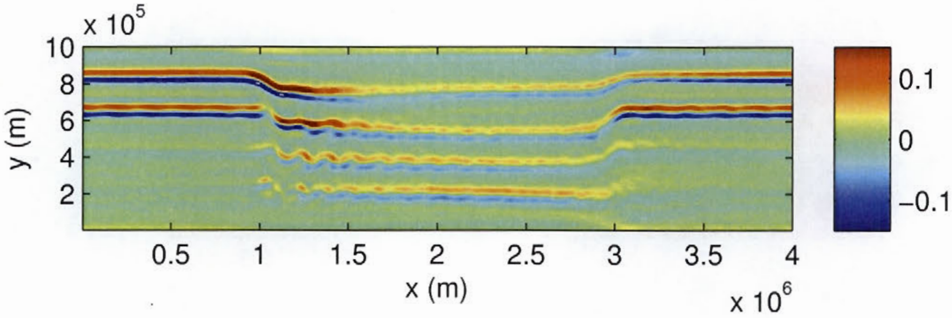

(a) $\overline{u'\eta'}$

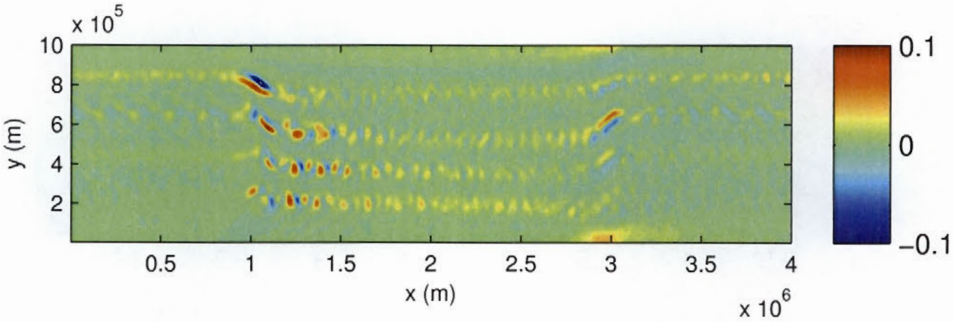

(b) $\overline{v'\eta'}$

Figure 5–12: Time averaged fluxes, $\overline{u'\eta'}$ and $\overline{v'\eta'}$, from a simulation with F_f of 1.4 and a topographical height of 400m.

flow is a positive maximum. $|\overline{u'\eta'}|$ is highest on the northern flanks of the ridge. This is where the highest jet core velocities are observed (review Figure 5–9).

Obviously, the net flux across any zonally reconnecting contour must be constant at equilibrium. If there were a net flux in the cores but not between, then mass would pile up between the jets. Recall that the derivations of the QG model equations assume a non-divergence of the velocity field to leading order (see Section 2.1.1). In fact, there is a smaller non-divergent correction the velocity, which scales as ϵ. It is this order ϵ correction to the velocity which makes up the difference. Although it could be calculated, it is beyond the scope of this work.

In Figure 5–12 (b) $\overline{v'\eta'} > 0$ in the upper layer. Within the domain, higher $\overline{v'\eta'}$ fluxes occur in the lee of the topography, in agreement with Thompson and Sallée (2012). Locally maximum flux occurs in the jet cores. Comparing with Figure 5–11 (b) we find these regions of high $\overline{v'\eta'}$ flux are coincident with regions of steep $\overline{\eta_y}$. The increased transport in regions of steeper isopycnals appear to support the GM90 thickness diffusivity hypothesis. In the backflow regions $\overline{v'\eta'}$ drops to a minimum, often close to zero. Even more fundamentally, we note that positive $\overline{v'\eta'}$ flux results from negative $\overline{\eta_y}$, supporting a downgradient hypothesis.

We compare the magnitudes of $\overline{u'\eta'}$ and $\overline{v'\eta'}$. For the fields in Figure 5–12 we compute the root-mean square of the mass fluxes. We find $\overline{u'\eta'}_{rms}$ is 3.52 x 10^{-2} m^2/s and $\overline{v'\eta'}_{rms}$ is 1.13 x $10^{-2}\mathrm{m}^2$/s. In general modellers are more concerned with modelling $\overline{v'\eta'}$ but we find $\overline{u'\eta'}$ fluxes to be of larger magnitude. In the upper layer, the effective transport velocity (Bolus velocity) due to mesoscale eddies in the zonal direction is $\overline{u'\eta'}/H_1$. The superposition of this on the mean zonal flow, $\overline{u}$ gives the effective zonal transport velocity. Transport by mesoscale eddies in the zonal direction is only significant in modelling terms if its magnitude is comparable with the mean flow velocity. We find that $\overline{u'\eta'}/H_1$ is $\pm 0.5\%$ of $\overline{u_1}$ in all runs; that is the zonal transport of mass attributed to the eddies is less than 0.5% of that of the mean flow. In the meridional direction, $\overline{v}$ is often very close to zero. This means the only transport in the meridional direction is attributed to these $\overline{v'\eta'}$ fluxes.

Zonal distribution of Mass Fluxes

We discuss zonal distribution of mass transport here. We also use it to demonstrate the influence of the choice of averaging time as noted in Section 5.1.2. We will consider the meridional distribution of mass fluxes shortly in Section 5.3.2 where we use it to quantitatively test a locally defined eddy diffusivity.

For sufficiently long averaging times, one expects $\overline{u'\eta'}$ and $\overline{v'\eta'}$ to be functions of y alone. In fact, in the flat bottom simulations there is no reason that the jets should remain physically locked in latitude. In other words, for a very long averaging time, $\overline{u'\eta'}$ and $\overline{v'\eta'}$ should converge to a single value everywhere in the domain. It is well known, however, that quasi-zonal jets can be remarkably steady. We want to choose an intermediate averaging time that captures the spatial distribution of mass transport as it relates to the mean jet structure. At the same time we want to average sufficiently long to remove small scale variations due to transient eddies.

From Figure 5–12 we can see that $\overline{v'\eta'}$ varies in the x direction along the jet cores. In fact we find these small scale variations in the x direction in $\overline{v'\eta'}$ occur in all simulations with our averaging time of 60 000 days. We want to evaluate the significance of these fluctuations and their dependence on the averaging time used. For simplicity we take the flat bottom simulation at the reference forcing ($F_f = 1.4$) for a series of averaging times. We take zonal slices aligned with jet cores from the $\overline{v'\eta}$ field and evaluate the standard deviation of fluctuations about the mean along the jet core.

Figure 5–13 shows a cross-section of $\overline{v'\eta'}$ through a portion of the same jet core for three different averaging times used. We do see the size of the fluctuations reduce with increasing averaging time although they are slow to do so. This can be seen in both the raw data in (a) and the standard deviation of the fluctuations in (b). For 60 000 days, the averaging time used in these simulations, the fluctuations have a standard deviation of $0.0055 \pm 0.0006 \mathrm{m}^2/\mathrm{s}$ (equivalent 36 % of the mean value). We could expect that after a very long averaging time the fluctuations would eventually diminish to zero.

Fluctuations in the $\overline{u'\eta'}$ along the jet core are similar in magnitude; for the same simulation in Figure 5–13 core values have a standard deviation of $0.0050 \mathrm{~m}^2/\mathrm{s}$. In regions of maximum and minimum $\overline{u'\eta'}$ flux on either side of the jet core fluctuations are slightly smaller but of a similar amplitude. These small scale variations are only evident in $\overline{v'\eta'}$, $\overline{u'\eta'}$ and $\overline{\eta_x}$ fields. Fortunately, we don't find spatial averages to depend on the averaging time used. This means estimating eddy diffusivities is more-or-less independent of averaging time. However, one could possibly expect that locally defined eddy diffusivities would vary with the averaging time. Other fields, such as $\overline{\eta_y}$ and ψ, fields do not display such long residing zonal variations.

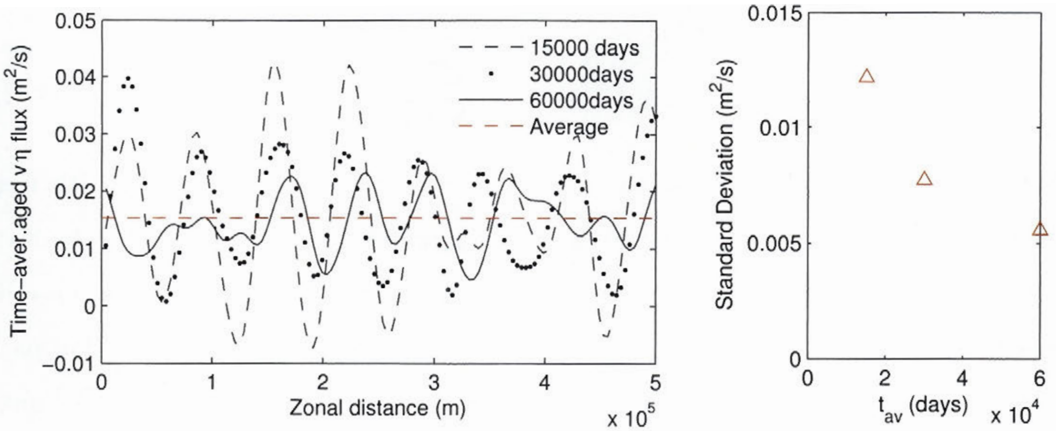

(a) $\overline{v'\eta'}$ cross-section

(b) σ of $\overline{v'\eta'}$

Figure 5–13: (a) Zonal cross-section of $\overline{v'\eta'}$ through most northern jet core for three different averaging times, t_{av}. (b) Corresponding standard deviation of fluctuations as function t_{av}. Simulation is for a flat bottom and F_f of 1.4. Note that for clarity only a portion of the domain length is plotted.

Cross-jet Fluxes

In the flat bottomed simulations $\overline{\psi_1}$ and η contours are aligned. The jets are zonal and $\overline{v'\eta'}$ gives the mass flux across the jets. In contrast, in the ridge simulations $\nabla\eta \sim \nabla\overline{\psi_2} - \nabla\overline{\psi_1}$. This means streamlines in the upper layer are not necessarily aligned with η contours. This can be seen by comparing ψ_1 in Figure 5–6 to η in Figure 5–7.

We are interested in how mass is fluxed across the jet cores. In the ridge simulations, $\overline{u_1}$ has a meridional component in some regions of the domain - particularly often in the lee of the topography (see Figure 5–9). In these regions the cross-jet direction has a zonal component. This means $\overline{v'\eta'}$, which is typically of most concern to modellers, may not completely explain the cross-jet transport. We seek to evaluate how much of the cross-jet transport in the ridge simulations can be attributed to the zonal fluxes, $\overline{u'\eta'}$. As jet cores follow streamlines (Thompson and Sallée, 2012), the local cross-jet transport is given by the dot product between the the mass flux vector and a unit vector locally normal to the flow direction, $\hat{n}$. The cross-jet transport is given by $\overline{\mathbf{u}'\eta'} \cdot \hat{\mathbf{n}}$ where

$$\hat{\mathbf{n}} = \frac{\overline{\psi_{1x}}}{|\nabla\overline{\psi_1}|}\hat{i} + \frac{\overline{\psi_{1y}}}{|\nabla\overline{\psi_1}|}\hat{j} \tag{5.2}$$

The fraction $\overline{u'\eta'}$ contributes to cross-jet transport, $\overline{\mathbf{u}'\eta'} \cdot \hat{\mathbf{n}}$, increases with forcing strength and topography height. It peaks to maximum of 4.6% with a 400 m high ridge and forcing factor of 1.6. The increase in percentage with topography makes sense if we review Figure 5–9. For the higher topography runs, the oscillation of the mean flow path in the lee of the topography means more opportunity for mass fluxes to cross as $\overline{u'\eta'}$ fluxes.

Summary

Recalling that the GM90 thickness diffusivity model predicts $\overline{\mathbf{u}'\eta'}$ from $\nabla\eta$ fields, we introduced fields of these variables in this section. We have not considered them in great detail but will continue to refer back the structures of the mass flux and interface gradient fields to explain results we find in fitting eddy diffusivities. Qualitatively, we find that maximum $\overline{v'\eta'}$ transport occurs in the jet cores where $\overline{\eta_y}$ is steepest. $\overline{u'\eta'}$ advects upper layer mass eastwards in negative mean shear in the jet and westwards in positive mean shear. The majority of cross-jet transport does occur as $\overline{v'\eta'}$ transport although we continue to include $\overline{u'\eta'}$ for completeness.

5.3 Plausibility of an eddy diffusivity model

Recall the classic eddy diffusion parameterization where $\overline{\mathbf{u}'\eta'} \sim -\kappa\nabla\eta$. κ could be thought of as a scalar or as a tensor. In its simplest scalar form, the hypothesis predicts that $\overline{v'\eta'} \sim -\kappa\overline{\eta_y}$. Globally this means that we should see a linear relationship between globally averaged $\overline{v'\eta'}$ fluxes and the imposed interface gradient $\langle\overline{\eta_y}\rangle$. Recall that $\langle\overline{\eta_y}\rangle$ is related to U_{shear}, and therefore we could also express mass fluxes in terms of the shear velocity. We consider whether the GM90 model is applicable to our results in Section 5.3.1. Likewise, in the zonal direction a simple scalar eddy diffusivity model predicts $\overline{u'\eta'} \sim -\kappa\overline{\eta_x}$. On a global scale we note that $\langle\overline{\eta_x}\rangle = 0$. This traditional scalar hypothesis then predicts that $\langle\overline{u'\eta'}\rangle$ is also equal to zero. We test whether this is true in Section 5.3.1. We consider whether it makes sense to define κ in all flow regions in Section 5.3.2.

5.3.1 Global mass flux

Global meridional flux

If an eddy diffusivity approach makes sense, then we should see a linear relationship between $\langle\overline{\eta_y}\rangle$ and $\langle\overline{v'\eta'}\rangle$. Figure 5–14 shows that increasing forcing does lead to higher net meridional mass fluxes for all topographies. Over a range of values a well defined slope is evident, except at lower values where the data points tail off. The relationship is clear for the flat bottom but a little less so for the ridge topographies. Overall, these results support the case for a scalar downward gradient eddy diffusivity hypothesis.

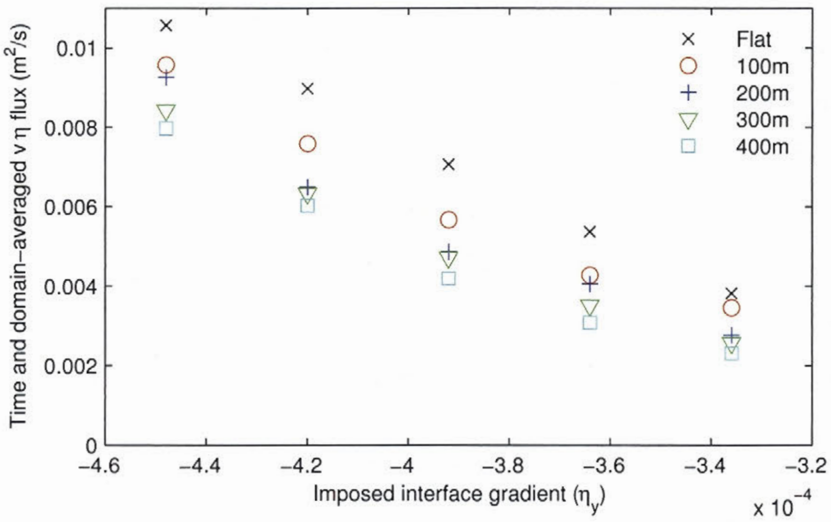

Figure 5–14: Interface gradient imposed by forcing, $\langle\overline{\eta_y}\rangle$, versus domain and time averaged meridional flux, $\langle\overline{v'\eta'}\rangle$. Data is shown for all simulations and highlights an apparent zero flux for a non-zero $\langle\overline{\eta_y}\rangle$.

Note however that the data points do not pass through $\bar{\eta_y} = 0$. We denote the intersect value as η_y^{crit}. Furthermore, this leads us to believe that an eddy diffusivity model should more appropriately be fitted against $[\bar{\eta}_y - \bar{\eta}_y{}^{crit}]$. An eddy diffusivity hypothesis would then take the form in Equation 5.3, where κ_0 is a normal scalar eddy diffusivity.

Recall that the GM90 thickness diffusivity is based on an idea that baroclinic eddies are generated to relax isopycnals (See Section 3.1). Increased mixing is predicted where isopycnals are steep and can supply large amounts of potential energy. If we consider that baroclinic eddies will only relax isopycnals so that they are baroclinically stable, rather than flat, then alternatively it makes sense to use some sort of measure of the difference between these two slopes. This is how $\bar{\eta}_y - \bar{\eta}_y{}^{crit}$ can be interpreted physically.

$$\overline{v'\eta'} = \kappa_0[\bar{\eta}_y - \bar{\eta}_y{}^{crit}] \tag{5.3}$$

We estimate η_y^{crit} from Figure 5–14 for each topography. Since the higher forcings show a stronger linear relationship we choose to estimate regressions using the four highest forcings. Extrapolating to $\langle\overline{v'\eta'}\rangle = 0$ obtains an estimate of the critical interface gradient. η_y^{crit} does not vary significantly; between -2.81 x 10^{-4} for the flat bottom to -3.19 x 10^{-4} for the 400 m ridge. For the flat case, η_y^{crit} is very close to our empirically derived interface gradient of -2.80 x 10^{-4} corresponding to U_{onset} in Section 5.1.1.

$\overline{\eta_y}^{crit}$ becomes steeper with increasing topography height. This is contrary to Section 5.1.1 where topography was seen to trigger instabilities at lower forcings than in the flat case. Thus for the ridge cases η_y^{crit} is not equivalent to the forcing level at which we see the onset of eddy generation, U_{onset}. It should be considered as more of an effective critical value for the problem which lends itself to the $[\overline{\eta_y} - \eta_y^{crit}]$ refinement. Note also in passing that interface slopes can locally be flatter than η_y^{crit}. This problem is addressed in due course in Section 5.4.

Figure 5–15 is a plot analogous to Figure 5–14 but now plotted with the critical interface gradient subtracted. The curves for the five different topographies collapse onto

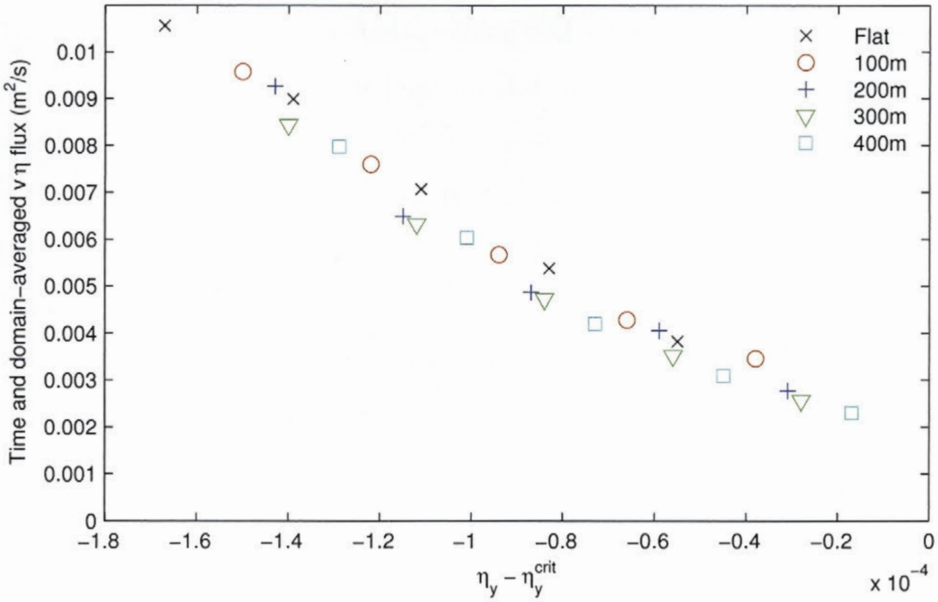

Figure 5–15: Time averaged meridional flux, $\langle\overline{v'\eta'}\rangle$, versus $\langle\overline{\eta_y}\rangle - \eta_y^{crit}$, showing validity of fitting an eddy diffusivity model against $\langle\overline{\eta_y}\rangle - \eta_y^{crit}$.

each other. The data points now pass much closer to zero. However, as η_y^{crit} was estimated using data points from higher forcings, a linear regression through the more weakly forced regimes does not appear to pass through the origin.

One may have been tempted to estimate κ from a linear regression in Figure 5–14, however Figure 5–15 makes a non-linearity in the data more obvious. κ_0 appears to be lower at lower forcing as given by the flatter slopes and higher at higher forcings. We could estimate κ_0 from slopes locally or globally in Figure 5–15 but choose not to. Generally, Figure 5–15 supports a scalar eddy diffusivity model as per Equation 5.3. The difference being that κ_0 does not appear to be a constant but proportional to $\overline{\eta_y}$.

Global zonal mass flux

As already mentioned, $\langle\overline{\eta_x}\rangle$ is identically zero. In these simulations it is always at least eight orders of magnitude than its average magnitude, $\langle|\overline{\eta_x}|\rangle$. The traditional scalar downward gradient eddy diffusivity then predicts that $\langle\overline{u'\eta'}\rangle$ should also be zero. Figure 5–16 verifies $\langle\overline{u'\eta'}\rangle = 0$ to hold approximately for the flat runs and ridges of 100m ridge. This means that regions of eastwards advection of $\overline{u'\eta'}$ are approximately balanced by a counter westwards advection (refer to Figure 5–12). However simulations with larger topography and higher forcings produce a net westward flux. To put this in perspective, for the 400 m ridge topography and a forcing factor of 1.6, $\langle\overline{u'\eta'}\rangle$ is 7.4% of $\langle|\overline{u'\eta'}|\rangle$. Some of this could be explained as cross-jet transport occurring as $\overline{u'\eta'}$ fluxes. However as we saw earlier in Section 5.2.2 the cross-jet transport as $\overline{u'\eta'}$ is only at maximum 5 % of the total cross-jet transport.

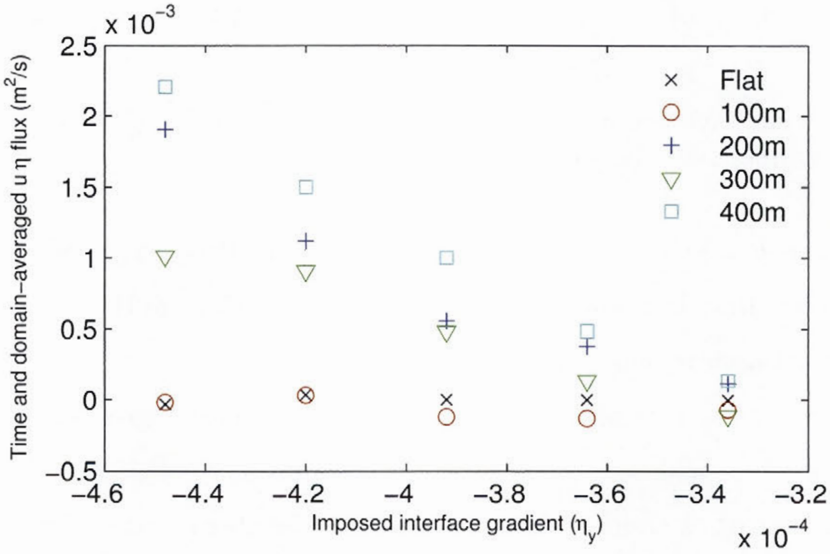

Figure 5–16: Domain-averaged zonal mass flux, $\langle\overline{u'\eta'}\rangle$, as a function of imposed meridional interface gradient, $\bar{\eta}_y{}^I$ for different topographies, showing presence of a non-zero skew-flux.

As was the case with the meridional fluxes, it is also true here that linear regressions on the data do not cross through the origin. That is zonal fluxes appear to decrease to zero for some non-zero $\overline{\eta_y}$. We estimate the intersect point for the 200m, 300m and 400m ridge, analogous to $\overline{\eta_y}^{crit}$ from Figure 5–14. The intercepts estimated from Figure 5–16 are similar but slightly higher (steeper slope) compared to η_y^{crit}. This again suggests a threshold $\overline{\eta_y}$ gradient $\overline{u'\eta'}$, below which $\overline{u'\eta'}$ fluxes are not observed. This leads us to propose an eddy diffusivity model relating $\overline{u'\eta'}$ fluxes to $[\overline{\eta_y} - \eta_y^{crit}]$. We choose to use the original η_y^{crit} estimated. We deem the linear trends in the data in Figure 5–16 to be less convincing those in Figure 5–14. Additionally, estimating $\overline{v'\eta'}$ and $\overline{u'\eta'}$ from the same $\nabla\overline{\eta}$ vector will allow us to write κ in a matrix form later on. We propose a model for a κ_{skew} in Equation 5.4. Note that κ_{skew} does not fall out as a scalar down-gradient eddy diffusivity from the classic model. It is a cross-correlation term in a matrix form of κ.

$$\overline{u'\eta'} \sim -\kappa_{skew}[\overline{\eta_y} - \eta_y^{crit}] \tag{5.4}$$

5.3.2 Meridional distribution of Mass Fluxes

We have now defined a κ_0 and κ_{skew} based on $\overline{\eta_y} - \eta_y^{crit}$. Both make sense from a global perspective however within the backflow regions, the interface gradient often drops close to or below η_y^{crit}(revisit Figure 5–12 and consider that η_y^{crit} for this topography is -3.19 x 10^{-4}). This leads to potential problems, particularly where $\overline{\eta_y} - \eta_y^{crit}$ becomes close to zero and κ becomes ill-defined. We consider how such κ could be applied by considering the meridional distribution of $\overline{v'\eta'}$ fluxes in Figure 5–17.

Figure 5–17(a) shows a $\langle\overline{v'\eta'}\rangle^x$ profile for a simulation with flat bottom topography at the reference forcing, where $\langle\rangle^x$ denotes a zonal average. We identify the average maximum and minimum values in the profile for each flat bottom simulation. Figure 5–17(b) then quantifies these maximum and minimum as a function of forcing.

A clear linear relationship is seen between $\langle\overline{v'\eta'}\rangle^x_{max}$ and F_f, or alternatively the imposed interface gradient. These occur in the jet cores where eddy generation is high, fed by the steep interface gradients. We expect steeper isopycnals to correspond to increased eddy kinetic energy (EKE) generation and increased eddy mixing, consistent with what we see here.

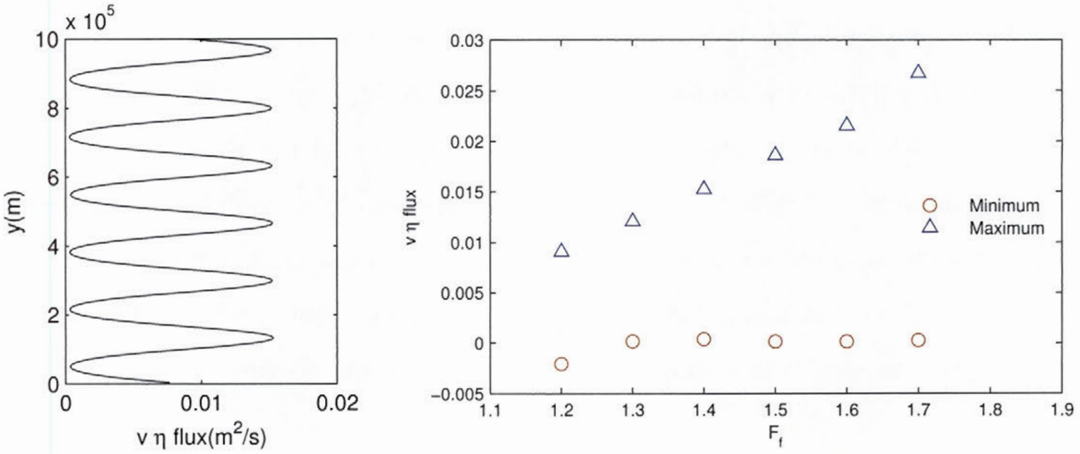

Figure 5–17: (a) Example of $\langle\overline{v'\eta'}\rangle^x$ profile for a flat run with $F_f = 1.4$, with peaks corresponding to jet cores. In (b) the minimum, $\langle\overline{v'\eta'}\rangle^x_{min}$, and maximum, $\langle\overline{v'\eta'}\rangle^x_{max}$, are computed from each flat bottom simulation and plotted against F_f.

The story with $\langle\overline{v'\eta'}\rangle^x_{min}$ fluxes is very different. The minimum shows no clear relationship with the imposed interface gradient and suggests an eddy diffusivity approach may not be justified here. Perhaps this should be unsurprising. Within the backflow regions the interface gradient often drops close to or below η_y^{crit}. If an eddy diffusivity were valid, it would either mean eddies are either increasing the available potential energy by steepening isopycnals (in this case a negative κ) or are further relaxing slopes below critical (a positive κ). Neither of these cases are readily supported by baroclinic instability theory. Moreover, $\overline{v'\eta'}$ fluxes in the backflow regions are roughly two orders of magnitude smaller than in the jet core. As this represents only a small portion of the mass transport, it may not be valuable parameterizing the fluxes in these backflow regions.

5.3.3 Summary

In this section, we presented simple, domain-averaged, eddy mass transport statistics to demonstrate that our data appears to support a downward gradient eddy diffusion model. In addition, the global zonal fluxes, $\langle\overline{u'\eta'}\rangle$, appear to vary with $\langle\overline{\eta_y}\rangle$. We find data for both zonal and meridional fluxes do not pass through the origin; that is, the fluxes become zero not for $\langle \overline{\eta_y} \rangle = 0$, but instead for $\langle \overline{\eta_y} \rangle = \overline{\eta_y}^{crit}$. This leads us to focus on relating zonal and meridional mass fluxes to $\overline{\eta_y} - \overline{\eta_y}^{crit}$. As such, we define a normal, κ_0, and skew, κ_{skew}, eddy diffusivity which can be written in a matrix form as in Equation 5.5. Our global statistics suggest κ_0 and κ_{skew} have dependence on the strength of the imposed forcing.

$$\begin{pmatrix} 0 & \kappa_{skew} \\ 0 & \kappa_0 \end{pmatrix} \begin{pmatrix} 0 \\ \overline{\eta_y} - \eta_y^{crit} \end{pmatrix} = \begin{pmatrix} -\overline{u'\eta'} \\ -\overline{v'\eta'} \end{pmatrix} \tag{5.5}$$

The problem arises in how to define κ in the backflow regions where $\overline{\eta_y}$ can be flatter that η_y^{crit}. We use the meridional distribution of $\overline{v'\eta'}$ fluxes to show that $\overline{v'\eta'}$ fluxes here in these backflow regions are also low. Additionally they show no clear correlation with forcing level. This leads us to believe that κ_0 and κ_{skew} should only be defined in the jets. We proceed in this manner and explore fitting κ_0 and κ_{skew} on a globally defined and on a locally defined basis in Section 5.4.

5.4 An eddy diffusivity with $\overline{\eta_y} - \eta_y^{crit}$

In light of the previous section we define eddy diffusivities according to the model proposed in Equation 5.5. We can either compute the two κ as global values over the domain or allow them to be defined at each grid point. The latter approach will allow us to see spatial variation in the two κ. We first compute the global eddy diffusivities, κ_0^g and κ_{skew}^g. We use the g superscripts to denote the global eddy diffusivities to avoid confusion. We will then go on to compute κ_0 and κ_{skew} at each grid point.

5.4.1 A global jet eddy diffusivity with $\overline{\eta_y} - \eta_y^{crit}$

Computation method for flat topography

Here we explain the computation method for κ_0^g and κ_{skew}^g for the flat bottom simulations. It is based on a rearrangement of Equation 5.5, where all variables are replaced with their spatially-averaged counterparts. In the spatial averages we choose to only include regions of the domain where $\overline{\eta_y} < \eta_y^{crit}$. This is motivated by Figure 5–17 where we only saw a relationship between $\overline{v'\eta'}$ in the jet core (where $\overline{\eta_y} < \eta_y^{crit}$) and the imposed gradient. Between the jets (where $\overline{\eta_y}$ is often flatter than η_y^{crit}), $\overline{v'\eta'}$ is small and does not appear to be explained by the interface gradient. It makes sense then that only regions able to be explained by $\overline{\eta_y}$ are included in an eddy diffusivity model.

The two κ^g are estimated from Equation 5.6 where the two spatial averages in each equation are restricted to flow areas where $\overline{\eta_y} < \eta_y^{crit}$. Physically it is a spatially averaged mass flux divided by the average value of $\overline{\eta_y} - \eta_y^{crit}$. Since the numerator and denominator are averaged separately first, we avoid potential problems where $\overline{\eta_y}$ becomes close to η_y^{crit} locally.

$$\kappa_0^g = -\frac{\langle \overline{v'\eta'} \rangle}{\langle \overline{\eta_y} - \overline{\eta_y}^{crit} \rangle} \qquad \qquad \kappa_{skew}^g = -\frac{\langle \overline{u'\eta'} \rangle}{\langle \overline{\eta_y} - \overline{\eta_y}^{crit} \rangle} \tag{5.6}$$

We will present the results for all flat bottom simulations shortly alongside those from the ridge simulations for comparison in Figure 5–18.

Computation method for ridge topography

Keep in mind that we are primarily interested in cross-jet transport. Since for the ridge cases the jets meander in the domain (review Figure 5–9), if we computed eddy diffusivities in the model coordinate system, as we did for the flat bottom case, then we will not quantify cross-jet transport. We therefore choose to compute eddy diffusivities in jet coordinates. The new along and cross-stream coordinate directions are aligned with the $\overline{\psi_1}$ field. Since $\overline{\psi_1}$ is, in turn, aligned with the jet cores (Thompson and Sallée, 2012), this new coordinate system will allow us to see transport across the jet cores.

At each grid point the fields are reorientated along axes parallel and perpendicular to $\overline{\psi_1}$ using Equations 5.7 to 5.9. Mass fluxes are denoted in jet coordinates as $\overline{\mu'\eta'}$ and $\overline{\nu'\eta'}$ corresponding to along-stream and normal directions respectively. Subscripts l and n will denote derivatives along and normal to these new orientations.

$$\overline{\nu'\eta'} = -\frac{\overline{\mathbf{u}'\eta'}.\nabla\overline{\psi_1}}{|\nabla\overline{\psi_1}|} = -\overline{u'\eta'}\frac{\overline{\psi_{1x}}}{|\nabla\overline{\psi_1}|} - \overline{v'\eta'}\frac{\overline{\psi_{1y}}}{|\nabla\overline{\psi_1}|} \tag{5.7}$$

$$\overline{\mu'\eta'} = -\frac{\overline{\mathbf{u}'\eta'}.\hat{k} \times \nabla\overline{\psi_1}}{|\nabla\overline{\psi_1}|} = -\overline{u'\eta'}\frac{\overline{\psi_{1y}}}{|\nabla\overline{\psi}|} + \overline{v'\eta'}\frac{\overline{\psi_1}}{|\nabla\overline{\psi_1}|} \tag{5.8}$$

$$\overline{\eta}_n = -\frac{\nabla\eta.\nabla\overline{\psi_1}}{|\nabla\overline{\psi_1}|} = -\overline{\eta_x}\frac{\overline{\psi_{1x}}}{|\nabla\overline{\psi_1}|} - (\overline{\eta_y} - \eta_y^{crit})\frac{\overline{\psi_{1y}}}{|\nabla\overline{\psi_1}|} \tag{5.9}$$

where $\overline{\psi_{1y}} = -\overline{\psi_{1y}}$ where $U < 0$. Firstly this maintains the sign of derivatives of η in y. Secondly, this means positive $\overline{\nu'\eta'}$ fluxes are always northward, consistent with those through the jet core. We choose to subtract η_y^{crit} from $\overline{\eta_y}$ prior to re-orientating. This makes sense if η_y^{crit} is considered to relate to baroclinic instability and the β-effect which acts uniquely in the y-direction. This inherently assumes that an equivalent η_x^{crit} would be zero and that baroclinic eddies are generated for any non-zero $\overline{\eta_x}$ to relax isopycnals towards $\overline{\eta_x} = 0$. We will check this assumption later in Section 5.5.2 when we parameterize mass fluxes with both $\overline{\eta_y}$ and $\overline{\eta_x}$.

κ_0^g and κ_{skew}^g can now be computed in the same way as for the flat bottom simulations, but now using the reorientated fields. Equation 5.10 is analogous to Equation 5.6 except that we have substituted fields in the new coordinate system. Since η_y^{crit} is already removed from $\overline{\eta}_n$, we are now spatially averaging only over grid points where $\overline{\eta}_n < 0$.

$$\kappa_0^g = -\frac{\langle\overline{\nu'\eta'}\rangle}{\langle\overline{\eta}_n\rangle} \qquad\qquad \kappa_{skew}^g = -\frac{\langle\overline{\mu'\eta'}\rangle}{\langle\overline{\eta}_n\rangle} \tag{5.10}$$

Given that the fields are reorientated as each grid point using local $\overline{\psi_1}$ derivatives, one may be concerned about the sensitivity of this computation to small scale variations in $\overline{\psi_1}$. We use this algorithm on the data from the flat bottom cases and compare the two κ_0^g given by Equation 5.6 and Equation 5.10. We find the two estimates vary at maximum by 1.2%.

κ_0^g and κ_{skew}^g for all simulations

We compute κ_0^g and κ_{skew}^g for each simulation as per the computation method described in the preceding two sections. The reorienatation of fields in the topography cases means that now κ_0^g is interpreted physically as a cross-jet eddy diffusivity and κ_{skew}^g as an along-jet eddy diffusivity. We compare the two κ in Figure 5–18 as a function of forcing. For clarity we only present the results for three topographies; the flat bottom, the 200m ridge and the 400m ridge. We find κ_0^g and κ_{skew}^g show a dependence on both topography and forcing strength.

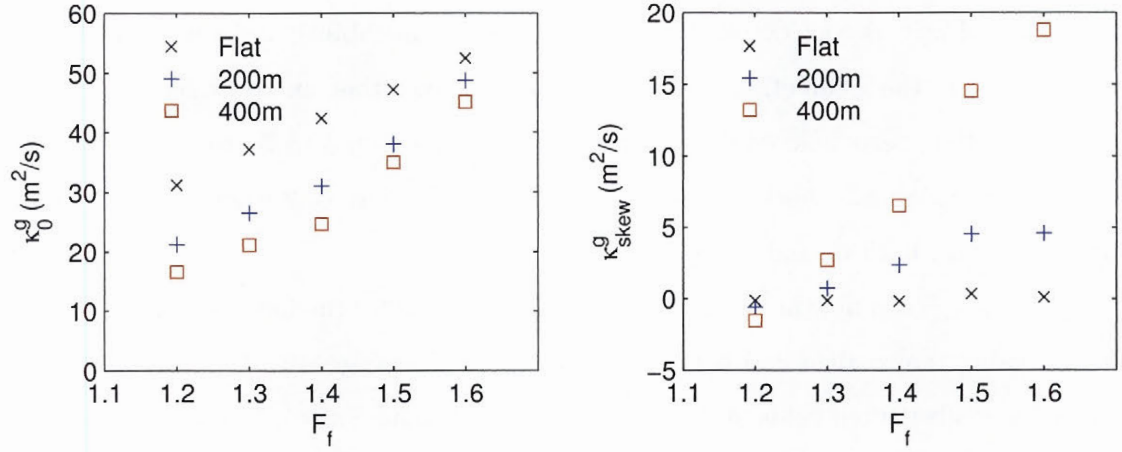

(a) κ_0

(b) κ_{skew}

Figure 5–18: (a) Global cross-jet diffusivity, κ_0^g, and (b) global skew diffusivity, κ_{skew}^g, as a function of forcing strength for runs with flat topography, 200 m ridge and 400 m ridge.

Let's first focus on κ_0^g presented in Figure 5–18. We find κ_0 to increase with forcing, implying $\overline{v'\eta'} \sim \kappa|\nabla\eta|\nabla\eta$. This is not unexpected after revisiting Figure 5–15. Here we saw a non-linear increase in $\langle\overline{v'\eta'}\rangle$ with $\langle\overline{\eta_y}\rangle - \eta_y^{crit}$. That is, at larger forcings we observed a steeper slope, representing a higher eddy diffusivity. The relationship with forcing appears to be linear for the flat bottom topography but for the ridge topography a linear relationship is less convincing. The stronger forcing increases the supply of potential energy in the jets, permitting higher EKE generation and leading to increased mixing (Sallée et al., 2008).

Now consider the dependence of κ_0 on topography height. We find in Figure 5–18 that κ_0 is highest for the flat bottom and reduces with topography. At first impression this may seem contradictory to that concluded by Thompson and Sallée (2012) who use a model similar to ours to show that cross-jet transport is maximum in the lee of the topography. However, their results show that the effect of the bottom topography is to localize the transport, rather than increase overall transport which in the domain. In fact, the domain-averaged κ_{eff} they define is infact lower in their ridge simulations (see their Figure 11), in agreement with what we observe in our results.

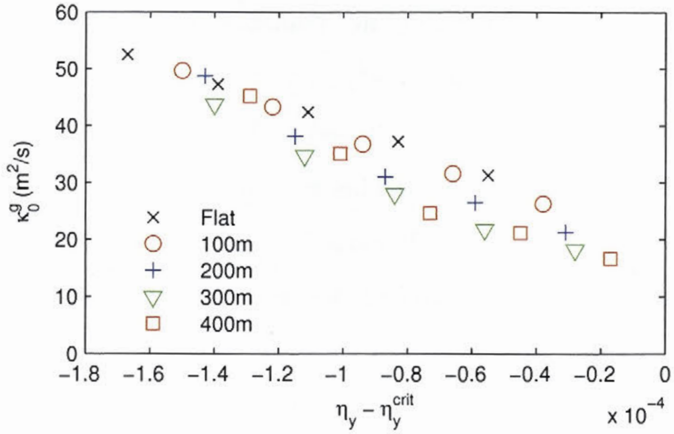

Figure 5–19: Cross-jet diffusivity, κ_0, as a function of $\overline{\eta_y} - \eta_y^{crit}$ for all topographies and forcing levels.

The decreasing trend in κ_0 with increasing topography height is also not unexpected after considering that we saw the same thing with $\langle\overline{v'\eta'}\rangle$ in Figure 5–14. If you recall, we were able to remove a large portion of the offset between the curves of the different topographies by re-plotting the data against $\langle\overline{\eta_y}\rangle - \eta_y^{crit}$ in Figure 5–15. We proceed to do the same here and re-plot κ_0 against $\langle\overline{\eta_y}\rangle - \eta_y^{crit}$ to see if the variation between topography is mainly due to a variation in η_y^{crit} between topographies. This is shown in Figure 5–19 where we see that the curves for the different topographies now lie much closer together. Although not all of the variation between the different topographies is explained by η_y^{crit} it certainly does explain a large part of the observed variation in Figure 5–18.

We now focus on κ_{skew}, shown in Figure 5–18(b). For the flat bottom topography we find κ_{skew} is closely centred around zero, similar to the globally averaged zonal fluxes, $\langle\overline{u'\eta'}\rangle$ (see Figure 5–16). In contrast, for the ridge topographies we find a non-zero κ_{skew} which appears to diverge with forcing. In other words, κ_{skew} increases with the level of forcing much faster for the higher ridges. This is the same behaviour that can be observed in $\langle\overline{u'\eta'}\rangle$.

We could speculate as to the origin of the skew flux. Consider that for the flat bottom topography $\overline{\psi_1}$ and $\overline{\eta}$ are both zonal. So ψ_1, or the computation axes, are aligned with $\overline{\eta}$ contours. If we assumed that the only net transport of mass fluxes is down $\overline{\eta}$ contours then we would not expect a net flux or κ_{skew}^g, which is what we see. Now for the ridge cases consider that $\overline{\psi_1}$ contours are not aligned with $\overline{\eta}$ contours $(\eta \sim \psi_2 - \psi_1)$, that is the current is mis-aligned with η contours. This misalignment can be seen by reviewing the fields in Figure 5–6 and Figure 5–7. If mass flux is indeed exclusively down $\overline{\eta}$ contours then the misalignment could be a source of the apparent skew flux that we observe for the ridge simulations.

One may be concerned about how much of the mass flux is accounted for by restricting the eddy diffusivity model to only regions where $\overline{\eta_y} < \eta_y^{crit}$. We find that across all simulations, $\overline{\eta_y} < \eta_y^{crit}$ (or alternatively $\overline{\eta_n} < 0$ for the ridge simulations) is met in 61% of the domain. The percentage varies between 46 - 96 %, increasing with increasing forcing. Given that the model is only applied in a little more than half of the domain, we want to make sure that in excluding these regions we are not discounting some of the mass flux. We find that within these regions lies 90 ± 7% of the total $\overline{v'\eta'}$ flux in the domain. This supports our notion to only base an eddy diffusivity model in these regions.

5.4.2 Spatially varying eddy diffusivity with $\overline{\eta_y} - \eta_y^{crit}$

We now allow κ_0 and κ_{skew} to vary spatially. The two eddy diffusivities are still defined as in Equation 5.5, however κ_0 and κ_{skew} now have a unique value at each grid point. We remind the reader that within the backflow regions, $\overline{\eta_y}$ is often flatter than η_y^{crit}. To define a κ here would either mean mesoscale eddies are steepening isopycnals or that they are further relaxing them below a critical slope (see Section 5.3.2); neither of which are logical. Given that the mass transport within these backflow regions is also small (Figure 5–17), it seems reasonable to set $\kappa = 0$ there. However, we are still faced with the problem of how to define the two κ when $\overline{\eta_y}$ approaches η_y^{crit}. We choose to truncate the computation at a threshold $\overline{\eta_y}$ value before κ tends to infinity. As we describe later, we will only choose to use jet core κ values to compare to previous results. This value is unaffected by the point at which we truncate κ.

Flat bottom topography

The estimation of κ_0 and κ_{skew} for the flat bottom simulation is relatively straightforward. The two κ are computed at each grid point according to to Equation 5.11. κ_0 is given by the time-averaged meridional mass flux at that point, $\overline{v'\eta'}$, divided by the difference between the interface gradient and the critical gradient, $\overline{\eta_y} - \eta_y^{crit}$. For κ_{skew} the computation is the same except using the zonal mass flux, $\overline{u'\eta'}$. The two κ are set to zero if $\overline{\eta_y} - \eta_y^{crit} > 0$.

$$\kappa_0 = -\frac{\overline{v'\eta'}}{\overline{\eta_y} - \eta_y^{crit}} \qquad\qquad \kappa_{skew} = -\frac{\overline{u'\eta'}}{\overline{\eta_y} - \eta_y^{crit}} \tag{5.11}$$

We find that along lines of constant latitude, the two κ fluctuate. We compute the standard deviations of these regular fluctuations and find them to be derived from those in the mass flux fields (see Figure 5–13). However, zonally averaging produces smooth profiles of which the general form is shared among all forcing levels. We present $\langle\kappa_0\rangle^x$ and $\langle\kappa_{skew}\rangle^x$, where $\langle\rangle^x$ denotes a zonal average, in Figure 5–20 for the simulation with an F_f

of 1.6. We use this simulation as an example as $\overline{\eta_y} < \eta_y^{crit}$ everywhere, i.e., so that κ is defined at every point in the domain. The κ profiles overlay mean velocity profiles.

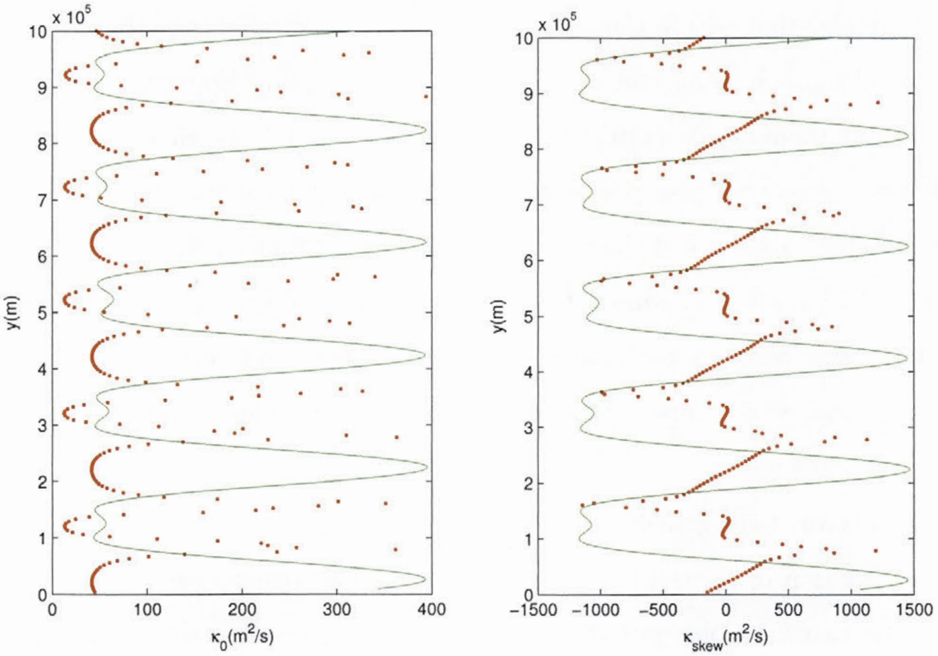

(a) κ_0 (b) κ_{skew}

Figure 5–20: $\langle\kappa_0\rangle^x$ and $\langle\kappa_{skew}\rangle^x$ computed for flat bottom topography and F_f of 1.6. The scale corresponds to κ, shown in red points, and overlying the mean velocity profile in green (scale not shown).

Both κ show meridional structure over the length scale of jets. In Figure 5–20(b), κ_0 is always positive indicating downgradient transport to the north. Within the jet cores κ_0 drops to local minima. This is consistent with several other authors (e.g. Marshall et al. (2006)) who believe jets in the ACC act as a barrier to mixing in the Southern Ocean. Its value increases outwards from the jet core until it begins to grow rapidly where $\overline{\eta_y}$ approaches $\overline{\eta_y}^{crit}$ and the denominator becomes close to zero. Within the backflow regions here, κ_0 is low due to the low $\overline{v'\eta'}$ fluxes here (review Figure 5–17). This is the only flat bottom simulation in which κ_0 is defined throughout the meridional profile. For all other forcings, κ_0 tends to infinity at the edges of the jet and is undefined in the backflow regions.

In Figure 5–20b (b), κ_{skew} alternates between positive and negative, reflecting the shape of the $\overline{u'\eta'}$ profile (revisit Figure 5–12). On the northern side of the jet, in negative mean shear, η' is transported westward. In positive mean flow shear η' is transported eastward. The rotational symmetry about the jet core explains why both $\langle\overline{u'\eta'}\rangle$ and κ^g_{skew} are close to zero for the flat bottom topography (Figure 5–18).

We take the series of $\langle\kappa_0\rangle^x$ profiles for all forcings with flat bottom topography. For each profile we compute an average value of κ_0 in the jet cores, κ_0^{jc}, by averaging across each jet in the domain. As F_f increases so too does $\overline{u_1}$ in the jet core. As $\overline{u_1}$ (or F_f) increases, κ_0^{jc} linearly increases with it. On one hand this makes sense. As the forcing level increases, we expect higher levels of EKE in the jets and more mixing. This is also in agreement with the observation that κ_0^g increases with forcing strength (Figure 5–18). On the other hand, within the jets in Figure 5–20(a) velocity appears to be negatively correlated with κ_0.

We wish to compare the estimates here to the global κ we computed in Section 5.4.1. Near the edge of the jets in Figure 5–20, κ_0 and κ_{skew} tend to high values or infinity. Some sort of spatial average which includes these values would not be robust. Therefore we choose to compare κ_0^{jc} to κ_0^g from Section 5.4.1. This seems reasonable as the maximum flux occurs in the jet core and κ_0^{jc} value does not lie on a sharp curve.
Figure 5–21 confirms the two methods produce comparable estimates. κ_0^{jc} is systematically less than κ_0^g. Although this is not unexpected it does confirm that the meridional structure of κ_0 (in Figure 5–20) is not simply an artifact in the computation where $\overline{\eta_y} - \eta_y^{crit}$ locally tends towards zero. Averaged over these runs κ_0^{jc} is suppressed to approximately 79% of the global value, κ_0^g.

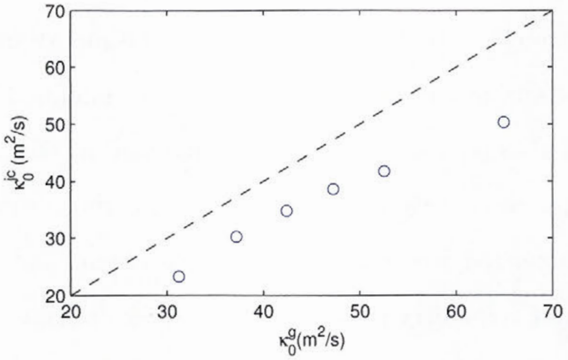

Figure 5–21: Comparison between κ_0 in jet core, κ_0^{jc}, and the globally computed cross-jet diffusivity, κ_0^g. Each data point represents a flat-bottom simulation. Dashed line is $\kappa_0^g = \kappa_0^{jc}$

Ridge topography

We now wish to compute some sort of analogy to Figure 5–20 for the ridge topography. In particular, we want to know if the structure of κ_0 and κ_{skew} in the jets remains the same when we add bottom topography. Like we did in Section 5.4.1, we will continue to work in a cross-stream and stream-wise coordinate system. Also like before, $\overline{\eta_y}^{crit}$ is subtracted prior to re-orientating and subsequently the κ are only defined at grid points where $\overline{\eta_n} < 0$. To avoid division by zero, in practice we implement $\overline{\eta_n} < \eta_y^{crit}/100$. We define κ_0 and κ_{skew} at each grid point according to Equation 5.12.

$$\kappa_0 = -\frac{\overline{\mu'\eta'}}{\overline{\eta_n}} \qquad\qquad \kappa_{skew} = -\frac{\overline{\nu'\eta'}}{\overline{\eta_n}} \tag{5.12}$$

Example fields of κ_0 and κ_{skew} are shown in Figure 5–22. These are for the 200 m ridge and F_f of 1.4 - the same reference case we used throughout Section 5.1.2. Our first aim is to test whether the structure of the two κ are the same throughout the jet profile as those seen with the flat bottom topography. We decided to compute an average following the jet core axis of the middle jet in the domain. The profile is initially computed along

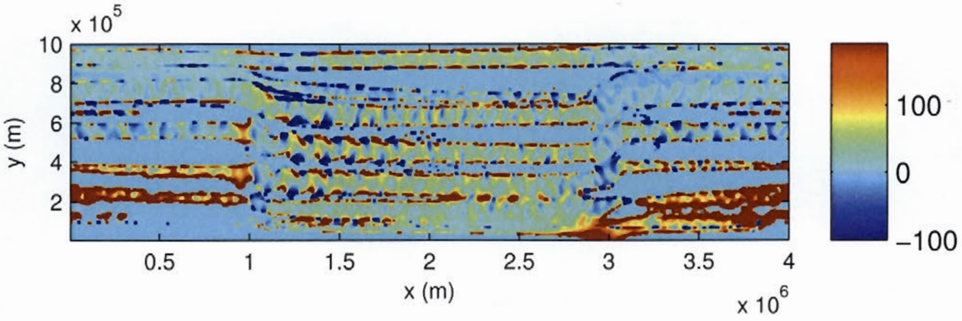

(a) κ_0

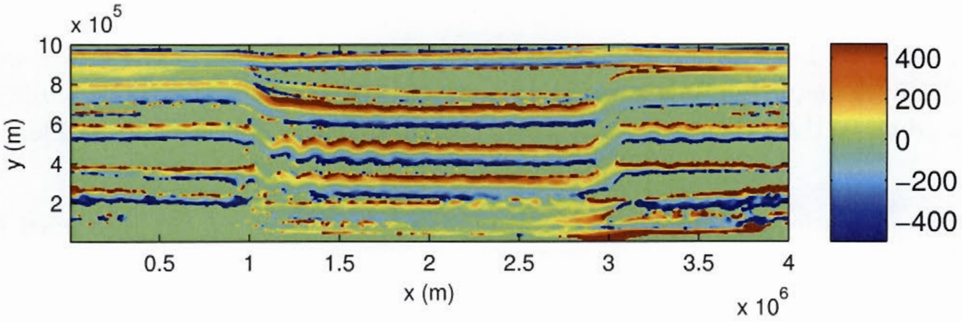

(b) κ_{skew}

Figure 5–22: κ_0 and κ_{skew} fields in m^2/s computed in axes parallel to the mean flow field. Simulation is ridge of 200 and forcing factor of 1.4.

$\overline{\psi_1}$ contours and scaled back to an effective y space. For this we take a profile in the mid-point of the domain of y values and their corresponding ψ_1 values. The averaged-profile in $\overline{\psi_1}$-space is mapped back to a y_{eff} using the pairing values in the conversion profile. This eliminates the possibility of a distorted look of the profile as ψ_1 contours are not equally spaced. We show these profiles of κ_0 and κ_{skew} in y_{eff} space in Figure 5–23.

Figure 5–23, although not as elegant as the flat bottom analogy in Figure 5–20, shows the same structure in κ_0 and κ_{skew} relative to the jet. κ_0 is minimum in the jet core and highest on the sides of the jets before dropping to zero in the backflow regions. Although κ_0 in the jet core can be seen to vary between jets in the domain in Figure 5–22, κ_0^{jc} is 23 m^2/s in the profile in Figure 5–23. This corresponds to 74% of κ_0^g computed for this

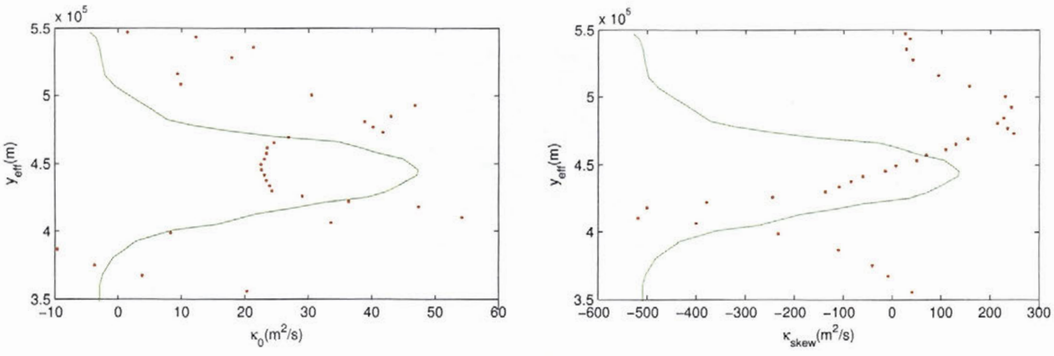

(a) κ_0 (b) κ_{skew}

Figure 5–23: Profiles of κ_0 and κ_{skew} averaged along lines of constant $\overline{\psi_1}$. Profiles are for the middle jet in domain from fields in Figure 5–22 (red data points are the eddy diffusivities corresponding to the y-axes labelling; green curves are the mean velocity profiles)

simulation. This level of suppression is not unlike that seen in flat bottomed cases in Figure 5–21 ($\kappa_0^{jc} \sim 79\% \kappa_0^{g}$). κ_{skew} has the same structure, positive on the northern side of the jet and negative on the southern side zero in the jet core. κ_{skew} is again zero in the jet core although we observe some asymmetry in the profile.

Take a step back and review the κ_0 and κ_{skew} fields in Figure 5–22, corresponding to the reference case we used early in Section 5.1.2. Recall that we remarked that the jets in the domain were not homogeneous in terms of their mass transport, velocity, and other properties shown in Section 5.1.2 and 5.2. Unsurprisingly, we also now see that the jets are not homogeneous in terms of their diffusivity properties.

In the preceding section, we saw that for the flat-bottom case, κ_0 in the jet core increased as we increased the forcing to produce stronger jets. If the same could be said here, then we would expect higher diffusivities on the northern flanks of the ridge where jet velocities are higher. Instead we observe the contrary in Figure 5–22(a), and also in the raw mass flux fields in Figure 5–12. The result suggests that $(\eta_b)_y$ has an effect on mass fluxes. To consider a possible explanation, recall that on the northern flank of the ridge, the topography has a stabilizing effect (Section 5.1.1). If $(\eta_b)_y < 0$ persisted throughout the entire domain, then we could expect that U_{onset}, and therefore η_y^{crit} to be higher. We could therefore suppose that the domain-averaged $\langle\overline{\eta_y^{crit}}\rangle$ is locally underestimate on the northern flank, and by this argument we would expect κ_0, estimated from Equation 5.12, to be an underestimate. To remove the inhomogeneity between the jets one could use a spatially varying η_y^{crit}. A more straightforward approach might be to try absorb the apparent effects of bottom topography into another parameter.

5.4.3 Summary

κ_0 and κ_{skew} are computed according to the form proposed in Section 5.3 at both a global and local scale. We find κ_0^g increases with forcing and reduces with topography height over the strengths of forcings we used. κ_{skew}^g is zero for the flat bottom topography but increases with topography height and forcing strength. We then allow κ_0 and κ_{skew} to vary in the across jet direction. We are able to recover similar profiles for both κ_0 and κ_{skew} through the jet with both the flat bottom and ridge topography. We find κ_0 is a local minimum in the jet core, consistent with many authors who believe the jet cores are barriers to mixing. The κ_{skew} profile alternates between positive on the northern side of jet cores and negative on the southern side of jet cores. This is not unlike the meridional profile in $\overline{u'\eta'}$ seen earlier in Figure 5–12. In the flat bottom cases, jets in the domain have equal eddy diffusivity properties. In the ridge cases there is large scale variation in κ maps. For these ridge cases we are not completely satisfied that all of the variation can be explained by $\overline{\eta_n}$.

5.5 A Matrix Eddy Diffusivity

We are motivated to see if some of the variation in κ_0 and κ_{skew} in Figure 5–22 can be explained by a second variable. The parameterization in the previous section is extended to a matrix form to include this additional parameter. The eddy diffusivity takes the following form where m is the second variable and α_i are the eddy diffusivity matrix coefficients. Note that we recover $\alpha_2 = \kappa_{skew}$ and $\alpha_4 = \kappa_0$ by setting $m = 0$.

$$\begin{pmatrix} \alpha_1 & \alpha_2 \\ \alpha_3 & \alpha_4 \end{pmatrix} \begin{pmatrix} m \\ \overline{\eta_n} \end{pmatrix} = \begin{pmatrix} -\overline{\mu'\eta'} \\ -\overline{\nu'\eta'} \end{pmatrix} \tag{5.13}$$

5.5.1 A Second Regression Variable

Correlations with $\overline{\eta_x}$

We first consider whether $\overline{\eta_x}$ and $\overline{\eta_y}-\eta_y^{crit}$ could replace m and $\overline{\eta_n}$ in the eddy diffusivity matrix in Equation 5.13. $\overline{\eta_x}$ is a natural partner to $\overline{\eta_y}$ and variations in $\overline{\eta_x}$ occur mainly in the jet, with little variation between the jets. It also falls out of the GM90 parameterization, $\overline{\mathbf{u}'\eta} \sim \kappa\nabla\overline{\eta}$, by taking κ to be a matrix.

Flat bottom topography. κ_0 and κ_{skew} were estimated using $\overline{\eta_y} - \eta_y^{crit}$ in Section 5.4.2. The resultant κ_0 and κ_{skew} show small scale variation along lines of constant latitude. This is on the same scale as the variation in $\overline{\eta_x}$, $\overline{u'\eta'}$ and $\overline{v'\eta'}$ fields (see Section 5.2.2). One may be tempted to try using $\overline{\eta_x}$ to explain the variation. If $\overline{\eta_x}$ could explain this variation then we should see a correlation between mass fluxes and $\overline{\eta_x}$. Using the flat bottom reference simulation ($F_f = 1.4$) we show these correlation plots in Figure 5–24. Unfortunately the lack of correlation does not give hope.

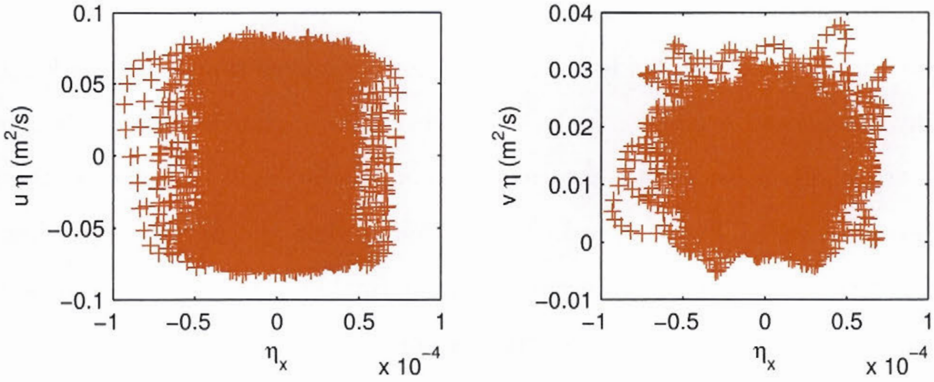

(a) $\overline{u'\eta'}$ (b) $\overline{v'\eta'}$

Figure 5–24: Correlations between $\overline{\eta_x}$ and thickness fluxes at each grid point, showing no correlation in the data. Data is from flat bottom simulation with $F_f = 1.4$.

Moreover these variations in $\overline{u'\eta'}$, $\overline{v'\eta'}$ and $\overline{\eta_x}$ occur on such small scales that they would not be resolved by any non-resolving eddy model. Therefore the results of any such parameterizaton would not be meaningful in practise. With this in mind, we decide not to try fitting a matrix eddy diffusivity model for the flat bottom topography.

Ridge topography. In Section 5.4.2 κ_0 and κ_{skew} were diagnosed parallel and perpendicular to the local mean flow field using $\overline{\eta_n}$. $\overline{\eta_y} - \eta_y^{crit}$ was replaced with $\overline{\eta_n}$ (Equation 5.9) to absorb much of the large scale variation in $\overline{\eta_x}$. Although using $\overline{\eta_n}$ makes sense and is based on the fundamentals, in practise it would require computing jet paths, locally realigning fields, computing cross and along jet transport before finally superimposing mass fluxes back into the model coordinate system. It would certainly be much more computationally efficient to compute fluxes directly in the model coordinate system. A matrix form with $\overline{\eta_x}$ is also suggested by some references (e.g. Vallis 2006). We therefore decide to try fitting the classic matrix eddy diffusivity form with $\overline{\eta_x}$ and $\overline{\eta_y} - \eta_y^{crit}$ in the ridge simulations.

Correlations with η_b

Recall that κ_0 and κ_{sk} fields suggest a negative correlation with the local bottom topography meridional gradient, $(\eta_b)_y$. On the northern flanks of the ridge, where jet velocities are highest, we would have expected κ_0 to be high. On the southern flanks we initially anticipated lower κ_0 values. We found that the opposite of what we had expected was true (refer back to Section 5.4.2 for further details). We suppose that this variation could be explained by considering a bottom topography parameter in addition to $\overline{\eta_n}$. Given that we are in along and cross stream coordinates we choose to use $(\eta_b)_n$ for consistency. $(\eta_b)_n$ here is the bottom topography derivative normal to the flow direction. On the northern and southern flanks, where the jets are close to zonal (see Figure 5–9), $(\eta_b)_n \sim (\eta_b)_y$.

Summary

For the flat bottom topography, we choose not to extend the eddy diffusivity model to a matrix form. For the ridge topography we will first attempt an eddy diffusivity matrix with $\overline{\eta_x}$ and $\overline{\eta_y}$, aligned with the model coordinate system. In applications, this would allow large scale variations in $\overline{\eta_x}$ to be taken into account without having to compute mass transport in jet coordinates. We will then compute the matrix parameterization in jet coordinates using $(\eta_b)_n$ and $\overline{\eta_n}$. To avoid confusion, in the matrix eddy diffusion model with $\overline{\eta_x}$ and $\overline{\eta_y}$ we denote the matrix coefficients, α_i, with upper case letters A, B, C and D. In the matrix form with $(\eta_b)_n$ and $\overline{\eta_n}$ we use the lower case letters a, b, c and d.

5.5.2 A Global Matrix Diffusivity

Computation Approach

The same method is used for fitting a global diffusivity matrix using both gradient pairs in turn which we explain here. For demonstration purposes we describe the method in terms of the paramterization with η_{bn} and $\overline{\eta_n}$. For the first matrix eddy diffusion model we will fit, η_{bn} and $\overline{\eta_n}$ are replaced with $\overline{\eta_x}$ and $\overline{\eta_y} - \eta_y^{crit}$. Mass fluxes, $\overline{\mu'\eta'}$ and $\overline{\nu'\eta'}$, are replaced with their counterparts in Cartesian coordinates, $\overline{u'\eta'}$ and $\overline{v'\eta'}$. As before, only regions where $\overline{\eta_n} < 0$ (or equivalently $\overline{\eta_y} < \eta_y^{crit}$ in Cartesian coordinates) are considered. With only four unknowns and two equations at every grid point the problem is overdetermined. However if two points are selected at random then the four coefficients can be uniquely determined using the construction below.

$$\begin{pmatrix} (\eta_{bn})_1 & (\overline{\eta_n})_1 & 0 & 0 \\ 0 & 0 & (\eta_{bn})_1 & (\overline{\eta_n})_1 \\ (\eta_{bn})_2 & (\overline{\eta_n})_2 & 0 & 0 \\ 0 & 0 & (\eta_{bn})_2 & (\overline{\eta_n})_2 \end{pmatrix} \begin{pmatrix} a \\ b \\ c \\ d \end{pmatrix} = \begin{pmatrix} -(\overline{\mu'\eta'})_1 \\ -(\overline{\nu'\eta'})_1 \\ -(\overline{\mu'\eta'})_2 \\ -(\overline{\nu'\eta'})_2 \end{pmatrix} \tag{5.14}$$

If another two grid points are randomly selected then another unique solution can be computed and so on. Eventually a running average of the four coefficients converges to a non-zero value. This method is able to get around the fact that both $\langle\overline{\eta_x}\rangle$ and $\langle(\eta_b)_n\rangle$ are identically zero. Figure 5–25 shows an example of the convergence of the four constants to non-zero values for our reference simulation.

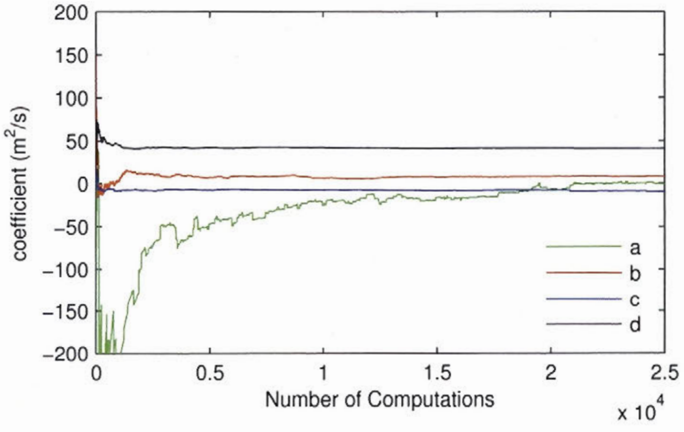

Figure 5–25: Running average of coefficients a, b, c and d computed for a global matrix, showing convergence of values to a constant value. This data is from a simulation with 200m ridge and F_f of 1.4.

If the two chosen points in Equation 5.14 are identical then the matrix is non-invertible and the system does not have a unique solution. Similarly, if the two points are too similar the computation contains a large error. For this reason we impose a condition on the determinant of the matrix to filter the selection of points. Since a measure of a "good" condition for the determinant varies with the magnitudes of the involved fields, we find it more robust to impose a condition determined by the average determinant for each simulation. Since a non-invertible matrix has a determinant of zero, we require that the determinant be greater in magnitude than a percentage of the average absolute determinant. Three thresholds are tested; 1%, 0.1%, 0.01%. Lower thresholds begin to produce numerically non-invertible matrices in some cases. Figure 5–26 gives a example comparison of the results of the three thresholds on two matrix coefficients. The estimates do vary with the threshold used, although the trend we observe with the forcing is statistically larger than the error. Generally making the threshold more strict produces estimates closer to zero. We choose to proceed with 0.01% to avoid unnecessarily excluding data.

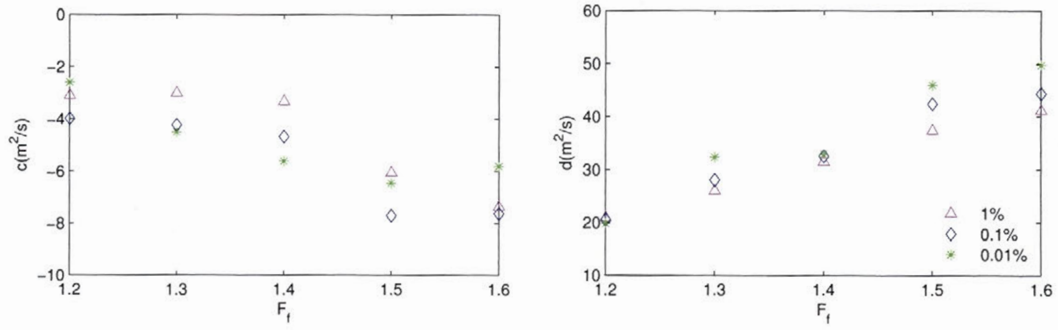

(a) c (b) d

Figure 5–26: Coefficients c and d for 100 m ridge, showing the sensitivity of the estimates to the condition imposed on the determinant of the matrix.

Global eddy diffusivity matrix fitted with $\overline{\eta_x}$ and $[\overline{\eta_y} - \eta_y^{crit}]$

Equation 5.15 is fitted as per the method in the preceding section using $\overline{\eta_x}$ and $\overline{\eta_y} - \eta_y^{crit}$. The four constants are plotted in Figure 5–27 as a function of forcing, where each data point represents a simulation. Both A and D are normal diffusivities as they describe down-gradient transport. The remaining two constants are skew diffusivities.

$$\begin{pmatrix} A & B \\ C & D \end{pmatrix} \begin{pmatrix} \overline{\eta_x} \\ \overline{\eta_y} - \eta_y^{crit} \end{pmatrix} = \begin{pmatrix} -\overline{u'\eta'} \\ -\overline{v'\eta'} \end{pmatrix} \tag{5.15}$$

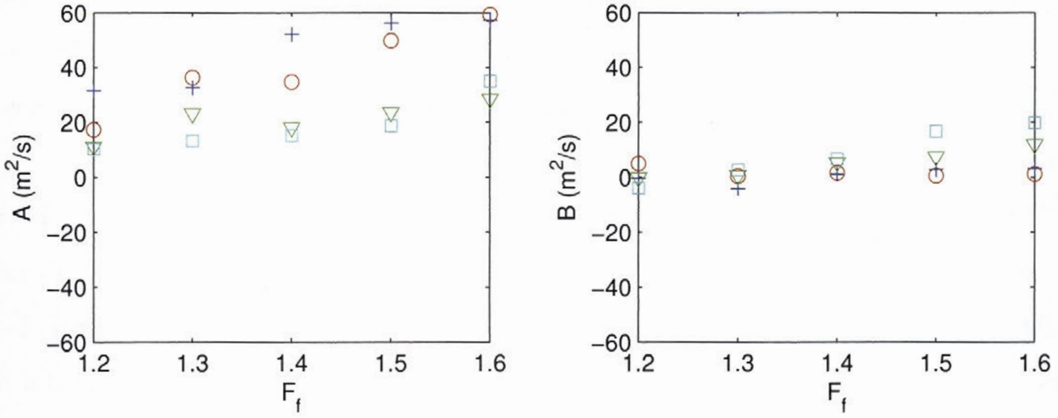

(a) A (b) B

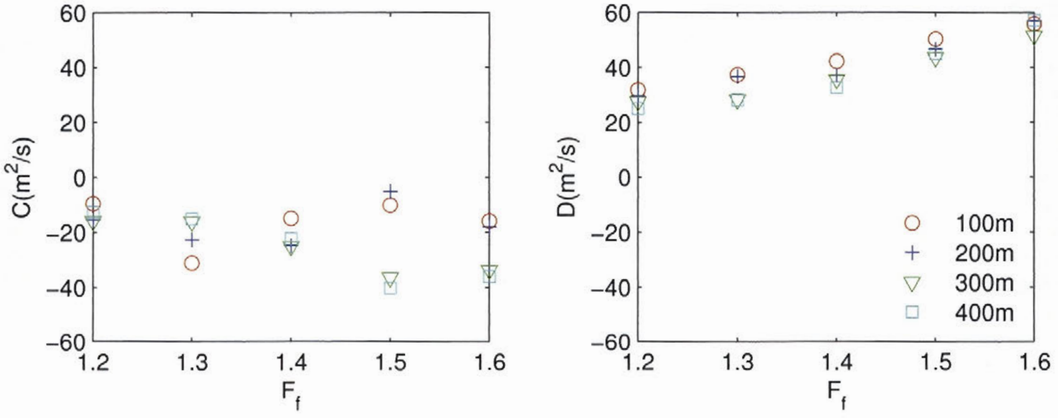

(c) C (d) D

Figure 5–27: Coefficients computed for global eddy diffusivity matrix using $\overline{\eta_x}$ and $[\overline{\eta_y} - \eta_y^{crit}]$. For each simulation we plot the 4 constants in the four panels as a function of F_f.

B is a zonal skew flux described by $\overline{\eta_y} - \eta_y^{crit}$ (analogous to κ_{skew}). B is close to zero for the lower topographies and weaker forcings. It is non-zero and positive for the higher ridges at higher forcings, suggesting a net eastwards flux. This is exactly the same behaviour we saw with κ_{skew} (see Figure 5–18) and in $\langle\overline{u'\eta'}\rangle$ (Figure 5–16). Although κ_{skew} was computed in jet coordinates, whereas B is in model coordinates, we will compare the two in magnitude shortly in Figure 5–31. C is a meridional skew eddy diffusivity; it relates a meridional mass flux to the zonal interface gradient $\overline{\eta_x}$. For higher topographies, C shows a convincing linearly decreasing trend. The negative sign indicates that $\overline{v'\eta'}$ is transported up $\overline{\eta_x}$ contours. We do see this transport on the downward slope of the ridge at approximately $x = 1000$km. $\overline{\eta_x}$ is large and negative here (see Figure 5–11), where we also see high $\overline{v'\eta'}$ fluxes (see Figure 5–12).

The two normal diffusivities, A and D, increase with forcing as κ_0 did. D is more or less independent of topography height whereas A reduces with increases topography height. Recall that κ_0^g varied with both topography and forcing (review Figure 5–18). This suggests the topography dependence of κ_0^g lies in a difference in transport down $\overline{\eta_x}$ contours. This makes sense as it is the topography height which dictates $\overline{\eta_x}$ in the field whereas $\overline{\eta_y}$ is primarily a function of the forcing.

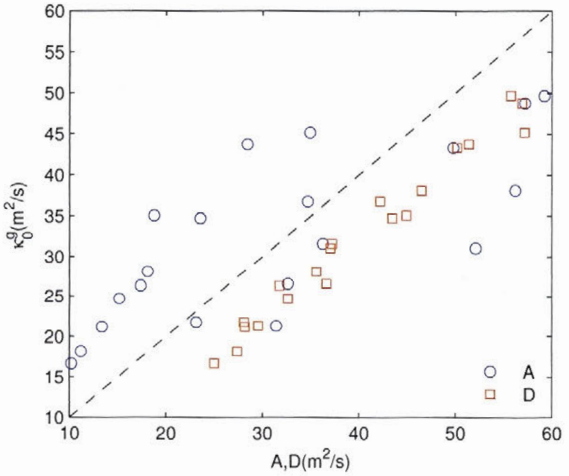

Figure 5–28: Comparison of κ_0^g with A and D coefficients, which both parameterize down-gradient transport, for each simulation.

As the jets closely follow η contours, we expect the κ_0^g we computed earlier in jet coordinates to be some sort of combination of both A and D. Although A and D are not drastically different in value, Figure 5–28 shows $D > \kappa_0^g$ while $A \sim \kappa_0^g$ although there is more scatter in this parameter. It suggests a slight bias in mass transport, that is that mass fluxes are in general more easily transported down $\overline{\eta_y}$ contours than $\overline{\eta_x}$. It alternatively mean that the estimates of η_y^{crit} we are using are too steep.

Recall that in Section 5.4.1 we first introduced the idea of computing eddy diffusivities in along and cross stream coordinates. We were faced with an uncertainty of how to define the new interface gradient perpendicular to $\overline{\psi_1}$ contours, $\overline{\eta_n}$. We assumed that η_y^{crit} was related uniquely to baroclinic instability in the y-direction and decided to subtract η_y^{crit} from $\overline{\eta_y}$ prior to realigning the axis in Equation 5.9. We noted that this inherently assumed an equivalent η_x^{crit} was zero and mass fluxes would always be generated for any non-zero $\overline{\eta_x}$. If this assumption is correct then we should see that η' is transported just as easily down $\overline{\eta_x}$ as $\overline{\eta_y} - \eta_y^{crit}$. In other words A and D would be equal in this matrix parameterization. What we find in Figure 5–28 is that this is largely the case. This backs up our earlier assumption that η_y^{crit} is only a threshold gradient in the y-direction and supports our method of computing $\overline{\eta_n}$ in Equation 5.9.

Global eddy diffusivity matrix fitted with $(\eta_b)_n$ and $\overline{\eta_n}$

We go back to the reason that initially motivated us to try fitting a matrix eddy diffusivity model. We want to see if some of the large scale variation in Figure 5–22 can be absorbed by a bottom topography parameter. We return to using jet coordinates to isolate the effects of the topography so that we can compare the results to previous estimates. We justify this as $A \simeq D$ is seen to loosely hold from the preceding section. A global matrix of the form in Equation 5.16 is fitted for each simulation using the method described earlier in this section.

$$\begin{pmatrix} a & b \\ c & d \end{pmatrix} \begin{pmatrix} (\eta_b)_n \\ \overline{\eta_n} \end{pmatrix} = \begin{pmatrix} -\overline{\mu'\eta'} \\ -\overline{\nu'\eta'} \end{pmatrix} \tag{5.16}$$

where $(\eta_b)_n = \nabla\eta_b.\hat{n}_\psi$ and $\hat{n}_\psi$ is the unit vector locally normal to $\overline{\psi_1}$ contours. The four coefficients a, b, c and d are shown in Figure 5–29 for each simulation. We consider a physical interpretation of each of the coefficients in following.

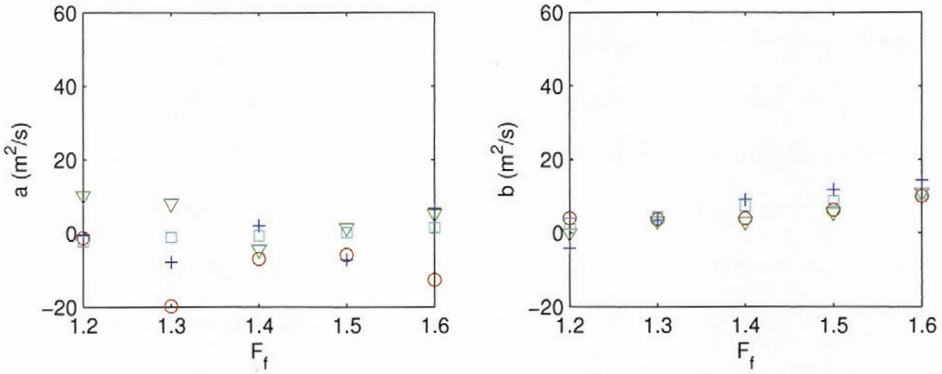

(a) a (b) b

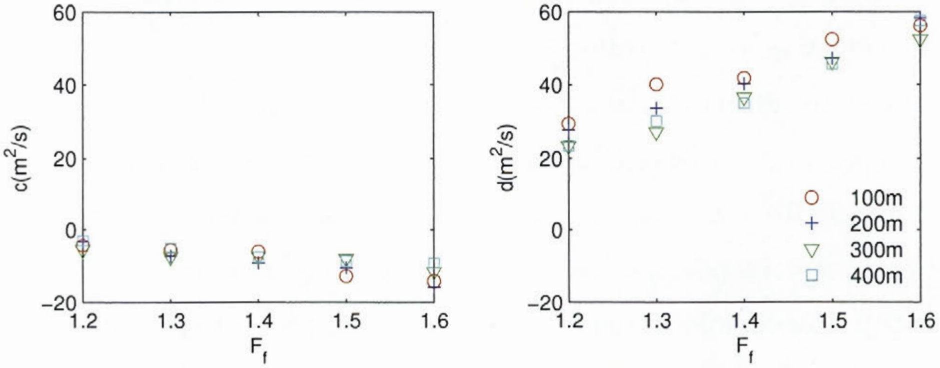

(c) c (d) d

Figure 5–29: Coefficients a, b, c and d computed for eddy diffusivity matrix using $(\eta_b)_n$ and $\overline{\eta_n}$. For each simulation we plot the 4 constants in the four panels as a function of F_f.

a is a skew diffusivity quantifying the effects on $\overline{u'\eta'}$ of of the bottom topography gradient perpendicular to it. If a were non-zero we would expect to see a difference in the *net* zonal flux on the northern and southern flanks of the ridge. Review Figure 5–12(a). We can only really say that $(\eta_b)_n$ appears to affect the magnitude of $\overline{u'\eta'}$ fluxes but there is no obvious effect on the net transport. We could expect a local a might be valid, but not on a global scale. As expected the estimates of a follow no pattern and that the parameter is not roust computationally; it was much slower to converge compared to the other three coefficients (review Figure 5–25) and sometimes even non-convergent. Note that the validity of a as a parameter does not affect estimates obtained of c or d from the computation method in Equation 5.14.

d always parameterizes the cross-jet transport. Like we did with A and D in Figure 5–28, we compare d to κ_0^g in Figure 5–30. Both κ_0^g and d are computed in stream-wise coordinates and we see a very good agreement between the two parameters.

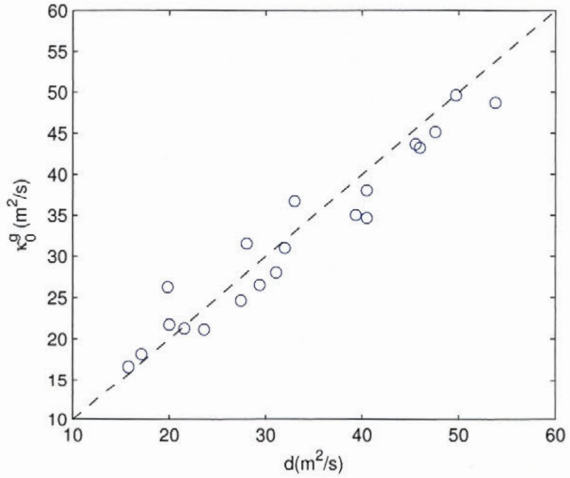

Figure 5–30: Comparison of κ_0^g with d coefficients for each simulation showing good agreement and validating the matrix results for this parameter.

c is a parameter which adjusts the cross-jet transport according to the bottom topography gradient. Here we find c to be negative. This translates to suppressed cross-front eddy diffusivities on negative slopes (in this case on the northern flanks of the ridge) and higher eddy diffusivities on positive slopes (southern flanks here). This is what we observed and hypothesized from Figure 5–22. We note that c is only a local correction of the estimated mass transport. As we saw in Figure 5–30, $\kappa_0^g \sim d$. This means over the entire domain, the net effect of c with our topography is not to increase or decrease transport but just to redistribute it. However we consider the local significance of c as a parameter. Recall that the total cross jet mass flux from Equation 5.16 is given here as $c(\eta_b)_n + d\overline{\eta_n} = -\overline{\nu'\eta'}$. From Figure 5–29 c is smaller in magnitude than d and may not seem worth modelling. However $(\eta_b)_n$ can locally be much larger than $\overline{\eta_n}$ making the $c(\eta_b)_n$ term a significant adjustment.

We consider the root-mean square of the two gradients $\overline{\eta_n}$ and $(\eta_b)_n$ and the magnitude of their corresponding contribution to the cross-jet mass flux; $c(\eta_{bn})_{rms}$ and $d\overline{\eta_n}_{rms}$. We do this for the reference case in Table 5–1, considering statistics for both the entire domain then a portion of the domain. If we consider the entire domain then the $|d\overline{\eta_n}_{rms}|$ term dominates in magnitude. If we consider only the first quarter of the domain, with the ridge in it, then we find $|c(\eta_{bn})_{rms}|$ is 36 % of the magnitude of the $|d\overline{\eta_n}_{rms}|$ term.

Table 5–1: Comparison between c and d terms estimated for 200m high ridge and F_f of 1.4.

	$(\eta_{bn})_{rms}$	$\lvert c(\eta_{bn})_{rms}\rvert$	$\overline{\eta_n}_{rms}$	$\lvert d\overline{\eta_n}_{rms}\rvert$
Whole Domain	2.27 x 10^{-4}	2.07 x 10^{-3}	3.08 x 10^{-4}	1.23 x 10^{-2}
$x = 0$ to $L_x/4$	4.34 x 10^{-4}	3.96 x 10^{-3}	2.74 x 10^{-4}	1.10 x 10^{-2}

As the topographic height increases, $\overline{\eta_n}_{rms}$ does not change significantly but $(\eta_{bn})_{rms}$ increases. For example, for the 400 m ridge at the reference forcing, $(\eta_{bn})_{rms}$ is almost three times the size of $\overline{\eta_n}_{rms}$. The c coefficient therefore provides an increasingly important adjustment on the estimated $\overline{\nu'\eta'}$ for the higher topographies. This makes sense if we reconsider the argument that the bottom topography gradient affects baroclinic instability.

If the gradient is steeper then we expect is to have a larger impact on the baroclinic instability and meridional mass transport. When we allow this matrix parameterization to vary spatially in the following section we will see again that this term can be locally significant.

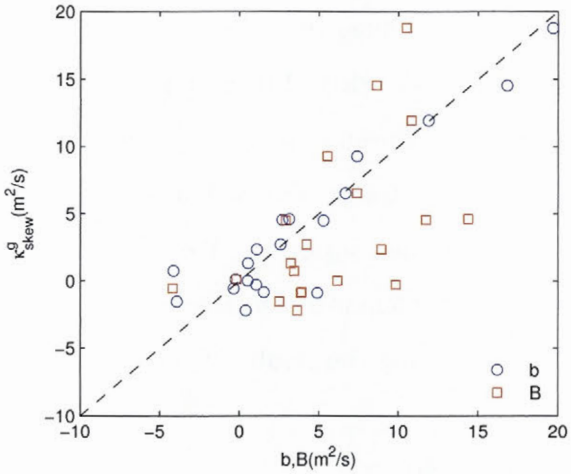

Figure 5–31: Comparison of κ^g_{skew} with B and b coefficients, which both equivalently characterize the skew flux, for each simulation.

We consider the remaining b coefficient in the matrix parameterization in Figure 5–29. A non-zero b points again to a net skew flux in the eastwards direction. It peels off the x axis for larger values of topography and forcing like B and κ_{skew} did. We compare κ_{skew} with B and b in Figure 5–31. b and κ_{skew} are closely related. The same could be said in general for B although there is much more scatter in the data. This makes sense as κ_{skew} and b are both estimated in stream-wise coordinates whereas B was computed in the model coordinate system.

Summary

The two matrix parameterizations we just saw allowed us to describe mass transport in terms of two gradients. The first parameterized $\overline{u'\eta'}$ and $\overline{v'\eta'}$ with $\overline{\eta_x}$ and $\overline{\eta_y} - \eta_y^{crit}$. An important point to take from these results is that we found mass transport occurred almost equally as easily down $\overline{\eta_x}$ as $\overline{\eta_y} - \eta_y^{crit}$. We used this result to move back into an along and cross stream coordinate system to parameterize $\overline{\mu'\eta'}$ and $\overline{\nu'\eta'}$ with $(\eta_b)_n$ and $\overline{\eta_n}$. The coefficients we computed suggested that including this bottom topography gradient was able to account for some of the large scale variations in mass transport we observe in the ridge simulations. We are still interested in gaining a better insight of the local importance of bottom topography gradients on mass transport.

5.5.3 Spatially varying matrix eddy diffusivity

We will now allow matrix coefficients from the parameterization using $(\eta_b)_n$ and $\overline{\eta_n}$, given in Equation 5.16, to vary spatially. This will allow us to see more clearly the local effects of bottom topography on mass transport. We seek a unique solution at each point with only two equations so the problem is under-determined. We describe the computation method in following before discussing the results of the parameterization for the reference simulation.

Computational Approach

We find the most robust approach is to gain information using surrounding data points. A 9 by 9 square is drawn around each data point, $p_{i,j}$, where the square's corners are defined by and include $p_{i-4,j-4}$, $p_{i+4,j-4}$, $p_{i-4,j+4}$ and $p_{i+4,j+4}$. The method from the previous section is modified and applied. $p_{i,j}$ is paired each in turn with every other data point in the square to compute a unique solution for the four constants (a, b, c and d). The immediately surrounding 8 data points are excluded as they are often too similar to $a_{i,j}$. Overall, 72 pairings are made at each point.

The solution for the four constants at $p_{i,j}$ is determined by a combination of all pairing results. Solutions from each pair are weighted in the average according to the distance between the two points. As eddy diffusivities vary over a jet length scale we use the Rhines scale to non-dimensionalize the distance. Here we use $L_{Rh} \sim 2\pi(U/\beta)^{1/2}$ as we found the constant of 2ψ (as suggested by Thompson and Sallée (2010)) to give a good approximation to our jet spacings (see Section 5.1.2). The final solution depends to an extent on the weighting function used and here we use an exponential function, giving closer points more weighting. The coefficient vector at each point, $X_p = (\ a \ b \ c \ d \ )^T$, is computed from Equation 5.17.

$$X_p = \frac{1}{\sum_k w_k} \sum_k w_k X_{pk} \tag{5.17}$$

$$w_k = \exp(-\frac{d_k^2}{L_{Rh}^2}) \tag{5.18}$$

where d_k is the distance between the two points, w_k is the weight function and X_{bk} is the solution vector of each pairing. In Section 5.5.2 we imposed a condition on the determinant of the matrix to prevent large errors in computing X_p with two points that were too similar. We will continue to use the same condition here. We only define the parameterization where $(\eta_b)_n \neq 0$ and $\overline{\eta_n} < 0$.

Example fields of the four coefficients for the reference simulation are shown in Appendix A. The constants which relate mass fluxes to $(\eta_b)_n$ (a and c) peak in the domain at the zonal edges of the ridge. This is consistent with the maximum fluxes observed here (see Figure 5–12). a alternates between positive just north of jet cores and negative just south. Its values are highest on the northern flank, predicting higher fluxes. Both these observations are consistent with observations of mass flux field patterns in Figure 5–12. In general, b and d show less spatial variation than their corresponding scalar fields, κ_0 and κ_{skew} (Figure 5–22). We can conclude that consideration of the effects of bottom topography is able to account for some of the variability seen in diffusivity estimates in Section 5.4.2.

Again we are interested in the magnitude of the two terms which parameterize the cross-jet flux; $-c(\eta_b)_n - d\overline{\eta_n} = \overline{\nu'\eta'}$. We plot a meridional profile of the these three terms in Figure 5–32 at an x-position coincident with the ridge. We see in the $\overline{\nu'\eta'}$ a net northward flux. $\overline{\nu'\eta'}$ is only non-zero where the jets are and close to zero in the backflow regions. The $-c(\eta_b)_n$ term is generally positive on the southern flanks of the ridge and negative on the northern flanks. This corresponds to an enhanced eddy diffusivity on the southern flanks and a suppressed eddy diffusivity on the northern flanks. This is exactly what we saw in the scalar κ_0 we computed for the same simulation in Figure 5–22. This also means the c coefficient is, for the most part, negative as we found in the corresponding global matrix parameterization in Figure 5–29.

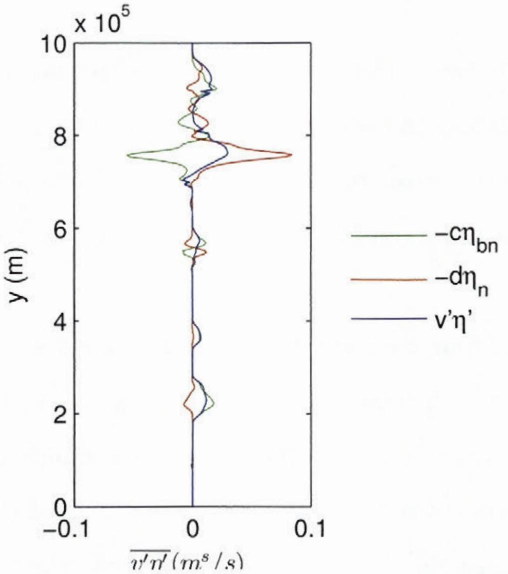

Figure 5–32: Profile showing for a spatially varying matrix eddy diffusivity showing the two terms which estimate the total $\overline{\nu\eta'}$; $-c(\eta_b)_n$ and $-d\overline{\eta_n}$. Profile is taken from the reference case and averaged between x=70 km and x=140km.

Let us focus on the jet at approximately y=750km in the profile in Figure 5–32. This is approximately the location of the maximum negative $(\eta_b)_n$ in the profile. If we had predicted the size of the mass flux $\overline{\nu'\eta'}$ based on $\overline{\eta_n}$ alone, then we would have overestimated $\overline{\nu'\eta'}$ by more than a factor of 2. In this case, including the effects of bottom topography led to a significant correction.

5.5.4 Summary

Here we allowed κ in the GM90 parameterization to be defined as a matrix for the ridge simulations. The first matrix parameterized $\overline{u'\eta'}$ and $\overline{v'\eta'}$ with $\overline{\eta_x}$ and $\overline{\eta_y} - \eta_y^{crit}$.

We found all four coefficients to be non-zero. We then moved back into cross and along stream coordinates, computing cross and along stream mass transport using $\overline{\eta_n}$ and $(\eta_b)_n$. We found that globally all parameters were non-zero except a - a parameter predicting the effects of $(\eta_b)_n$ on $\overline{\mu'\eta'}$. We then allowed the four constants of this latter matrix parameterization to vary spatially and be defined at each grid point. We found the bottom topography can be locally quite significant in terms of predicting mass transport.

5.6 Sensitivity to L_D and comparison of κ in literature

As we explain shortly, we find is that our values tend to be on the lower side of those in the literature. This motivated us to test the sensitivity of mass transport and eddy diffusivity parameterization to an important parameter in our model; the Rossby radius. Our main simulations used a Rossby Radius of $L_y/64$ (15.6km). We test the sensitivity to L_D by comparing results from the main simulations to those from a second set of simulations with twice this L_D, that is $L_y/32$ (31.3km). In our model L_D is imposed through the reduced gravity term, g', thus increasing L_D increases the density in the lower layer (see Section 4.2).

We comment first on the qualitative differences between the solutions at statistical equilibrium. Recall the instantaneous PV fields presented earlier to demonstrate the effect of forcing in Figure 5–8. We observed that by increasing F_f, the jets became larger and more turbulent. To show the effect of L_D, in Figure 5–33 we compare two flat-bottom simulations at the reference forcing ($F_f = 1.4$) for the two L_D. We see that increasing L_D has the same effect as increasing F_f; that is to make the jets larger and stronger. Physically this makes sense as both parameters affect the amount of energy contained in the forcing term. For the same imposed interface gradient, increasing g' increases the density gradient and is able to supply more potential energy to the flow. As the Rhines scale is linearly related to the Rossby radius the jets in Figure 5–33(b) are approximately double in size.

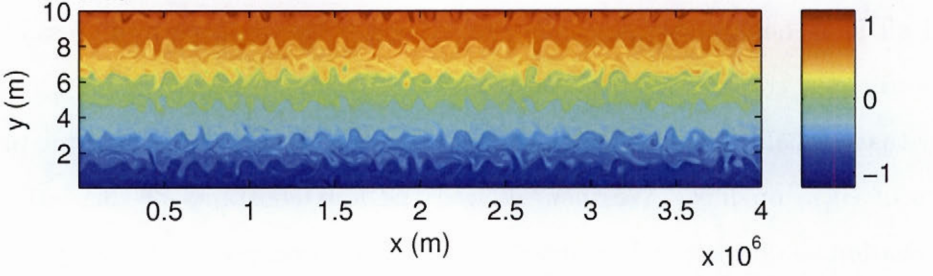

(a) $L_D = L_y/64$

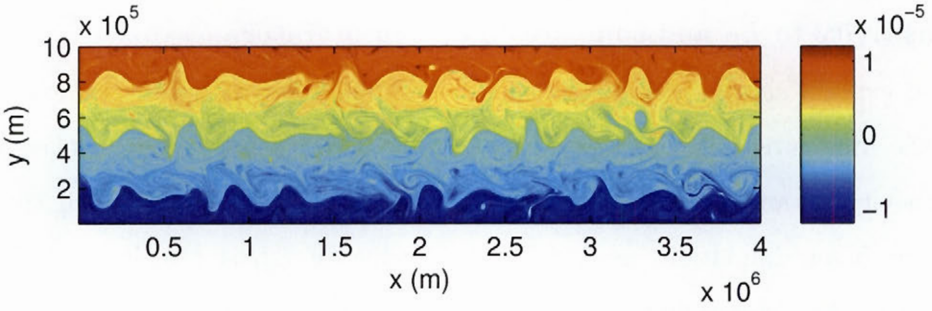

(b) $L_D = L_y/32$

Figure 5–33: Instantaneous upper layer PV fields for simulations with (a) $L_D = L_y/64$ and (b) $L_D = L_y/32$, showing the effect of L_D. Both panels are for flat bottom simulations with F_f of 1.4.

Note that although the critical shear velocity is larger in the $L_y/32$ simulations, the critical gradient is independent of L_D and remains the same.

We decide to quantify the significance of L_D on mass transport by comparing global normal eddy diffusivities for the two sets of simulations. We compute κ_0^g for the two sets of simulations as per the method in Section 5.4.1. Recall that we found κ_0^g increased with F_f (Figure 5–18). Based on this and the above argument that both F_f and L_D increase the energy in the forcing term, we may expect that κ_0^g would also increase with L_D. We find this to be true in Figure 5–34 which compares κ_0^g for the two L_D. The plot shows a large sensitivity to L_D that increases with forcing strength. κ_0 are 290-430 % higher in runs with $L_D/32$, than in runs with $L_D/64$ with corresponding forcing strength. This

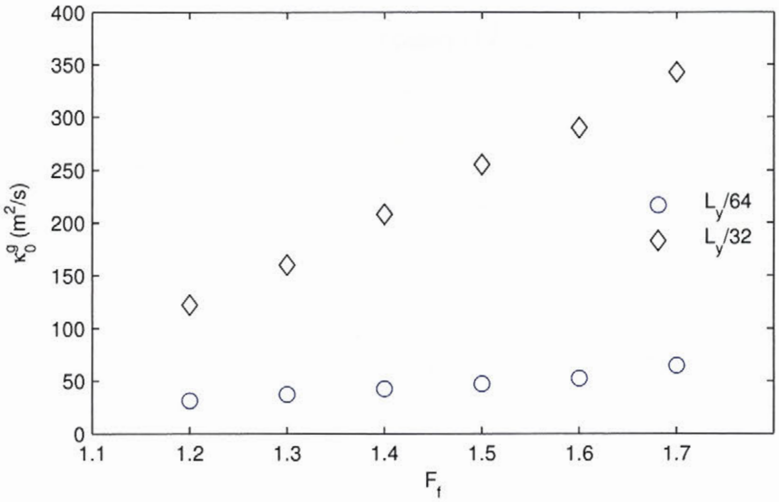

Figure 5–34: Global cross-jet diffusivity, κ_0^g, as a function of F_f for runs with flat bottom topography. Runs are shown for two Rossby Radii; $L_y/32$ and $L_y/64$, to demonstrate the influence of L_D on κ_0^g.

indicates a non-linear relationship between κ and L_D. Although we do not test the type of relationship that our data follows, Bryan (1996) suggests $\kappa \sim L_D^2$. Nonetheless, these results show the importance of a correctly defined local Rossby radius.

We will now use Figure 5–34 to compare the size of κ_0^g we found in this work to those in the literature. Referring back to Section 3.2.1, we find our results to be notably lower than the κ_0^g which we find in our main simulations with $L_D = L_y/64$ (Figure 5–34). Those given in the literature review are surface values whereas ours could be thought of as more of a depth integrated value for the upper 2000 km. We know that κ declines with depth (Eden, 2006). As a simplification we could assume an exponential decay, where κ_0 decays to 50% of the surface value by 500 m. Using this profile, a depth-averaged value over the upper 2000 m corresponds to 34% of the surface value. We could compare to a lower-end surface eddy diffusivity quoted in the literature within the ACC of 200 m^2/s (e.g. Naveira Garabato et al. 2011). Using the assumed exponential profile, this surface value corresponds to a depth-averaged κ_0^g of 67 m^2/s. This falls within the upper range of our estimates in the main simulations. Whereas, a typical value often adopted throughout the entire ocean of 1000 m^2/s (Eden, 2006) equates to a depth-averaged κ_0 of 340 m^2/s. This falls well within the range of κ_0^g we estimate using a Rossby radius of 32 km. Although this is a crude comparison it does verify that our values are on a comparable order of magnitude.

5.7 Summary

In this Chapter we discussed and analyzed the results from our model. In Section 5.1 we discussed the formation of the quasi-steady jets and their structure at statistical equilibrium. Recalling that the GM90 parameterization predicts that $\overline{\mathbf{u}'\eta'} \sim -\kappa\nabla\overline{\eta}$, we looked qualitatively at the mass flux and interface gradient fields in Section 5.2. In Section 5.3 we quantitatively tested whether the GM90 parameterization made sense for our data. We found that our data was more appropriately modelled using a gradient of $\overline{\eta_y} - \eta_y^{crit}$. Based on this result we proceeded to fit a series of increasingly complex eddy diffusivity models which we summarize in Table 5–2.

Table 5–2: Summary of eddy diffusivity models fit in this thesis

	Type of Model	Mathematical form	Section
(1)	Global with $\overline{\eta_y} - \eta_y^{crit}$	$\langle\overline{\mu'\eta'}\rangle = -\kappa^g_{skew}\langle\overline{\eta_n}\rangle$; $\langle\overline{\nu'\eta'}\rangle = -\kappa^g_0\langle\overline{\eta_n}\rangle$	5.4.1
(2)	Local with $\overline{\eta_n}$	$\overline{\mu'\eta'} = -\kappa_{skew}\overline{\eta_n}$; $\overline{\nu'\eta'} = -\kappa_0\overline{\eta_n}$	5.4.2
(3a)	Global matrix with $\overline{\eta_x}$ and $\overline{\eta_y} - \eta_y^{crit}$	$\begin{pmatrix}\overline{u'\eta'}\\ \overline{v'\eta'}\end{pmatrix} = -\begin{pmatrix}A & B\\ C & D\end{pmatrix}\begin{pmatrix}\overline{\eta_x}\\ \overline{\eta_y} - \eta_y^{crit}\end{pmatrix}$	5.5.2
(3b)	Global matrix with $(\eta_b)_n$ and $\overline{\eta_n}$	$\begin{pmatrix}\overline{\mu'\eta'}\\ \overline{\nu'\eta'}\end{pmatrix} = -\begin{pmatrix}a & b\\ c & d\end{pmatrix}\begin{pmatrix}(\eta_b)_n\\ \overline{\eta_n}\end{pmatrix}$	5.5.2
(4)	Local matrix with $(\eta_b)_n$ and $\overline{\eta_n}$	$\begin{pmatrix}\overline{\mu'\eta'}\\ \overline{\nu'\eta'}\end{pmatrix} = -\begin{pmatrix}a & b\\ c & d\end{pmatrix}\begin{pmatrix}(\eta_b)_n\\ \overline{\eta_n}\end{pmatrix}$	5.5.3

As forcing increases we found the cross-jet eddy diffusivity increases. We also found a non-zero eastwards flux for the higher topographies at large enough forcings. Although interesting, in reality the transport in the zonal direction by mesoscale eddies is dwarfed by the mean flow. Our latter parameterizations included the bottom topography gradient perpendicular to the flow direction, and aimed to absorb some of the large-scale spatial variation seen in the κ_0 fields. Locally bottom topography gradients were important, although the addition of the ridge did not have a huge impact on the net transport in the domain (Figure 5–14). However, we may expect that this would not be the case for non-symmetric topography, especially given that we found parameters relating bottom topography to mass transport to be non-zero. Finally in comparing our results to previous work we found that the Rossby radius is very important. At higher L_D larger more energetic eddies are generated and result in more mixing. Typically κ is diagnosed from the density gradient (Nakamura and Chao, 2000). In our model the density field is a function of both the imposed interface gradient and the reduced gravity term (inferred from the set Rossby radius, L_D). Steeping the interface gradient or increasing L_D, increases the density gradient. In these results we find both of these to increase κ, consistent with $\kappa \sim \nabla\rho$.

Chapter 6
Conclusions

The work in this thesis explored the parameterization of mesoscale eddy mass transport in the ACC using a two-layer quasi-geostrophic model. The domain had a physical size of 4000 km by 1000 km and was modelled using doubly periodic boundary conditions. The model forcing was based on the Phillips problem for baroclinic instability in a two-layer system and energy removal carried out by hyperviscosity and bottom drag. The forcing was implemented by maintaining a base state inclination of the interface between the fluids, such that the flow is baroclinically unstable and permits the generation of baroclinic eddies. The energy moves to larger scales by the inverse cascade, and finally when energy saturation is reached, quasi-geostrophic jets are formed in the domain. The strength of the forcing was increased by increasing the base state inclination of the interface. Our bottom topography included a flat bottom and idealistic ridge of varying height. Simulations were carried out over a series of combinations of ridge heights and forcing strengths. Model outputs of time averaged mass transport and mean flow properties were used to explore fitting eddy diffusivity relationships. We noted that κ in the GM90 parameterization can mathematically, in principal, be implemented as a scalar or matrix where in either case it can be defined globally or locally. We considered five parameterizations for κ ranging from a global constant to a matrix description of mass transport. Given that our model setup was highly idealized, we were more concerned about the ways in which κ depended on the topography height and forcing, rather than the actual numbers themselves per se.

The classic Phillips problem for two-layer baroclinic instability derives a critical instability condition based on the inclination of the interface. For our corresponding flat bottom topography case, we found an instability condition of approximately 70% of that of the classic result. This was determined to be the result of the bottom friction in our model, and the classic condition is recovered when the bottom drag is returned to zero. Although it is well-known that bottom friction increases the baroclinicity of flows, this result was a little counter-intuitive and surprising. A theoretical condition for instability, taking bottom drag into account, was not derived but could be a part of future work.

Once instability was activated, two completely different growth modes were observed in the flat bottom and ridge cases. In the flat bottom simulations, kinetic energy in the system grew exponentially. During this period, primarily one mode was growing which could be seen by a very regular structure in the fields. Its wavelength was close to one of the modes of fastest growth predicted by baroclinic instability. In contrast, the total kinetic energy growth in the system showed no resemblance to that of the flat bottom case. In these cases, the interaction between the topography and forcing excited a large scale structure almost instantly. This large scale structure evolved and grew with time. Baroclinic instability growth began to occur at a later time and preferentially where bottom topography slopes favoured instability. For both types of topography, energy eventually reached saturation and statistical equilibrium was attained. At this time quasi-steady jets were observed in the domain, typical of β-plane turbulence. Once the solutions achieved statistical equilibrium, or energy saturation, they were averaged in time.

In the upper layer peak eastwards velocities, corresponding to jet cores, alternated with regions of either weaker eastwards flow or westward flow. As the level of forcing was increased the jets became larger and stronger. In the ridge simulations, the jets took a meridional excursion in the lee of the topography. We related this to the conservation of PV of fluid columns as they are stretched moving off the ridge. Jets were found to be strongest on our northern flanks of the ridges, where the bottom topography slopes down towards the equator, and were attributed to the local stabilizing PV gradient of the topography slope. In the lower layer closed recirculation regions were found in the valley between the ridges. Since the initial goal of this work was to explore the effect of these quasi-steady jets on the κ structure, our subsequent analysis was focused on the upper layer mass transport and dynamics.

Recall that the GM90 eddy diffusivity model predicts that $\overline{\mathbf{u}'\eta'} \sim \kappa\nabla\overline{\eta}$. We first considered simple, global eddy statistics to show that our data better suited an eddy diffusivity fitted against $\overline{\eta_y} - \eta_y^{crit}$. The critical interface slope, η_y^{crit}, can be interpreted as a slope, below which, no mass flux occurs. For the flat bottom case, η_y^{crit} corresponded to the empirically derived onset of critical instability. Considering this, it makes sense that $\overline{\eta_y} - \eta_y^{crit}$ could be understood as a measure of "how unstable" the flow is, or the level of excess potential energy. When we looked in regions of the flow where $\overline{\eta_y}$ was locally flatter than η_y^{crit} (in the backflow regions), little eddy mass flux was present and the data did not locally support an eddy diffusivity model. In contrast, mass flux data appeared to locally follow an eddy diffusivity model where the interface gradient was steeper than η_y^{crit}. This motivated us to move forward, only defining an eddy diffusivity model where $\overline{\eta_y} < \eta_y^{crit}$. In addition, since we were primarily interested in cross-jet transport, eddy diffusivities were computed in a jet coordinate system which followed $\overline{\psi_1}$ contours and was aligned with jet cores.

For each simulation we computed a κ_0 and a κ_{skew}, which related $\overline{\nu'\eta'}$ (cross-jet mass transport in jet coordinates) and $\overline{\mu'\eta'}$ (along-jet mass transport in jet-coordinates) respectively to $\overline{\eta_n}$ (interface gradient normal to jet contours with $\overline{\eta_y}^{crit}$ removed). We computed the two κ on a global scale before allowing each to have a local definition. The global cross-jet diffusivity, κ_0^g, increased with forcing strength, consistent with higher levels of EKE and therefore mixing taking place. A local definition of κ_0, in all topography cases, had a meridional structure consistent with that believed by many others. κ_0 dropped to a local minimum through the jet core, suggesting mixing inhibition, and increased moving outwards from the core. This led to an apparent conflict, or paradox, between locally and globally defined cross-jet diffusivities. In a global sense, as the forcing, and therefore jet core velocities increased, so too did κ_0^g. In a local sense and following the same logic, we might have expected that as we move into the jet core, into regions of the higher velocity, that a local κ_0 would also increase. Instead we found the contrary to be true. Although we did not find a concrete explanation for this, it appears to support both seemingly contradictory arguments in the literature that diffusivities are suppressed in the jet cores but yet κ_0 is positively correlated with EKE.

Mass transport along jet contours is typically given much less attention since along-stream transport is dominated by the mean flow. Nonetheless, we considered an along-stream diffusivity, κ_{skew}, in the same manner as that for κ_0. Within the jets, a local κ_{skew} was found to be positive on the northern sides of jet cores and negative on the southern sides. This structure was derived from the eastwards transport of η' on the northern side of jet cores and westwards transport of η' on the south. In the flat bottom simulations, $\overline{u'\eta'}$ was found to average to zero over the domain indicating no net zonal transport of η'. Subsequently, a global κ^g_{skew} was found to be zero. In contrast, in the ridge simulations, a net eastwards transport of η' and non-zero positive κ_{skew} was observed. The value of κ_{skew} increased with both forcing strength and topography height. The source of the skew flux could have been the result of a misalignment of $\overline{\psi}$ and $\overline{\eta}$ contours in the ridge simulations.

It was noted that the GM90 parameterization could be mathematically correct either if κ was defined as a scalar or as a matrix. For the ridge simulations, we experimented with the idea of fitting an eddy diffusivity in matrix form. Given that it may be more practical to compute mass transport directly in model coordinates rather than in jet coordinates, our first global matrix parameterized meridional and zonal transport using $\overline{\eta_x}$ and $\overline{\eta_y} - \eta_y^{crit}$. The coefficients which related zonal fluxes to $\overline{\eta_x}$ was approximately equal to those relating meridional fluxes to $\overline{\eta_y} - \eta_y^{crit}$. This confirmed our early assumption that an equivalent critical gradient in the zonal direction, η_x^{crit}, would be zero.

For the ridge simulations, the scalar eddy diffusivity fields, κ_0 and κ_{skew}, appeared to be correlated with bottom topography. That is we did not observe the same eddy diffusivities on the northern flanks of the ridge, as on the southern flanks or in flat regions in the valley. This motivated a second global eddy diffusivity matrix. This time we reverted back to jet coordinates and tried to absorb the spatial variation in the two κ by introducing the bottom topography gradient as a second regression variable. We found a global eddy diffusivity to be suppressed on our northern flanks, where the gradient sloped down towards the equator and the gradient has a baroclinically stabilizing effect. This could be interpreted in several ways, however, we could consider that η_y^{crit} is locally increased and therefore the flow is "less unstable" and we expect less mass transport; exactly that which we observed in the raw mass transport fields. For our final eddy diffusivity parameterization, we extended this same matrix parameterization with bottom topography but now permitting it to vary locally. The problem was now under-determined as we sought four coefficients with only two equations and the results could have been expected to vary depending on the method used to close the system. However, our results showed the matrix coefficients equivalent to κ_0 and κ_{skew} showed much less large scale variation than their scalar counterparts.

Our diffusivity values were noted to be on the lower end of those found in the literature, motivating a further set of simulations at double the Rossby radius. The Rossby radius, L_D, was observed to have a significant impact, both visually in the velocity and PV fields and quantitatively in terms of mass transport. κ_0 was found to have a large and non-linear dependence on L_D, which increased with the strength of forcing. Currently, in practice, eddy diffusivities are diagnosed from the meridional density gradient. In this thesis, the meridional density gradient was determined by the separately defined interface gradient and Rossby radius.

This work was initially motivated to understand the changes of κ with the future changes to the ACC and the role topography may play in this evolution of κ. From our idealized model, we could expect the cross-jet diffusivity to increase with an increase in the meridional density gradient. Our symmetric idealized topography did not have a significant influence on the net cross-jet transport in the domain. However, based on the parameterizations with bottom topography gradients, one could expect that asymmetric topography could have a net effect to either increase or decrease a large scale cross-jet diffusivity.

References

Abernathey, R., Marshall, J., Mazloff, M., and Shuckburgh, E. (2010). Enhancement of mesoscale eddy stirring at steering levels in the southern ocean. *Journal of Physical Oceanography*, 40(1):170–184.

Briggs, W. L., McCormick, S. F., et al. (2000). *A multigrid tutorial*, volume 72. Siam.

Bryan, K. (1996). The role of mesoscale eddies in the poleward transport of heat by the oceans: a review. *Physica D: Nonlinear Phenomena*, 98(2):249–257.

Cushman-Roisin, B. (1994). *Introduction to Geophysical Fluid Dynamics.* Prentice-Hall, Inc.

Dukowicz, J. and Greatbatch, R. (1999). The bolus velocity in the stochastic theory of ocean turbulent tracer transport. *Journal of physical oceanography*, 29(9):2232–2239.

Eden, C. (2006). Thickness diffusivity in the southern ocean. *Geophysical research letters*, 33(11):L11606.

Eden, C., Greatbatch, R., and Willebrand, J. (2007). A diagnosis of thickness fluxes in an eddy-resolving model. *Journal of physical oceanography*, 37(3):727–742.

Farneti, R., Delworth, T., Rosati, A., Griffies, S., and Zeng, F. (2010). The role of mesoscale eddies in the rectification of the southern ocean response to climate change. *Journal of Physical Oceanography*, 40(7):1539–1557.

Ferrari, R. and Nikurashin, M. (2010). Suppression of eddy diffusivity across jets in the southern ocean. *Journal of Physical Oceanography*, 40(7):1501–1519.

Garrison, T. (2004). *Essentials of Oceanography 3e.* Brooks-Cole - Thomson Learning.

Gent, P. (2011). The gent–mcwilliams parameterization: 20/20 hindsight. *Ocean Modelling*, 39(1):2–9.

Gent, P. and Mcwilliams, J. (1990). Isopycnal mixing in ocean circulation models. *Journal of Physical Oceanography*, 20(1):150–155.

Gent, P., Willebrand, J., McDougall, T., and McWilliams, J. (1995). Parameterizing eddy-induced tracer transports in ocean circulation models. *Journal of Physical Oceanography*, 25(4):463–474.

Gilat, A. and Subramaniam, V. (2011). *Numerical Methods for Engineers and Scientists: An Introduction with Applications using MATLAB.* Wiley.

Gille, S. (2002). Warming of the southern ocean since the 1950s. *Science*, 295(5558):1275–1277.

Hogg, A., Meredith, M., Blundell, J., and Wilson, C. (2008). Eddy heat flux in the southern ocean: Response to variable wind forcing. *Journal of Climate*, 21(4):608–620.

Kantha, L. and Clayson, C. (2000). *Numerical models of oceans and oceanic processes*, volume 66. Academic press.

Kuhlbrodt, T., Smith, R., Wang, Z., and Gregory, J. (2012). The influence of eddy parameterizations on the transport of the antarctic circumpolar current in coupled climate models. *Ocean Modelling*, 52–53:1–8.

Lu, J. and Speer, K. (2010). Topography, jets, and eddy mixing in the southern ocean. *Journal of Marine Research*, 68(3-4):3–4.

Marshall, J., Shuckburgh, E., Jones, H., and Hill, C. (2006). Estimates and implications of surface eddy diffusivity in the southern ocean derived from tracer transport. *Journal of physical oceanography*, 36(9):1806–1821.

McWilliams, J. (2006). *Fundamentals of geophysical fluid dynamics.* Cambridge University Press.

McWilliams, J. and Chow, J. (1981). Equilibrium geostrophic turbulence i: A reference solution in a β-plane channel. *Journal of Physical Oceanography*, 11(7):921–949.

McWilliams, J., Holland, W., and Chow, J. (1978). A description of numerical antarctic circumpolar currents. *Dynamics of Atmospheres and Oceans*, 2(3):213–291.

Merryfield, W. and Holloway, G. (1999). Eddy fluxes and topography in stratified quasi-geostrophic models. *Journal of Fluid Mechanics*, 380:59–80.

Nadeau, L.-P. (2011). *Dynamics of a quasigeostrophic Antarctic Circumpolar Current.* PhD thesis, McGill University.

Nakamura, M. and Chao, Y. (2000). On the eddy isopycnal thickness diffusivity of the gent-mcwilliams subgrid mixing parameterization. *Journal of climate*, 13(2):502–510.

Nakamura, N. (1996). Two-dimensional mixing, edge formation, and permeability diagnosed in an area coordinate. *Journal of the atmospheric sciences*, 53(11):1524–1537.

Naveira Garabato, A. C., Ferrari, R., and Polzin, K. L. (2011). Eddy stirring in the southern ocean. *Journal of Geophysical Research: Oceans (1978–2012)*, 116(C9).

Nowlin Jr, W. and Klinck, J. (1986). The physics of the antarctic circumpolar current. *Reviews of geophysics*, 24(3):469–491.

Nurser, A. G. and Lee, M.-M. (2004). Isopycnal averaging at constant height. part ii: Relating to the residual streamfunction in eulerian space. *Journal of physical oceanography*, 34(12):2740–2755.

Olbers, D., Willebrand, J., and Eden, C. (2012). *Ocean Dynamics.* Springer.

Pedlosky, J. (1963). Baroclinic instability in two layer systems. *Tellus*, 15(1):20–25.

Phillips, H. and Rintoul, S. (2000). Eddy variability and energetics from direct current measurements in the antarctic circumpolar current south of australia. *Journal of physical oceanography*, 30(12):3050–3076.

Pope, S. (2000). *Turbulent flows.* Cambridge university press.

Rhines, P. (1975). Waves and turbulence on a beta-plane. *J. Fluid Mech*, 69(3):417–443.

Rhines, P. (2001). Mesoscale eddies. In *Encyclopedia of Ocean Sciences, volume 3*, pages 755–767. Elsevier Ltd.

Rivière, P., Treguier, A. M., and Klein, P. (2004). Effects of bottom friction on nonlinear equilibration of an oceanic baroclinic jet. *Journal of physical oceanography*, 34(2):416–432.

Sallée, J., Speer, K., Morrow, R., and Lumpkin, R. (2008). An estimate of lagrangian eddy statistics and diffusion in the mixed layer of the southern ocean. *Journal of Marine Research*, 66(4):441–463.

Salmon, R. (1998). *Lectures on Geophysical Fluid Dynamics.* Oxford University Press.

Sen Gupta, A., Santoso, A., Taschetto, A., Ummenhofer, C., Trevena, J., and England, M. (2009). Projected changes to the southern hemisphere ocean and sea ice in the ipcc ar4 climate models. *Journal of Climate*, 22(11):3047–3078.

Shuckburgh, E., Jones, H., Marshall, J., and Hill, C. (2009). Understanding the regional variability of eddy diffusivity in the pacific sector of the southern ocean. *Journal of Physical Oceanography*, 39(9):2011–2023.

Straub, D. (1993). On the transport and angular momentum balance of channel models of the antarctic circumpolar current. *Journal of physical oceanography*, 23(4):776–782.

Tennekes, H. and Lumley, J. (1972). *A first course in turbulence*. The MIT press.

Thompson, A. (2010). Jet formation and evolution in baroclinic turbulence with simple topography. *Journal of Physical Oceanography*, 40(1):257–278.

Thompson, A. and Sallée, J. (2012). Jets and topography: jet transitions and the impact on transport in the antarctic circumpolar current. *Journal of Physical Oceanography*, 42(6):956–972.

Thompson, A. and Sallée, J.-P. (2010). Jets and topography: Jet transitions and the impacts on transport in the antarctic circumpolar current. Unpublished Manuscript.

Treguier, A., Held, I., and Larichev, V. (1997). Parameterization of quasigeostrophic eddies in primitive equation ocean models. *Journal of Physical Oceanography*, 27(4):567–580.

Vallis, G. (2006). *Atmospheric and Oceanic Fluid Dynamics*. Princeton University.

Vallis, G. (2012). *Climate and the Oceans*. Princeton University Press.

Wang, Z., Kuhlbrodt, T., and Meredith, M. P. (2011). On the response of the antarctic circumpolar current transport to climate change in coupled climate models. *Journal of Geophysical Research C: Oceans*, 116(8). Cited By (since 1996): 4.

Washington, W. and Parkinson, C. (2005). *An introduction to three-dimensional climate modeling*. Univ Science Books.

Witter, D. and Chelton, D. (1998). Eddy-mean flow interaction in zonal oceanic jet flow along zonal ridge topography. *Journal of physical oceanography*, 28(10):2019–2039.

Wolff, J., Maier-Reimer, E., and Olbers, D. (1991). Wind-driven flow over topography in a zonal β-plane channel: A quasi-geostrophic model of the antarctic circumpolar current. *Journal of physical oceanography*, 21(2):236–264.

Appendix A
Matrix Eddy Diffusivity Coefficient Fields

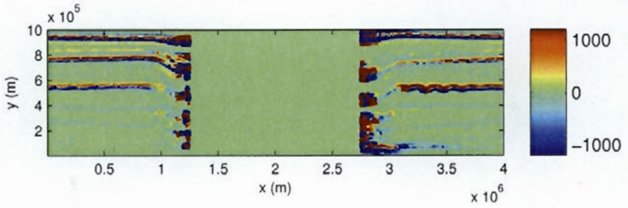

(a) a

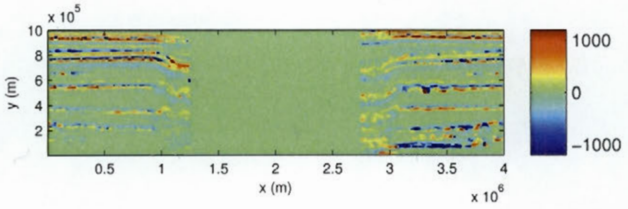

(b) b

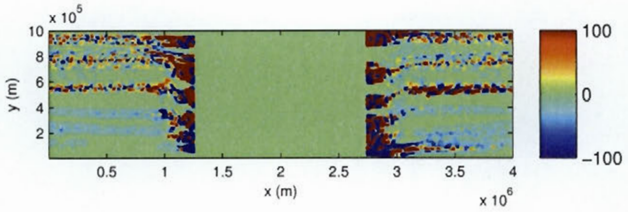

(c) c

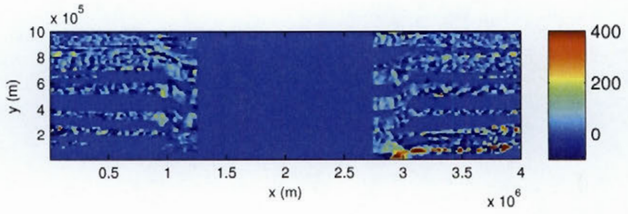

(d) d

Figure A–1: Coefficients for locally defined matrix paramerization in Section 5.5.3. Data from a simulation with a 200 m ridge and F_f of 1.4.